SHIBAURA INSTITUTE OF TECHNOLOGY

DOCTORAL THESIS

Hysteresis Characterization and Compensation of Smart Material-Based Actuators via a New Modified Bouc-Wen Model

---

Author:
Mohd Hanif Bin Mohd RAMLI
Supervisor:
Professor Xinkai CHEN

A thesis submitted in fulfillment of the requirements
for the degree of Doctor of Philosophy

February 20, 2017

SHIBAURA INSTITUTE OF TECHNOLOGY

Abstract

Doctor of Philosophy

Hysteresis Characterization and Compensation of Smart Material-Based Actuators via a New Modified Bouc-Wen Model

by Mohd Hanif Bin Mohd RAMLI

Most smart material based actuators (smart actuators) are known for their prominent characteristics of a high resolution of positioning, high bandwidth, and the ease of integration in miniaturized systems. However, their applications are restricted by the inherent hysteresis nonlinearity. This thesis presents an alternative modification to the original Bouc-Wen (BW) model in order to improve the characterization of smart actuators those are affected by hysteresis effects. The modified BW model is formulated in the discrete-time domain. The extended particle swarm optimization technique (EPSO) is used to properly validate the proposed model. Through the simulation study, it is observed that proposed model is capable of describing rate-dependent input-output relations which is an important feature in the modeling of hysteresis phenomenon. Then, the proposed model is directly used in developing control strategies to mitigate the hysteresis effects. In this case, two control architectures are developed; a discrete nonlinear prescribed performance control (DPPC) scheme and a discrete model reference adaptive control strategy (DMRAC). In addition, theoretical analysis of the closed-loop system's stability under each control algorithm is also systematically discussed. Finally, the efficacy of formulated control strategies are verified via real case applications. The simulation and experimental results substantiate the capacity of the proposed MBW model. It is not only applicable for modeling and characterization, but also towards control development for the betterment of motion tracking problems in smart actuators that are affected by hysteresis effects.

Acknowledgements

"*In the name of God, most Gracious, most Compassionate*".

During the past three years, I had learned technical skills and worked around nice colleagues. The most important is that this experience offers me the opportunity to grow as a person, both professionally and personally. There are many people I want to thank for their support during the time I spent on my research, without their help and support I would never have made it.

First of all, I would like to thank my supervisor Professor Xinkai Chen. I feel grateful that he gives me the opportunity to pursue a Ph.D. degree. I want to thank him for the guidance, support, patience and criticism that he gave me during my research. I also thank him for creating such a nice research environment, where he was always there for discussions whenever I needed. It would not have been possible to conduct the research that presented here without his help, suggestions and ideas.

My special gratitude goes out to my wife, Norlizan, for her love, source of my inspiration to complete this work. Furthermore, I would like to thank my parents for all the sacrifices they have had to make as I achieve my dreams. A very special thank you to my colleagues, Linh Manh Nguyen, and Chen's Laboratory members for all the support they have given me over the years.

Last but not least, I would like to convey my gratitude to Ministry of Education (KPM) and Universiti Teknologi MARA (UiTM) for their financial supports.

Thank you very much.

Contents

List of Figures

List of Tables

List of Abbreviations

BW	**B**ouc-**W**en
DEB	**D**ifferential **E**quations **B**ased
DMRAC	**D**iscrete **M**odel **R**eference **A**daptive **C**ontrol
DPPC	**D**iscrete **P**rescribed **P**erformance **C**ontrol
FC	**F**unnel **C**ontrol
GMA	**G**iant-**M**agnetostrictive **A**ctuator
LMI	**L**inear **M**atrix **I**nequalities
MAE	**M**aximum **A**bsolute **E**rror
MBW	**M**odified **B**ouc-**W**en
PEA	**P**iezoeletric **A**ctuator
P-I	**P**randtl-**I**shlinskii
PI	**P**roportional-**I**ntegral
PID	**P**roportional-**I**ntegral-**D**erivative
PSO	**P**article **S**warm **O**ptimization
RC	**R**epetitive **C**ontrol
RMSE	**R**oot **M**ean **S**quare **E**rror

List of Symbols

AC	the space of absolute continuous function
C	the space of continuous function
C^1	the space of continuous differentiable functions
$\mathbb{R}$	the field of real number
$\mathbb{R}_+$	the field of positive real number
$\in$	set membership (is an element of)
$sign(\nu, \mu)$	signum function of $sign(\nu).sign(\mu)$

Chapter 1

Introduction

1.1 Overview

In recent decades, there has been a substantial advancement in various smart materials and devices driven by these materials (Esbrook et al., 2014), (Olabi and Grunwald, A., 2008). The potential advantages of these smart material-based actuators (such as piezoelectric, magnetostrictive, electroactive polymers, and shape memory alloys) include a high resolution of positioning and the ease of integration in miniaturized systems. Some of them can provide a very high bandwidth, whilst others very high stiffness, or high range of deformation and thus of positioning (Grossard and Rakotondrabe, M., 2016). Their potential applications extend over a range of different industries including semiconductor fabrication systems manufacturing (Wang et al., 2015b), robotics (Karpelson et al., 2012), automotive (Melbert et al., 2006), medical applications (Levi et al., 2008), (Kaplanoglu, 2012) (for industrial fields), also can be found in digital equipment such as in optical axis alignment of optical fiber, and positional control of CCD (charge coupled device) for enhancement of image resolution (Ko et al., 2008). Certainly, optimal designs of mechatronic actuators together with appropriate control strategies may lead to the realization of high-precision and reliable actuation mechanisms. However, most smart material-based actuation systems, in general, suffer from hysteretic nonlinearity phenomenon which greatly deteriorates and limits the systems' performance.

The term 'hysteresis' originally comes from an ancient Greek word which means 'to lag behind'. This phenomenon is first observed by scientists in the fields of ferromagnetism about 200 years ago (Iyer and Tan, X., 2009). According to Oh et al., 2009, hysteresis is a quasi-static phenomenon in which a sequence of periodic inputs produces a

nontrivial input-output loop as the period of the input increases without bound. It is a fundamental problem in magnetic fields, smart materials (commonly in ferromagnetic and ferroelectric materials), and mechanical systems where it may lead to performance degradation if not properly handled. As for now, there is no fundamental theory that allows a general mathematical framework for modeling the hysteresis effects because the origins of these phenomena are often multiple and unclear (Ikhouane and Rodellar, J., 2007). In the literature, the common method of characterizing the hysteresis behaviour is either based on the law of physics or the phenomenological approach (Xu and Kiong, K., 2016). A notable example of the physics-based model is Jiles-Atherton model, where it is the first model to describe ferromagnetic hysteresis. Meanwhile, the phenomenological-based models that have been employed include: i). Preisach, Prandtl–Ishlinskii (PI) operators, and their extensions which are normally based on the weighted superposition of many (and even infinitely many) fundamental hysteretic units known as hysteron, ii). differential equations based (DEB) operators, such as Dahl model, Coleman-Hodgdon model, and Bouc-Wen (BW) model.

Through the literature review, various control strategies have been developed to cope with the hysteresis effects. In general, the control strategy can be roughly classified into the open-loop or feedforward control, and the feedback control schemes (Hassani et al., 2014). In the feedforward control method, the basic idea is to employ the inversion of a hysteresis operator for compensating the hysteretic behaviour. This technique is pioneered by Krejci and Kuhnen, K., 2001 where an inverse compensator based on the classical P–I model is proposed. Meanwhile, for hysteretic systems those are described by DEB models such as the Duhem model, Dahl model, and BW model, the inverse construction is either impossible or extremely difficult to be obtained (Gu et al., 2016). In this case, the feedforward compensator can be achieved by an alternative solution, known as multiplicative-inverse approach such as reported by Rakotondrabe, 2011 where the compensator is developed based on BW model. In the same vein, Habineza et al., 2015 extend it to multiple degree of freedom (DOF) hysteretic systems. However, the main challenge with such approaches is the modeling complexity and parameter sensitivity. Therefore, the performance of this control scheme is sensitive to errors in the plant transfer function, leading to problems such as divergence and instability. Conversely, hysteresis compensation is dealt by several approaches in the

feedback control scheme. The first approach is to directly develop a feedback controller without the use of hysteresis operators. The simplest solution is to consider the famous Proportional-Integral-Derivative (PID) control. In the second method, the system that is affected by the hysteresis is modeled by a composition of two terms namely, a linear term and a bounded disturbance-like term. In this approach, the non-smooth hysteresis nonlinearity can be dealt with a number of feedback control techniques as reported by Shan and Leang, K. K., 2012; Xu, 2015; Zhong and Yao, B., 2008. Alternatively, control design and stability analysis methods are proposed based on the properties of hysteresis itself such as monotonicity, sector-bound or dissipativity to ensure that the controller is robust against the parameter uncertainties and thus stable. For example, Gorbet et al., 2001 derive the dissipativity of the Preisach operator and design a controller, which is strictly passive for the smart actuators. Another result that is similar to this method can be found in Jayawardhana et al., 2012.

In this thesis, we devote the focus onto a class of DEB models with regard to its feasibility of modeling and control of smart actuators. This consideration is motivated by observing the fact that differential equations, in general, are well-suitable for controller design purposes. It is remarked that this class of operator can soundly describe a range of shapes of hysteretic effects which match the behaviour of a wide class of hysteretic systems. In addition, it could provide physical insights to the problem, i.e., the changes to its parameters reflect the shape, amplitude, and orientation of the hysteresis curves. Recent results on the differential equations based operators in the control and systems literature include Du et al., 2009; Habineza et al., 2015; Jayawardhana et al., 2012; Xu and Li, Y., 2010.

1.2 Aim and Objectives

Generally, this research is aimed at improving the characterization and control of nonlinear systems in the discrete-time domain. In particular, this research deals with hysteresis, which is the fundamental problem in smart actuators. To fulfil this requirement, the following objectives are set.

1. To improve the characterization accuracy for describing the nonlinear hysteretic behaviour in the smart actuators.

In order to solve the motion tracking problem in smart actuators, a good hysteresis model or operator is required. Indeed, there are many suitable candidates for this purpose, but in this thesis, the focus is devoted to the class of DEB models. First, the feasibility of the DEB models towards hysteresis characterization and control fusion will be carefully examined. Then, a new model modification will be developed based on the outcome of above investigation with a goal to improve the characterization and control of hysteretic behaviour in the smart actuators. This development will be established in the discrete-time domain.

2. To fuse the DEB model into the control design.

   In this case, two control structures are proposed in order to mitigate hysteresis effects. Both of these structures consider DEB model in the development. The first control framework is based on the prescribed performance control. The second one is an adaptive control strategy. In addition, stability analysis pertaining to each control scheme will be systematically presented.

1.3 Outline of Thesis

The title of this research is "Hysteresis Characterization and Compensation of Smart Material-Based Actuators via a New Modified Bouc-Wen Model". This section briefly describes the contents of this research thesis, which consists of 6 chapters, including Introduction, Literature Review, Modeling of Smart Actuators, Discrete Nolinear Prescribed Performance Control, Discrete Model Reference Adaptive Control, and lastly Conclusions and Recommendations.

Chapter 1: The first chapter provides a general introduction and background of the whole research, including overview, research objectives, as well as an outline of the thesis.

Chapter 2: The second chapter elucidates the literature review, which describes previous studies related to this research. The chapter begins with an introduction of hysteresis phenomenon in smart actuators. Then, it is followed by hysteresis modeling. System identification is also discussed. Finally, a discussion about control issues on the

smart actuators is presented.

Chapter 3: In the first stage, the feasibility of the DEB models towards hysteresis characterization and control fusion are carefully examined. Then, a new model modification is proposed based on the outcomes of above investigation. Additionally, a method of model validation is presented. In this case, experimental data from three types of smart-material based actuators are considered namely, a piezoelectric actuator (PEA), a giant-magnetostrictive actuator (GMA), and an ionic polymer metal composites actuator (IPMC) to study the capacity of the proposed model in fitting and matching real input-output relations.

Chapter 4: The fourth chapter demonstrates the practicality of the proposed model for compensating hysteresis nonlinearity of a linear piezoelectrically actuated positioning system (PEA stage). The control architecture is synthesized by fusing the proposed model into a discrete-time version of the prescribed performance control strategy. In the controller establishment, a new performance function is introduced to properly define the ultimate allowable steady-state error bound and transient behaviour. In addition, stability analysis of the closed-loop system is also systematically discussed. Finally, the proposed control scheme is implemented and tested on PEA stage to show its effectiveness.

Chapter 5: In this chapter, we exploit the proposed model in designing a robust adaptive control law in order to mitigate the hysteresis nonlinearity. Theoretical analysis of the closed-loop system with regard to stability is also systematically presented. Finally, a real case control implementation is given to verify the effectiveness of the formulated control strategy. In this case, the GMA is used as the test rig.

Chapter 6: The last chapter of this thesis explains conclusions of research findings, discoveries and provides future recommendations for forthcoming improvement.

Chapter 2

Literature Review

2.1 Introduction

The study of hysteresis phenomenon has a long history. It is first observed in the field of ferromagnetism by James A. Ewing in 1881 (Iyer and Tan, X., 2009). This phenomenon is history dependent, i.e., it can be referred to a system that has memory, where the effects of input to the system are experienced with a certain delay in time. According to Oh and Bernstein, D. S., 2005, hysteresis is a quasi-static phenomenon in which a sequence of periodic inputs produces a non-trivial input-output loop as the period of input increases without bound. This phenomenon arises in diverse fields ranging from physics to biology, from material science to mechanics, and from electronics to economics.

In recent decades, there has been a substantial advancement in various smart materials which lead to a new class of sensing and actuation systems. A broad range of materials falls into this class, including piezoelectrics, magnetostrictives, shape memory alloys (SMA), electro-active polymers, and magnetorheological fluids. Their advantages include high flexibility in shape designs, versatility, and power–to–weight ratio compared to the traditional rigid actuators. Their potential applications extend over a range of different industries including manufacturing (Wang et al., 2015b); for example in semiconductor fabrication systems, robotics (Karpelson et al., 2012), automotive (Melbert et al., 2006), medical applications (Levi et al., 2008) (for example see Fig. 2.1a), (Kaplanoglu, 2012) (for industrial fields), also can be found in digital equipment such as in optical axis alignment of optical fiber, and positional control of CCD (charge coupled device) for enhancement of image resolution (Ko et al., 2008) as illustrated in Fig. 2.1b (an auto focus camera module that has a size of 10x9.8x5.6t (in mm)). These materials,

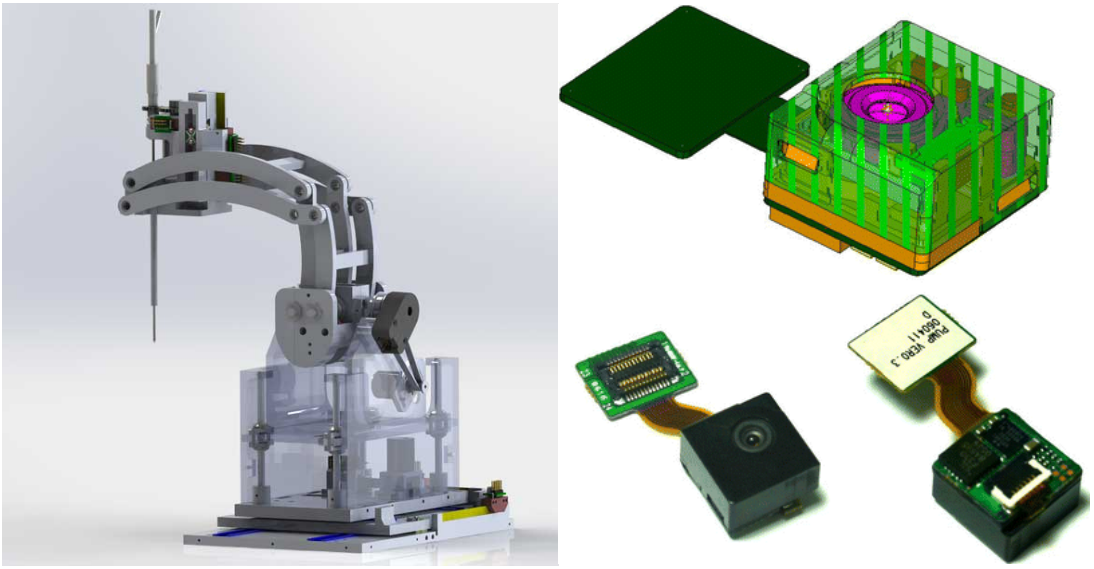

(A) A diagram of Magnetic Resonance Imaging (MRI) driven by PEA (MICROMO company).

(B) Perspective views of an auto-focus module adapted from (Ko et al., 2008)

FIGURE 2.1: Examples of real applications driven by smart actuators.

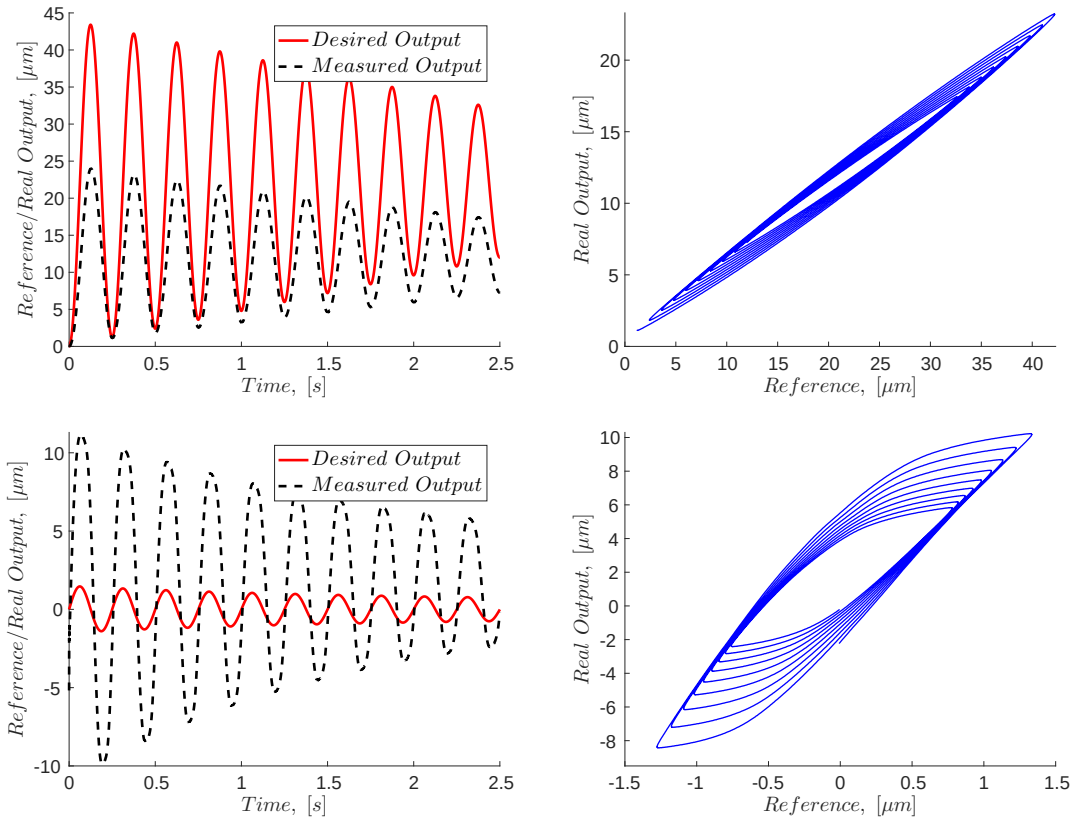

FIGURE 2.2: The plots of open-loop input-output relations measured in the experiments. (Top) A PEA case. (Bottom) A GMA case.

however, are strongly exhibit hysteresis. As a result, systems that driven by these materials are directly affected by the hysteresis effects and give rise to poor performance (Gu et al., 2016; Zhang et al., 2015). Fig. 2.2 illustrates the hysteresis effects in the smart actuators, in particular, PEA and GMA for the case of a damped input trajectory.

This chapter provides a brief literature survey relating to the various types of hysteresis models with regard to their applications in modeling and control. In the remaining part of this study, different types of methods which are utilized for parameter estimation, system identification and a discussion about control issues on the smart actuators will also be provided.

2.2 Conventional models of hysteresis

As for now, there is no fundamental theory that allows a general mathematical framework for modeling the hysteresis effects because the origins of these phenomena are often multiple and unclear (Ikhouane and Rodellar, J., 2007). In the literature, it can be noticed that most of the existing models of hysteresis are initially developed to describe a particular type of hysteretic system but their mathematical forms are to a degree suitable for multi-disciplinary extensions. For example, Preisach model is initially developed to describe the dependence of magnetization on magnetic field in ferromagnetic systems in the mid-1930s. The model is widely used by the scientific community only after 50 years later following the works by Mayergoyz, 1986. Since then, the model has been extended to describe hysteresis phenomena in many other areas of science such as electromagnetism, economics, biology, geology, and has become one of the most utilized mathematical models in the literature.

By and large, the common approach of characterizing the hysteresis behaviour is either by the law of physics or the phenomenological method (Xu and Kiong, K., 2016). A notable example of the physics-based model is Jiles-Atherton model, where it is the first model to describe the ferromagnetic hysteresis. Meanwhile, the phenomenological-based models that have been exploited include:

1. Operator based models such as Preisach, Prandtl–Ishlinskii (P-I) operators, and their extensions which are normally based on the weighted superposition of many (and even infinitely many) fundamental hysteretic units known as hysteron,

2. Differential equation based (DEB) operators, such as Coleman-Hodgdon model, Dahl model, and Bouc-Wen model.

2.2.1 Physics based models

In general, physics-based models are established based on the principle of physics, such as the relationships of energy, displacement and so on. However, it is difficult to build a model by this principle because physical feature of a hysteretic system is usually very complicated. Moreover, a physics-based model developed for one smart actuator may not be used for another kind of actuator and thus no model generalization is possible.

A well known physics-based model is the Jiles-Atherton model which is introduced in the early 1980s to describe hysteresis curves in magnetic materials. The relation between magnetization y field strength within the material and the applied magnetic u is described by

$$\frac{dy}{du} = \frac{(1-\tau)L(u+Ay) - y}{\varrho(1-\tau)sgn(\dot{u}) - A(L(u+Ay) - y)} + \tau\frac{L(u+Ay)}{du} \tag{2.1}$$

where τ, A, and ϱ are the model parameters, which are assumed to be non-negative, and L is the anhysteretic curve in which can be described by Langevin function

$$L(u) = y_{sat}(coth(\frac{u}{B_A}) - \frac{B_A}{u}) \tag{2.2}$$

in which B_A is another fitting parameter and y_{sat} is the saturation value of the output. (*anhysteretic : not involving or producing hysteresis.)

The following constraints are imposed to ensure that the model is always bounded-input bounded-output (BIBO) stable:

1. $k(1-\tau)sgn(\dot{u}) > A(L(u+Ay) - y)$ for all possible values of u and y.
2. $1 - A\tau\frac{dL(u)}{du} > 0$ for any u. If the anhysteretic function is given by (2.2), then this condition is equivalent to $3 > A\tau y_{sat}$

It can be shown that the Jiles-Atherton model has the following properties (Dimian and Andrei, P., 2014)

1. The output variable is bounded and lies in the interval $(-y_{sat}, y_{sat})$.

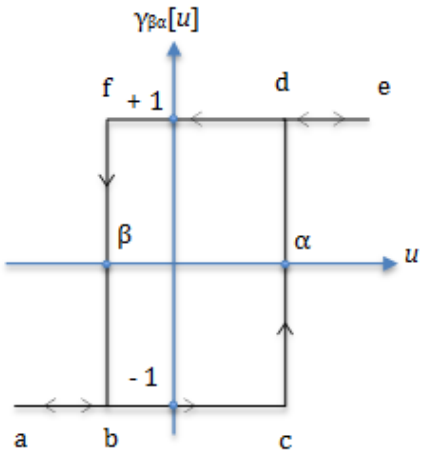

FIGURE 2.3: A Preisach hysteron $\gamma_{\beta\alpha}[u]$.

2. The hysteretic state of the Jiles-Atherton model is completely described by the value of the input, output, and the direction (increasing or decreasing) of the input variable.

3. Eqn. (2.1) can be written in the form of a nonlinear first-order differential equation by taking the derivative in the last term in (2.1) and using the chain rule. One obtains

$$\frac{dy}{du} = \frac{(1-\tau)L(u+Ay)-y}{\varrho(1-\tau)sgn(\dot{u})-A(L(u+Ay)-y)} + \tau\frac{dL(u_{eff})}{d(u_{eff})}(1+A\frac{dy}{du}) \tag{2.3}$$

after a few rearrangements

$$\frac{dy}{du} = \frac{\frac{(1-\tau)L(u+Ay)-y}{\varrho(1-\tau)sgn(\dot{u})-A(L(u+Ay)-y)} + \tau\frac{dL(u_{eff})}{d(u_{eff})}}{1-A\tau\frac{dL(u_{eff})}{d(u_{eff})}} \tag{2.4}$$

2.2.2 Phenomenological based models

2.2.2.1 Preisach model

The Preisach model is constructed based on the weighted superposition of many (and even infinitely many) fundamental hysteretic units known as hysteron. For $u(t) \in C[0,T]$ (the space of continuous functions on $[0,T]$) and initial configuration $\chi \in -1, 1$, $y(t) = \gamma_{\beta\alpha}[u,\chi]$ in Fig. 2.3 is defined as

$$y(t) = \begin{cases} -1, & \text{if } u(t) < \beta \\ 1, & \text{if } u(t) > \alpha \\ y(t^-), & \text{if } \beta \leq u(t) \leq \alpha \end{cases} \tag{2.5}$$

$t^- \equiv lim_{\varsigma>0}(t-\varsigma)$ and $y(0^-) = \chi$.

The Preisach plane is defined as

$$P_0 \equiv \{(\beta, \alpha) \in \mathbb{R}^2 | \beta \leq \alpha\} \tag{2.6}$$

where $(\beta, \alpha) \in P_0$ is identified with the hysteron $\gamma_{\beta,\alpha}u(t)$. For $u(t) \in C[0,T]$, then, the output $y(t)$ is calculated as

$$y(t) = \Gamma[u(t)] = \iint_{P_0} \varepsilon(\beta, \alpha)\gamma_{\beta,\alpha}[u(t)]\, d\beta\, d\alpha \tag{2.7}$$

where Γ is known as Preisach operator, and $\varepsilon(\beta, \alpha)$ is a weighting function called the Preisach density function. A hysteron constitutes a nonideal delayed relay parameterized by two threshold values (β, α), at which the hysteron flips among two binary states $\{-1, +1\}$. Assume that $\varepsilon(\beta, \alpha) = 0$ if $\beta<\beta_0$ or $\alpha>\alpha_0$ for some β_0 and α_0, then it is sufficient to consider a finite triangular area in the Preisach plane P in which defined as

$$P \equiv \{(\beta, \alpha) \in P_0 | \beta \leq \beta_0, \alpha \leq \alpha_0\} \tag{2.8}$$

At time t, P can be divided into two regions

$$P_+(t) \equiv \{(\beta, \alpha) \in P | \; output \; of \; \gamma_{\beta,\alpha}[u(t)] \; at \; t \; is \; +1\} \tag{2.9a}$$

$$P_-(t) \equiv \{(\beta, \alpha) \in P | \; output \; of \; \gamma_{\beta,\alpha}[u(t)] \; at \; t \; is \; -1\} \tag{2.9b}$$

Let the input $u(t)$ change as follows: at time t_0, the input $u(t_0)=u_0<\beta_0$, and then the output of each hysteron is -1, as shown in Fig. 2.4(b). Next, $u(t)$ is increases monotonically to some maximum value at time t_1 with $u(t_1)=u_1$, and the output of each hysteron whose α is less than u_1 is switched to +1, as shown in Fig. 2.4(c). Based on Eqn. (2.7), the output $y(t)$ for the case that shown in Fig. 2.4(c) can be written as

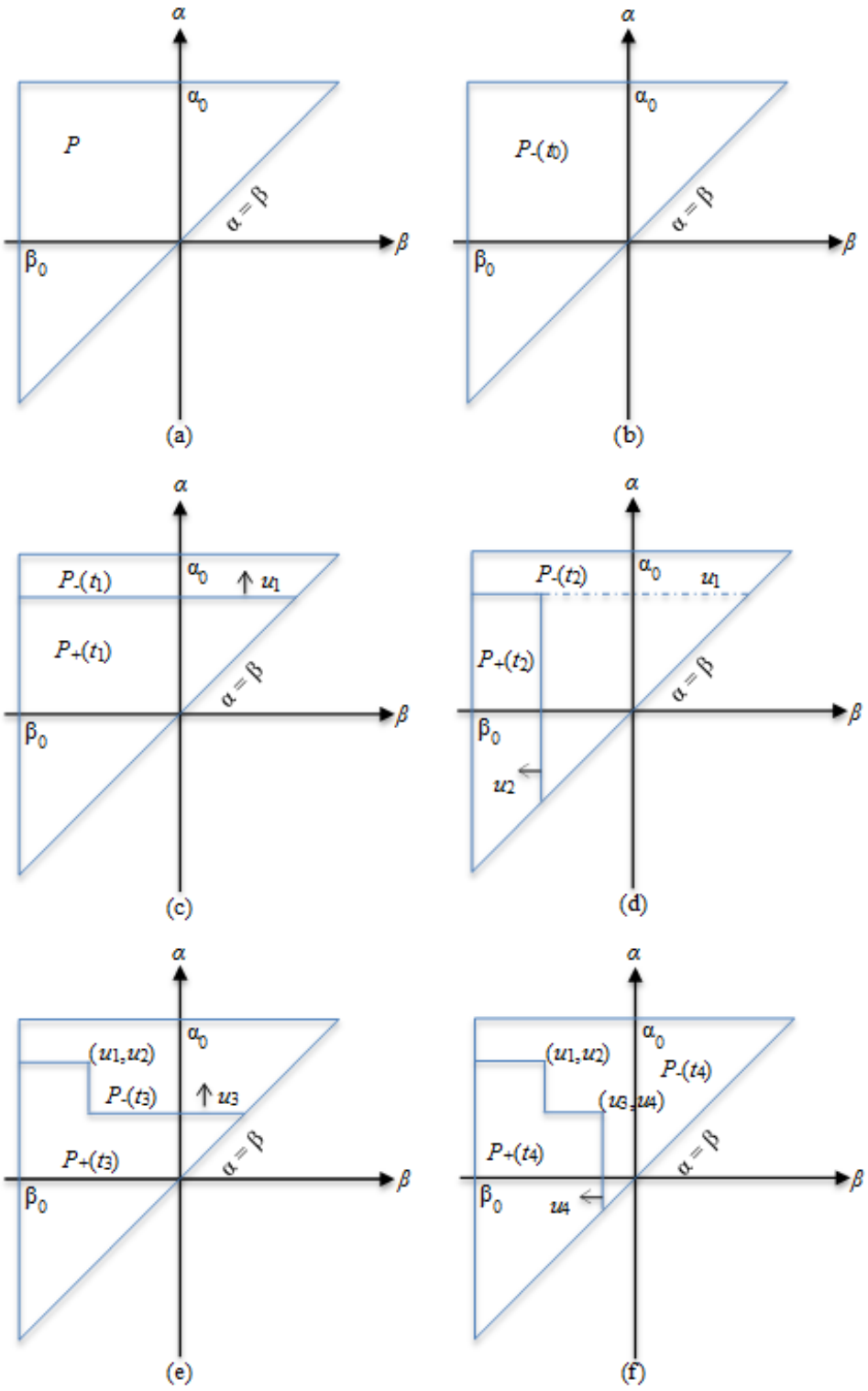

FIGURE 2.4: The occurrence of memory curves on the Preisach plane. (a) No input. (b) $u{=}u_0{<}\beta_0$. (c) $\beta_0{<}u{=}u_1{<}\beta_0$. (d) $\beta_0{<}u{=}u_2{<}u_1$. (e) $u_2{<}u{=}u_3{<}u_1$. (f) $u_2{<}u{=}u_4{<}u_3$.

$$y(t) = \iint_{P_+(t_1)} \varepsilon(\beta,\alpha)\gamma_{\beta,\alpha}[u(t)]\,d\beta\,d\alpha - \iint_{P_-(t_1)} \varepsilon(\beta\alpha)\gamma_{\beta,\alpha}[u(t)]\,d\beta\,d\alpha \tag{2.10}$$

As the input $u(t)$ starts to decrease monotonically until it stops at time t_2 with $u(t_2)$=u_2, and the output of each hysteron whose β is greater than u_2 is switched to -1, as shown in Fig. 2.4(d). Next, $u(t)$ increases monotonically to u_3 at time t_3 and u_3<u_1, as shown in Fig. 2.4(e). Finally, $u(t)$ decreases monotonically to u_4 at time t_4 and u_4>u_2, as shown in Fig. 2.4(f). The above input reversals generate staircase structured boundary between $P_+(t)$ and $P_-(t)$, and coordinate of the boundary's intersection with the line α=β correspond to the current value of the input. In general, the output $y(t)$ equals to the integral of Preisach density function in the $P_+(t)$ boundary. This boundary captures the memory effect of the Preisach operator, so called memory curve.

The presence of a double integral makes the Preisach model relatively complicated to solve. Numerical and approximative approaches are introduced to simplify such complexity as reported by Reimers and Della Torre, E., 1998; Song and Li, C.J., 1999; Tan and Baras, J. S., 2004. Although the Preisach model is well suited for hysteresis loops of arbitrary shape, a much higher effort is needed to make it work smoothly within the modeling and control framework (Rosenbaum et al., 2010).

2.2.2.2 Prandtl-Ishlinskii model

The classical Prandtl-Ishlinskii (P-I) model is based on the backlash (also known as play) operator (see Fig. 2.5). For an input function u, which is monotonic (nondecreasing or nonincreasing) in each interval $[t_{i-1}, t_i]$ of a partition $0 = t_0 < ... < t_m = T$ and for a given threshold r>0, the output of a backlash operator is defined by

$$F_r[u](t) = max(u(t) - r, min(u(t) + r, F_r[u](t_{i-1}))) \tag{2.11}$$

with initial condition $F_r[u](0)$=$max(u(0) - r, min(u(0) + r, 0))$. For a given input $u(t) \in C[0, T]$, the output of the P–I model can be expressed as

$$y(t) = P[u](t) = p_0 u(t) + \int_0^\infty p(r)F_r[u](t)dr \tag{2.12}$$

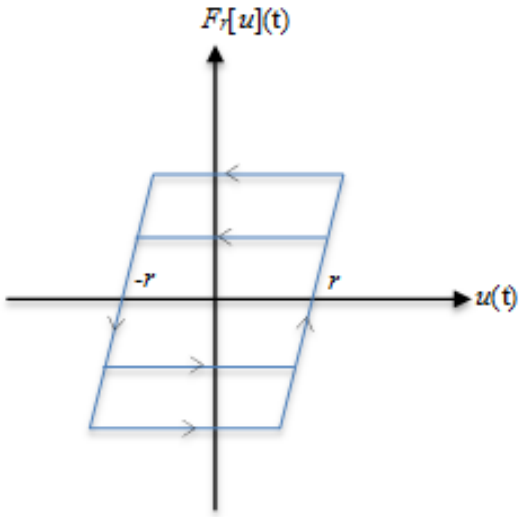

FIGURE 2.5: A backlash operator with a unity slope.

in which p_0 is a positive constant and $p(r)$ is an integrable density function that vanished for large value of r. It is reasonable to assume that there exists a constant R such that $p(r) = 0$ for $r > R$. The density function $p(r)$ is usually defined based on the experimental data (Janaideh et al., 2016; Jiang et al., 2010).

To implement the model (2.12), it is necessary to approximate the integrals. This problem can be solved by introducing a discrete P-I operator of the play type which given as (Janocha and Kuhnen, K., 2000).

$$y(t) = P[u](t) = p_0 u(t) + \sum_{j=1}^{M} p_j \cdot F_r[u](t) \tag{2.13}$$

where p_j denote the weights that are calculated from experimental data, and M is the number of adopted play operators.

In view of relation (2.13), it is obvious that parameters of the P–I model can be easily identified, for example, via a simple Least Square identification method. Furthermore, P-I model is analytically invertible and thus can be used as feedforward compensator. This makes the P–I model convenient for different applications that related to real-time micro-positioning and nano-positioning systems (Janaideh et al., 2016).

2.2.2.3 Duhem model

Duhem model is originally developed to describe magnetic hysteresis and has a property in which every state is equilibrium under constant inputs and the output can only change its character when the input changes its direction (Padthe et al., 2008). For a given shape functions x_1 and x_2, the relationship between input $u(t)$ and output $y(t)$ is expressed as

$$\dot{y}(t) = x_1(y(t), u(t))\dot{u}_+(t) - x_2(y(t), u(t))\dot{u}_-(t) \tag{2.14}$$

where $\dot{u}_+(t)$ and $\dot{u}_-(t)$ are defined as

$$\dot{u}_+(t) = max\{0, \dot{u}(t)\}, \quad \dot{u}_-(t) = min\{0, \dot{u}(t)\} \tag{2.15}$$

The Duhem model as defined in (2.14) has the following properties (Jayawardhana et al., 2012):

- **Existence of solution**

  If for every $u \in \mathbb{R}$, the functions x_1 and x_2 are C^1 and satisfy

  $$(y_1 - y_2)[x_1(y_1(t), u(t)) - x_1(y_2(t), u(t))] \leq \lambda_1(u)(y_1 - y_2)^2, \tag{2.16a}$$

  $$(y_1 - y_2)[x_2(y_1(t), u(t)) - x_2(y_2(t), u(t))] \geq \lambda_2(u)(y_1 - y_2)^2. \tag{2.16b}$$

  for all $y_1, y_2 \in \mathbb{R}$, where λ_1 and λ_2 are nonnegative, then (2.14) has a unique global solution.

- **Monotonicity**

  If $x_1, x_2 \geq 0$, then the Duhem model (2.14) is piecewise monotone, i.e., for every $u \in AC(\mathbb{R}_+)$, the inequality $\dot{y}(t)\dot{u}(t) \geq 0$ holds at every $t \in \mathbb{R}_+$

- **Rate-independent**

  The rate-independency property of the Duhem model (2.14) can be interpreted as follows, let $\tau : [0, \infty) \to [0, \infty)$ be a continuous nondecreasing function satisfying $\tau(0) = 0$ and $\lim_{t\to\infty} \tau(t) = \infty$, i.e., τ is the time transformation, then $(u(t) \circ \tau, y_0) = (u(t), y_0) \circ \tau$. In other terms, for any periodic input $u(t)$, the input-output relation does not depend on the input frequency.

- **Causality**

  The output depends on the past and current inputs but not future inputs, i.e., the $y(t_0)$ only depends on the input $u(t)$ for values of $t \leq t_0$

However in applications, Eqn. (2.14) is simplified to the special case and given as (Coleman and Hodgdon, M. L., 1987)

$$\dot{y}(t) = a|\dot{u}(t)|(x_1(u) - y(t)) + x_2(u)\dot{u}(t) \tag{2.17}$$

with a constant $a > 0$. Eqn. (2.17) is formally known as Coleman-Hodgdon model and satisfies the following three conditions.

Condition 1: $x_1(u)$ is odd, piecewise smooth, monotonically increasing, real–valued function, with a finite first-order derivative $x_1'(u)$ at infinity;

Condition 2: $x_2(u)$ is an even piecewise continuous, real–valued function with a limit that satisfies

$\lim_{u\to\infty} x_2(u) = \lim_{u\to\infty} x_1'(u)$

Condition 3: $x_1'(u) \geq x_2(u)$ and $ae^{au}\int_0^\infty |x_1'(\tau) - x_2(\tau)|e^{-au}d\tau \leq x_2(u)$ for all $u > 0$.

Thus, for monotone piecewise $u(t)$, Eqn. (2.17) can be solved explicitly as

$$y(t) = x_1(u) + \Psi(u) \tag{2.18}$$

where $\Psi(u)$ is defined as

$$\Psi(u) = (y_0 - x_1(u_0))e^{-a(u-u_0)sgn(\dot{u})} - e^{-ausgn(\dot{u})}\int_{u_0}^{u}(x_1'(\zeta) - x_2(\zeta))e^{a\zeta sgn(\dot{\zeta})}d\zeta \tag{2.19}$$

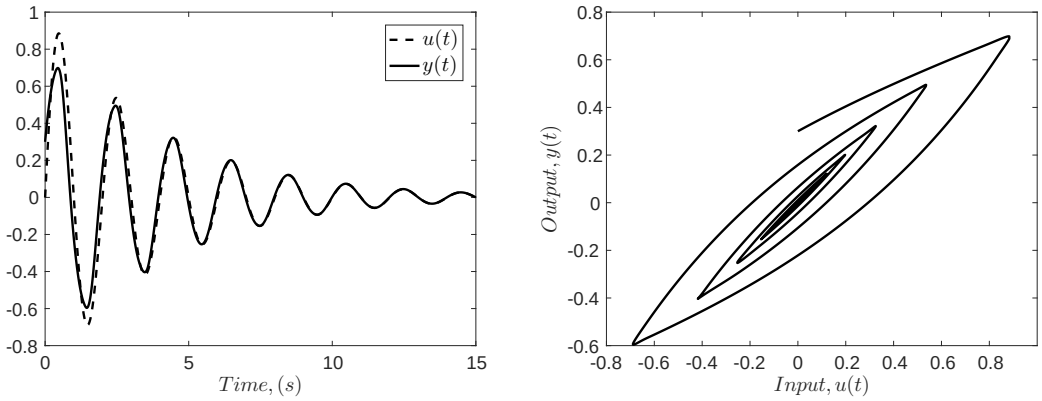

FIGURE 2.6: The input-output map of the Backlash model (2.21) with $a = 1.5$, $b = 1$ and $c = 0.5$.

for constant $\dot{u}(t)$ and $y(u_0) = y_0$. It has been shown by Du et al., 2009 that $\Psi(u) \to 0$ as $u \to \infty$ if $y(u; u_0, y_0)$ is the solution of (2.18) with initial values (u_0, y_0), i.e.,

$$\lim_{u \to +\infty} \Psi(u) = \lim_{u \to +\infty} (y(u : u_0, y_0) - x_1(u)) = 0, \ \dot{u} > 0. \tag{2.20a}$$

$$\lim_{u \to -\infty} \Psi(u) = \lim_{u \to -\infty} (y(u : u_0, y_0) - x_1(u)) = 0, \ \dot{u} < 0. \tag{2.20b}$$

For example, if the shape functions $x_1(u)$ and $x_2(u)$ are chosen as $x_1(u) = (c/a)u$ and $x_2(u) = b$. Eqn. (2.17) can be further expressed as

$$\dot{y}(t) = b\dot{u}(t) - a|\dot{u}(t)|y + c|\dot{u}(t)|u(t) \tag{2.21}$$

Relation in (2.21) is known as Backlash-like (Backlash) model (Su et al., 2000). Fig. 2.6 shows the behaviour of the Backlash model with $a = 1.5$, $b = 1$ and $c = 0.5$. Clearly, the main advantage of Duhem model is that different hysteresis shapes can be captured by appropriately choosing the shape functions x_1 and x_2, which satisfy the above three conditions. Furthermore, the solution of Duhem model can be expressed explicitly, which makes it possible to explore the control method for mitigating the hysteresis effects. There are also other shape functions that have been proposed in the literature such as by Zhou and Wang, J., 2013 and Feng et al., 2009. For example, Zhou and

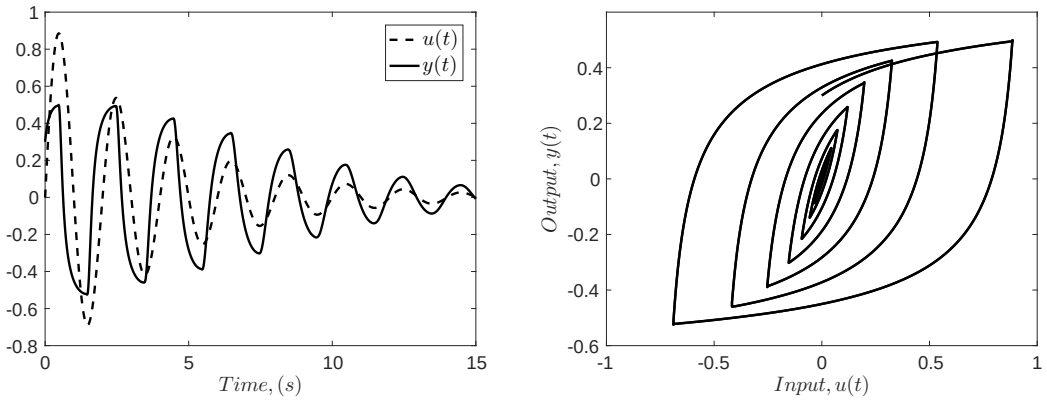

FIGURE 2.7: The input-output map of the Dahl model (2.22) with $\beta = 2.5$, $\sigma = 0.75$ and $r = 3$.

Wang, J., 2013 consider a polynomial based shape functions in modeling piezoelectric-based actuators. Through their experimental verifications, it is shown that the proposed shape functions help the Duhem model to fit and match the experimental data with a reasonable accuracy.

2.2.2.4 Dahl Model

Dahl model (Bliman, 1992; Vedagarbha et al., 1999) is commonly used in mechanical systems, which represents friction force with respect to relative displacement between two surfaces in contact. The general representation of Dahl model is given as

$$\dot{y}(t) = \beta|1 - \frac{y(t)}{\sigma} sgn(\dot{u}(t))|^r sgn(1 - \frac{w}{\sigma} sgn(\dot{u}(t)))\dot{u}(t) \tag{2.22}$$

where $\beta > 0$ and $\sigma > 0$ reflect the slope and shape of the input-output curve respectively, while $r \geq 1$ defines the slope order. Initially this model is formulated to describe the non-linear friction effects in ball bearings. In this case, the output $y(t)$ denotes the friction force, and the input $u(t)$ denotes the relative displacement, σ and β can be regarded as the Coulomb friction force and the rest stiffness respectively. The Dahl model (2.22) is also in the class of rate-independent hysteresis model. Eqn. (2.22) can also be

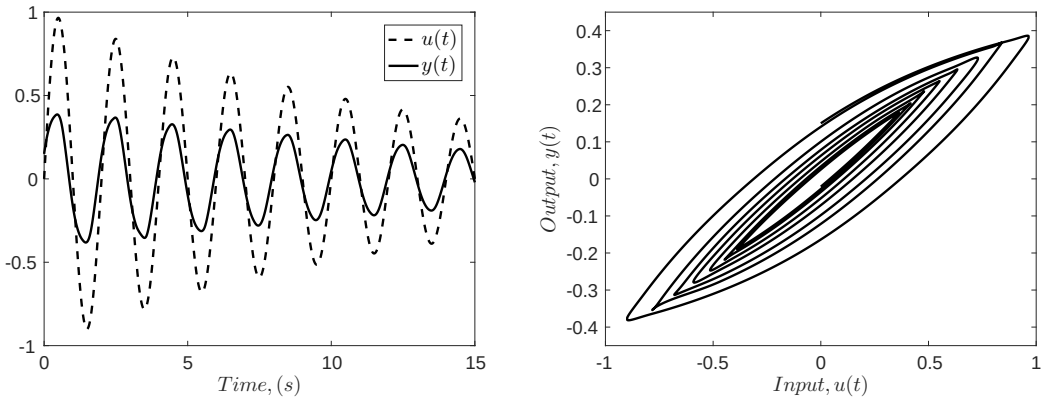

FIGURE 2.8: The input-output map of the Bouc-Wen model (2.26) with $\xi = 1$, $\varphi = 1$, $\gamma = 0.01$, $\rho = k = 0.5$ and $n = 1.25$.

described by the Duhem model (2.14) with

$$x_1(y(t), u(t)) = \beta|1 - \frac{y(t)}{\sigma}|^r sgn(1 - \frac{y(t)}{\sigma}), \tag{2.23a}$$

$$x_2(y(t), u(t)) = \beta|1 + \frac{y(t)}{\sigma}|^r sgn(1 + \frac{y(t)}{\sigma}). \tag{2.23b}$$

The Dahl model can be considered as a special case of the Duhem operator (Padthe et al., 2008). In Fig. 2.7, we illustrate the behaviour of input-output plot described by Dahl model where parameters σ, β, and r are chosen as $\sigma = 0.75$, $\beta = 1.5$ and $r = 3$.

2.2.2.5 Bouc-Wen Model

The model is initially proposed by Bouc in 1971 to describe the loading and unloading curves of the hysteresis loop. The model is subsequently modified by Wen in 1976 (Gu et al., 2016) and used mostly for predicting plastic deformations in mechanical systems. Due to its capability to describe and characterize a broad range of hysteretic systems, it has been extensively used in various applications namely smart actuators (Guo et al., 2011; Habineza et al., 2015; Wang and Mao, J. Q., 2010), magnetorheological dampers (Lin et al., 2013), as well as mechanical isolation systems (Cao and Chen, X. B., 2015; Manzoori and Nezhad, H. T., 2016). The general expression of Bouc-Wen (BW) model

is given as (Ikhouane and Rodellar, J., 2007)

$$y(t) = \rho k u(t) + (1-\rho)k w(t) \tag{2.24}$$

$$\dot{w}(t) = \xi \dot{u}(t) - \varphi|\dot{u}(t)||w(t)|^{n-1}w(t) - \gamma \dot{u}(t)|w(t)|^n,\ w(0) = w_0 \tag{2.25}$$

where $y(t)$ denotes the output of the BW model; $u(t)$ and $w(t)$ denote the applied input and the hysteresis state respectively; $0<\rho\leq 1$ is the weighting parameter; k is the stiffness coefficient; and ξ, φ, γ and $n \geq 1$ are the parameters which govern the shape and amplitude of the hysteresis curve.

Alternatively, the BW model (2.24)-(2.25) can be expressed as follows

$$\dot{y}(t) = (\rho k + k(1-\rho)(\xi - \varphi sgn(\dot{u})|\frac{y-\rho k u}{k(1-\rho)}|^{n-1}(\frac{y-\rho k u}{k(1-\rho)}) - \gamma|\frac{y-\rho k u}{k(1-\rho)}|^n))\dot{u}(t) \tag{2.26}$$

In view of (2.26), the Bouc-Wen model can be described by the Duhem model (2.14) with

$$x_1(y,u) = (\rho k + k(1-\rho)(\xi - \varphi|\frac{y-\rho k u}{k(1-\rho)}|^{n-1}(\frac{y-\rho k u}{k(1-\rho)}) - \gamma|\frac{y-\rho k u}{k(1-\rho)}|^n)), \tag{2.27a}$$

$$x_2(y,u) = (\rho k + k(1-\rho)(\xi + \varphi|\frac{y-\rho k u}{k(1-\rho)}|^{n-1}(\frac{y-\rho k u}{k(1-\rho)}) - \gamma|\frac{y-\rho k u}{k(1-\rho)}|^n)). \tag{2.27b}$$

Obviously, the BW model is also a variation of Duhem model. An illustration of the input-output relations described by BW model (2.26) is shown in Fig. 2.8.

2.3 System Identification in Hysteresis Characterization

Most of the models considered in the previous section consist of many parameters to build the shape of the hysteresis curve. In the first place, a suitable model has to be assigned to describe a nonlinear behavior of the system properly, and then the parameters of the proposed model have to be estimated. This matter can be considered from two different points of views. In one hand, an identifier can be designed and substituted into the model of the system for imitating behavior of the real system as nearly as possible with a minimum error. This kind of identification is known as non-parametric

identification. On the other hand, parameters of the proposed model can be estimated through an optimization tool. This type of identification is known as parametric identification in which the parameters of the system are estimated using several methods such as least mean square, recursive least square, genetic algorithm, particle swarm optimization, etc.

2.3.1 Least Square Identification

In this method, the unknown parameters in a certain model are estimated by finding numerical values for the parameters that minimize the sum of the squared deviations. Normally, the model is expressed in a regression form such as autoregressive with exogenous model (ARX), autoregressive-moving-average model (ARMA), autoregressive-moving-average with exogenous model (ARMAX), and so on.

For an illustration, consider a second-order discrete model of the ARX form given as

$$y(k) + a_1 y(k-1) + a_2 y(k-2) = a_3 u(k) + a_4 u(k-1) \tag{2.28}$$

The objective is to estimate the parameter vector $\theta^T = [a_1, \ a_2, \ a_3, \ a_4]$ using the vector of input and output measurements. Define,

$$\phi^T(k) = [-y(k-1), \ -y(k-2), \ u(k), \ u(k-1)] \tag{2.29}$$

Then, we can write (2.28) as follows

$$y(k) = \phi^T(k) \cdot \theta \tag{2.30}$$

In the least-square (LS) estimation, the following cost function is used

$$J(\hat{\theta}) = \sum_{k=1}^{N} [y(k) - \phi^T(k)\hat{\theta}]^2 \tag{2.31}$$

where $\phi^T(k)\hat{\theta}$ is the predicted output and $y(k)$ is the real output which measured in the experiment. To determine the parameter vector $\hat{\theta}$, the cost function (2.31) is minimized,

i.e., $\frac{dJ(\hat{\theta})}{d\hat{\theta}} = 0.$

$$\frac{dJ(\hat{\theta})}{d\hat{\theta}} = -2\sum_{k=1}^{N}\phi(k)(y(k) - \phi^T(k)\hat{\theta}) = 0 \tag{2.32}$$

in which we obtain $\hat{\theta}_N$ as

$$\hat{\theta}_N = \left(\sum_{k=1}^{N}\phi(k)\phi^T(k)\right)^{-1}\sum_{k=1}^{N}\phi(k)y(k) \tag{2.33}$$

Results on modeling and identification of hysteresis behaviour pertaining to the LS method can be found in Iyer and Shirley, M. E., 2004; Stakvik et al., 2015; Tan et al., 2001. The LS identification is also known as an off-line parameter estimation method. For on-line parameter estimation, it is extended to recursive least square (RLS) identification and is discussed in the following subsection.

2.3.2 Recursive Least Square Identification

In the recursive least square (RLS) technique, the evolution or estimation of parameters is updated at every time when a new set of observation data is obtained. Compared to LS approach, RLS algorithm has a faster convergence speed and do not exhibit the eigenvalue spread problem. However, it entailed more complicated mathematical operations and require more computational resources than LS method. The standard RLS algorithm is described as follows (Goodwin and Sin, K. S., 2009):

$$\hat{\theta}(k) = \hat{\theta}(k-1) + \frac{P(k-2)\phi(k-1)}{1+\phi^T(k-1)P(k-2)\phi(k-1)}(y(k) - \phi^T(k-1)\hat{\theta}(k-1)) \tag{2.34}$$

$$P(k-1) = P(k-2) - \frac{P(k-2)\phi(k-1)\phi^T(k-1)P(k-2)}{1+\phi^T(k-1)P(k-2)\phi(k-1)} \tag{2.35}$$

with $\hat{\theta}(0)$ given and $P(k-1)$ is any positive definite matrix P_0.

There are many variants of RLS algorithm that have been developed to solve the identification problems in the linear as well as nonlinear systems. For example, Zhang et al., 2013 apply an extended RLS method to adaptively identify the parameters of the controlled autoregressive moving average (CARMA) model which is used to describe the hysteresis phenomenon in a smart beam. In this study, the CARMA model is used

to characterize the relationship between the output strain near the fixed end of the cantilever beam and the input voltage applied on the piezoelectric actuator. It is shown that the hysteresis effects in the smart beam could be well identified by the above extended RLS algorithm.

Meanwhile, Zhou et al., 2013 proposed a variable step-size RLS estimation algorithm in order to reduce the computation overhead in the identification process. It is then used to identify the weighting parameters of the Krasnosel'skii-Pokrovskii model in modeling hysteresis nonlinearity of a magnetic shape memory alloy (MSMA) actuator. For a benchmarking purpose, an improved gradient correction identification method is used. Through simulation and experimental studies, it is verified that the variable step-size RLS has a better performance over the gradient approach.

2.3.3 Particle Swarm Optimization Method

The particle swarm optimization (PSO) method is inspired by the flocking and schooling patterns of birds and fish. Its establishment is relatively new (in the 1990s) in comparison to Genetic Algorithm (GA) and Fuzzy Logic (FL) but has become one of the most powerful methods for solving unconstrained and constrained global optimization problems (Bergh and Engelbrecht, A.P., 2006). Essentially, it consists of a number of individuals that denote particles to simulate social behavior that 'flying' around in a multidimensional search space. The individuals thus have a position and a velocity. The particles evaluate and update their positions with a fitness value at each iteration. By attracting the particles to better positions with good solutions, each particle remembers its own previously best-found position, and particles in the group (a.k.a swarm) share memories of their "best" positions, and then use those memories to adjust their own velocities, and thus subsequent positions.

The algorithm of the original PSO is described as follows (Hassani et al., 2014):

1. Initialize the time to zero and set a number for initial position $x_{(0)}^{i,d}$ and initial velocity $v_{(0)}^{i,d}$.

2. Evaluate the fitness of each particle $F(x_k^{i,d})$.

3. Set the $Pb_k^{i,d}$ to the better performance as follows

$$Pb_k^{i,d} = \begin{cases} Pb_{k-1}^{i,d}, & F(x_k^{i,d}) \geq F(Pb_{k-1}^{i,d}); \\ \\ x_k^{i,d}, & F(x_k^{i,d}) < F(Pb_{k-1}^{i,d}). \end{cases} \tag{2.36}$$

4. Set the $Gb_k^{i,d}$ to the position of particle with the best fitness within the swarm as

$$Gb_k^{i,d} \in Pb_k^{1,d}, Pb_k^{2,d}, \cdots, Pb_k^{N_s,d} / F(Gb_k^{i,d})$$
$$= min\{F(Pb_k^{1,d}), \cdots, F(Pb_k^{N_s,d})\}$$

5. Update the velocity vector for each particle according to the following rule:

$$v_{k+1}^{i,d} = V_{max}, \quad if \;\; v_k^{i,d} \geq V_{max} \tag{2.37a}$$

$$v_{k+1}^{i,d} = -V_{max}, \quad if \;\; vv_k^{i,d} < -V_{max} \tag{2.37b}$$

$$v_{k+1}^{i,d} = I_w \cdot v_k^{i,d} + \rho_1 \cdot r_1 \cdot (Pb_k^{i,d} - x_k^{i,d}) + \rho_2 \cdot r_2 \cdot (Gb_k^{i,d} - x_k^{i,d}), \quad otherwise \tag{2.37c}$$

6. Update the position of each particle according to

$$x_{k+1}^{i,d} = x_k^{i,d} + v_{k+1}^{i,d} \tag{2.38}$$

7. Let $k = k + 1$.

8. Compute the new $F(x_k^{i,d})$ until the iteration to be terminated or the least value for F to be achieved.

where I_w is inertia weight; ρ_1 is cognitive learning gain; ρ_2 is social learning gain; r_1 and r_2 are random numbers,uniformly distributed in the range of [0,1]; $Pb_k^{i,d}$ is the best known position along the dth dimension of particle i in iteration k; $Gb_k^{i,d}$ is the global best known position among all particles along the dth dimension in iteration k; and $k = 1, 2, \cdots, N$, denotes the iteration number, N is the maximum allowable iteration number. N_s is the population size. In addition, V_{max} is the maximum velocity evolution which is usually selected to be half of the length of the search space.

Since its establishment, it has been applied in many areas, such as function optimization, artificial neural network training, pattern classification and so forth (Pant et al., 2007). Among the advantages of PSO are including rapid convergence, less computation overhead, and ease of implementation. However, the standard PSO does exhibit some disadvantages: it is sometimes easy to be trapped in local minima, and the convergence rate decreased considerably in the later period of evolution; when reaching a near optimal solution, the algorithm stops optimizing, and thus the accuracy that the algorithm can achieve is limited (Yang et al., 2007).

To attend the aforementioned problems, the standard PSO has received various modifications and upgrades. For example, Evers and Ghalia, M. B., 2009 introduce a mechanism for overcoming the stagnation problem of PSO. This mechanism triggers the swarm regrouping whenever premature convergence is detected and helps liberate the swarm from the state of premature convergence in order to enable continued progress toward the true global minimum. In Alrasheed et al., 2007, a chaotic acceleration function is introduced into the PSO algorithm. The modified version of PSO is then empirically tested with the well-known benchmark functions include sphere, rosenbrock and rastrigin functions. A real case application is also considered to further evaluate the modified PSO. From the simulation and experimental results, it is proven that the modified version outperforms the standard PSO with better enhancement of convergence rate and accuracy. Other results related to the improvement of PSO technique are include Fan, 2002; Pant et al., 2007; Yang et al., 2007.

2.4 Control Strategies in Hysteretic Systems

Various control strategies have been developed to combat the hysteresis effects. In general, the control approach can be roughly classified into the open-loop or feedforward control, and the feedback control schemes (Cao and Chen, X. B., 2015; Devasia et al., 2007; Hassani et al., 2014).

2.4.1 Feedforward Approaches

In the feedforward control approach, the basic idea is to employ the inversion of a hysteresis operator for compensating the hysteretic behaviour. The common structure

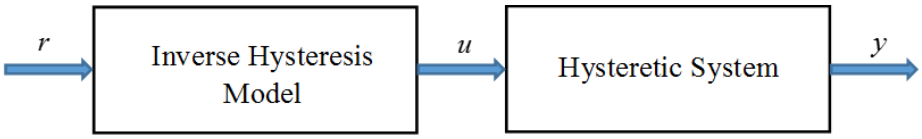

FIGURE 2.9: The block diagram of the inverse feedforward control scheme. y is the output of the inverse compensation, u is the control input, and r is the reference input.

of this strategy is shown in Fig. 2.9. The desired output r is fed through the inverse model to obtain the input signal u, which is then passed onto the physical plant, the output y of which will ideally be the desired signal.

Generally, this technique is devoted to the operator-based models i.e., the Preisach and P-I models such as reported by Al-Janaideh and Krejci, P., 2012; Chen et al., 2013; Krejci and Kuhnen, K., 2001; Tan and Baras, J. S., 2004. Comparing with the Preisach model, the P-I model has the advantage of the analytical inverse. Krejci and Kuhnen, K., 2001 are the pioneer to provide the analytical inverse of the classical P-I model. Since then, it can be seen that extensive works have been developed (Gu et al., 2014; Kuhnen, 2003; Tan et al., 2009). For the Preisach model, numerical method is mainly adopted to approximate its inversion (Ruderman and Bertram, T., 2010; Venkataraman and Krishnaprasad, P. S., 2000).

When the hysteresis is represented by DEB models such as the Duhem model, Dahl model, and BW model, the inverse construction is either impossible or extremely difficult to be obtained (Gu et al., 2016). In this case, a feedforward compensator is achieved by an alternative solution, known as multiplicative-inverse approach such as reported by Rakotondrabe, 2011 where the compensator is developed based on the BW model. In the same vein, Habineza et al., 2015 extend this approach to multiple degree of freedom (DOF) hysteretic systems.

The main challenge with such approaches is the modeling complexity and parameter sensitivity. Therefore, the performance of this control scheme is sensitive to errors in the plant transfer function, leading to problems such as divergence and instability. In practice, feedback control approaches are used to reduce the effects of uncertainties and disturbances which is discussed in the following subsection.

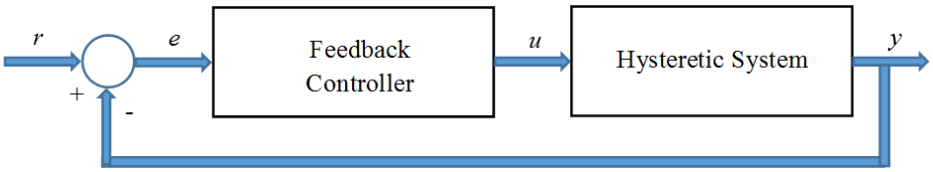

FIGURE 2.10: The block diagram of the feedback control scheme. y is the controlled output, u is the control input, and r is the reference input.

2.4.2 Feedback Approaches

In the feedback control scheme, hysteresis compensation is dealt by several approaches. Fig. 2.10 depicts the common structure of the feedback control scheme. The first approach is to directly develop a feedback controller without the use of hysteresis operators. The simplest solution is to consider the famous Proportional-Integral-Derivative (PID) control such as reported by Ikhouane and Rodellar, J., 2006. In this case, the PID controller is used to regulate the displacement and velocity of a second-order system that includes a dynamic hysteresis which is described by BW model. It is shown that the asymptotic regulation of the displacement and velocity can be achieved by the PID controller with a guaranteed stability of the closed loop signals.

In the second method, the system that is affected by the hysteresis is modeled by a composition of two terms namely, a linear term and a bounded disturbance-like term. In this way, available control methods are adequate to deal with the non-smooth hysteresis nonlinearity and different feedback control techniques have been proposed along this direction. Riccardi et al., 2013 come up with a control design strategy based on the PID controller to compensate hysteresis of a magnetic shape memory alloy-actuated positioning system. In this study, the linear matrix inequalities (LMI) based design tool is used to perform the numerical synthesis of the controller. Xu, 2015 presents the design of a second-order discrete-time terminal sliding-mode control strategy to address the tracking control problem of the PEA stage. Its establishment eliminates the use of the state observer because the designed control signal only depend on the output feedback. In Zhong and Yao, B., 2008, an adaptive controller framework is proposed to compensate for the effect of unknown model parameters and bounded disturbances effectively. The formulation of the control strategy takes the basis of a simple first-order nonlinear model with only four parameters.

Alternatively, control design and stability analysis methods are proposed based on

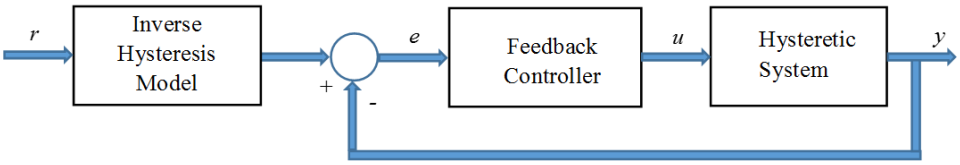

FIGURE 2.11: The block diagram of the feedforward-feedback control scheme with the closed-loop inversion. y is the controlled output, u is the control input, and r is the reference input.

the properties of hysteresis itself such as monotonicity, sector-bound or dissipativity to ensure that the formulated controller is robust against the parameter uncertainties and thus stable. For example, Gorbet et al., 2001 derive the dissipativity of the Preisach operator and design a controller, which is strictly passive for the smart actuators. Another result that is similar to this method can be found in (Jayawardhana et al., 2012).

2.4.3 Integration of Feedforward and Feedback

There are a number of feedforward-feedback control architectures that have been developed to further suppress the hysteresis effects and improve the overall systems' performance. Generally, in this strategy, the hysteresis nonlinearity is compensated by the approximation of the feedforward scheme (hysteresis inverse), while the feedback controller is designed to reduce the residual errors due to the inaccurate of hysteresis inverse model and the system uncertainties. This integration technique is initially introduced by Ge and Jouaneh, M., 1996 where they developed the inverse hysteresis compensator based on the Preisach model to mitigate the hysteresis effects and then combined it with a PID controller to eliminate the creep nonlinearity and modeling uncertainties of a piezoceramic actuator. Other results pertaining to this direction can be found in Cao et al., 2013; Chen et al., 2013; Shan and Leang, K. K., 2012; Xie et al., 2013. For example, Shan and Leang, K. K., 2012 present a thorough analysis relating to the effect of hysteresis on the stability of repetitive control (RC) strategy. P–I operator is used to characterizing the hysteresis effects. Then, the identified parameters of P-I operator are used to determine the bounds for a stable RC system. Different control strategies include Proportional-Integral (PI), a hybrid based of PI, RC and inverse P-I are considered to investigate the performance of RC based control scheme. Experiment results show a significant improvement in the tracking performance (such as a 71% reduction in tracking error) when the hybrid of PI-RC-inverse P-I control architecture is

used. The results are achieved without compromising the stability of the closed-loop system. Similar approach is reported in Riccardi et al., 2012.

Fig. 3.1 shows one of the feedforward-feedback control architecture reported for piezo-actuated nanopositioning stages (Devasia et al., 2007). In this case, the feedforward controller in Fig. 3.1 is the inversion of closed-loop system. It is demonstrated that this approach capable of reducing the computational error as the uncertainties and nonlinearities are compensated in advanced by the feedback control loop.

2.5 Concluding Remarks

This chapter elucidates the literature review, which describes previous studies related to this research. First, we discuss the conventional hysteresis models for characterizing the hysteresis effects in various applications and followed by system identification. Then, a discussion about control issues on smart actuators is presented.

Chapter 3

Modeling of Smart Actuators

3.1 Introduction

This chapter is focused on modeling of the hysteresis effects in the smart actuators. In order to solve the motion tracking problem in smart actuators, a good hysteresis model or operator is required. Indeed, there are many suitable candidates for this purpose. For example, we can consider physical based model which can accurately describe the input-output behaviour by considering almost all elements that actuator consists of. However, the developed model will be too complicated for direct implementation in the control design. To avoid this kind of limitation, in this thesis, we devote the focus onto the class of differential equations based (DEB) model. This consideration is due to its favourable properties that include a small number of parameters is required to describe the hysteresis phenomenon and the fact that differential equations, in general, are well-suitable for controller design purposes.

First, the analytical solutions pertaining to the DEB models namely Backlash model, Dahl model, and BW model are presented. Simulation experiments are also conducted to understand their physical meanings, similarities, and uniqueness. The insights provide important remarks on the models' feasibilities towards the control design. Then, a new model modification will be developed based on the outcome of above investigation with a goal to improve the characterization and control of hysteretic behaviour in the smart actuators. This development will be established in the discrete-time domain.

3.2 Analytical Solution of DEB Models

3.2.1 Backlash-like Model

The Backlash model (3.1) is the special case of Duhem model which is first appeared in Su et al., 2000.

$$\dot{y}(t) = b\dot{u}(t) - a|\dot{u}(t)|y(t) + c|\dot{u}(t)|u(t). \tag{3.1}$$

Based on (2.18)–(2.20) in Chapter 2, the solution of Eqn. (3.1) can be derived as follows

$$y(t) = \frac{c}{a} + \Psi(u) \tag{3.2}$$

where $\Psi(u)$ is defined as

$$\Psi(u) = (y_0 - (\frac{c}{a})u_0)e^{-a(u-u_0)sgn(\dot{u})} + (\frac{ab-c}{a^2})sgn(\dot{u})(1 - e^{-a(u-u_0)sgn(\dot{u})}). \tag{3.3}$$

In view of (2.20), $\Psi(u)$ of (3.2) is bounded by the following properties

$$\lim_{u\to+\infty} \Psi(u) = \lim_{u\to+\infty} (y(u : u_0, y_0) - \frac{c}{a}u) = \frac{ab-c}{a^2}, \quad \dot{u} > 0, \tag{3.4a}$$

$$\lim_{u\to-\infty} \Psi(u) = \lim_{u\to-\infty} (y(u : u_0, y_0) - \frac{c}{a}u) = -\frac{ab-c}{a^2}, \ \dot{u} < 0. \tag{3.4b}$$

It is important to note that (3.4) implies that there exists a uniform bound κ as such that

$$\|\Psi(u)\| \leq \kappa. \tag{3.5}$$

3.2.2 Dahl Model

For the simplest case, i.e., $r = 1$, the Dahl model (2.22) may be written as

$$\dot{y}(t) = \beta\dot{u}(t) - \alpha|\dot{u}(t)|y(t). \tag{3.6}$$

where α is defined as $\alpha = \frac{\beta}{\sigma}$.

The analytical solution of (3.6) is given by

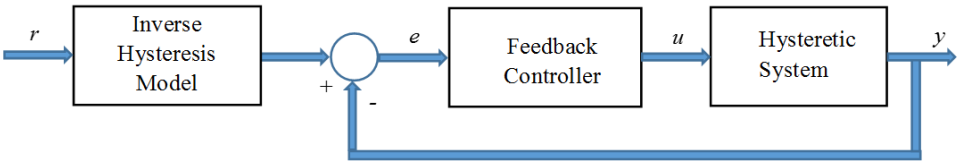

FIGURE 3.1: The block diagram of the feedforward-feedback control scheme with the closed-loop inversion. y is the controlled output, u is the control input, and r is the reference input.

$$y(t) = y_0 e^{-\alpha(u-u_0)sgn(\dot{u})} + \frac{\beta}{\alpha} sgn(\dot{u})(1 - e^{-\alpha(u-u_0)sgn(\dot{u})}). \tag{3.7}$$

It can be easily shown that (3.7) has similar properties as (3.4) for initial values (u_0, y_0), i.e., if $\dot{u} > 0$ or $\dot{u} < 0$ and $u \to +\infty$ or $u \to -\infty$, the following relations are obtained

$$\lim_{u \to +\infty} y(u : u_0, y_0) = \frac{\beta}{\alpha}, \quad \dot{u} > 0, \tag{3.8a}$$

$$\lim_{u \to -\infty} y(u : u_0, y_0) = -\frac{\beta}{\alpha}, \ \dot{u} < 0. \tag{3.8b}$$

A careful observation to Eqn. (3.6) and its properties (3.8) along with (3.1) and (3.4) lead to a conclusion that the hysteresis curves generated by both (3.1) and (3.6) would share similar shape.

3.2.3 Bouc-Wen Model

For $n = 1$, $k = 1$, and $\rho = 0$, BW model (2.26) can be rewritten as follows

$$\dot{y}(t) = \xi \dot{u}(t) - \varphi |\dot{u}(t)| y(t) - \gamma \dot{u}(t) |y(t)|. \tag{3.9}$$

Eqn. (3.9) is known as a special case of Bouc-Wen model. The output $y(t)$ of (3.9) is bounded with a bound given as in the following form (Zhou et al., 2012)

$$|y(t)| \leq \frac{\xi}{\varphi + \gamma} \tag{3.10}$$

For later developments, relation (3.9) is simplified as follows:

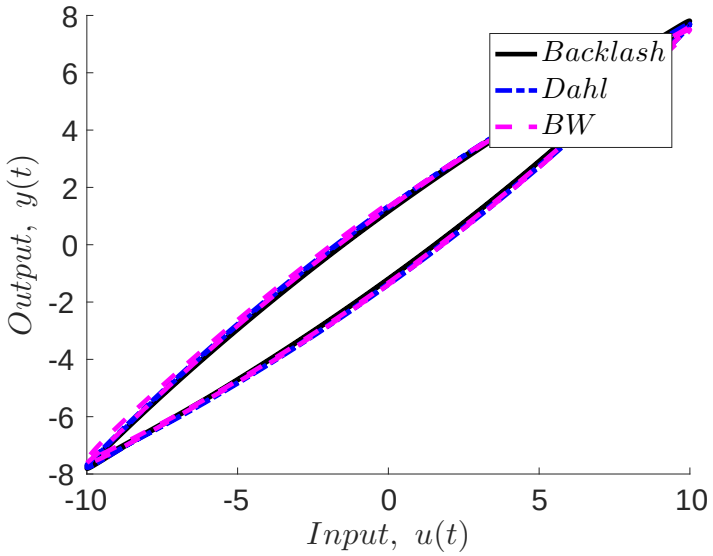

FIGURE 3.2: Hysteresis curves generated by Backlash model, Dahl model, and Bouc-Wen model with $a = 0.035$, $b = 0.8$, $c = 0.003$.

$$\dot{y}(t) = (\xi - |y|\mu(\dot{u}(t), y(t)))\dot{u}(t) \tag{3.11}$$

where $\mu(\dot{u}(t), y(t))$ is defined as

$$\mu(\dot{u}(t), y(t)) = \varphi sgn(\dot{u}(t))sgn(y(t)) + \gamma \tag{3.12}$$

The above analytical solutions provide the basis of selecting the parameter value for each model, in particular the parameter a in (3.1), α in (3.6), or φ in relation (3.9), i.e., it must be strictly positive to avoid exponential divergence and to preserve the existence of the hysteretic nonlinearity. In addition, we also learn that all the DEB models are bounded. This is an important property in the control design and stability analysis. Other physical meanings pertaining to each parameter are studied and discussed in the next section.

3.3 Simulation Analysis

In the first analysis, a sinusoidal input signal $u = 10sin(2\pi t)$ is used to simulate the hysteresis curves. Fig. 3.2 shows the generated hysteresis curves for each model with the chosen parameter values as $a = \alpha = \varphi$, $b = \beta = \xi$, and $c = \gamma$. As can be seen in Fig. 3.2, the hysteresis curves described by each model is identical to each other.

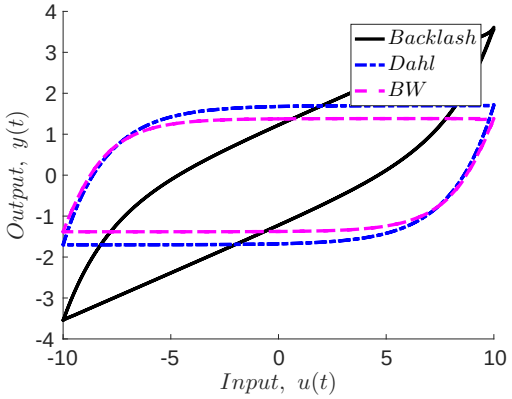

(A) Input of $u = 10sin(2\pi t)$.

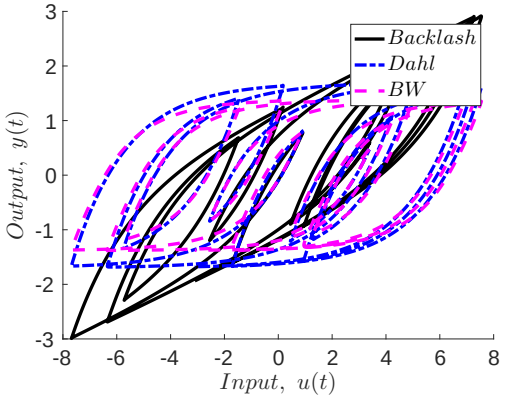

(B) Input of $u = 3.6sin(\pi t) + 3.1cos(3.4\pi t)$.

FIGURE 3.3: Hysteresis curves generated by Backlash model, Dahl model, and Bouc-Wen model with $a = 0.5$, $b = 0.85$, $c = 0.115$.

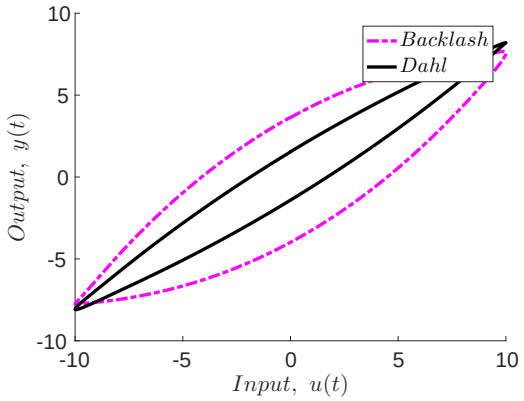

(A) The curves of Dahl and Backlash models.

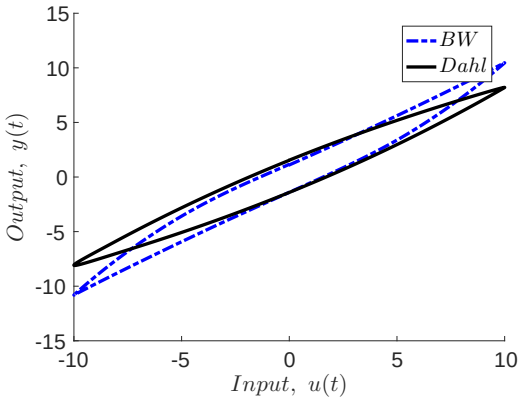

(B) The curves of Dahl and Bouc-Wen models.

FIGURE 3.4: Hysteresis curves generated by Backlash model, Dahl model, and Bouc-Wen model with $a = 0.035$, $b = 0.85$, $c = -0.05$ and $u = 10sin(2\pi t)$.

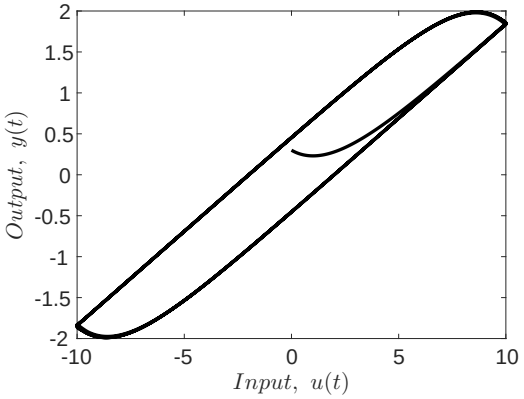

(A) Input of $u = 10sin(2\pi t)$.

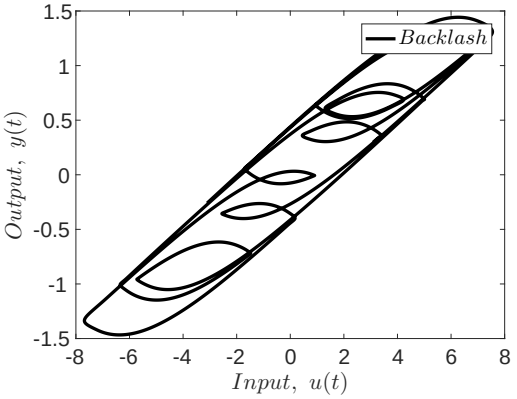

(B) Input of $u = 3.6sin(\pi t) + 3.1cos(3.4\pi t)$.

FIGURE 3.5: Input-output map for the partial Backlash model with $a = 0.5$, $c = 0.115$.

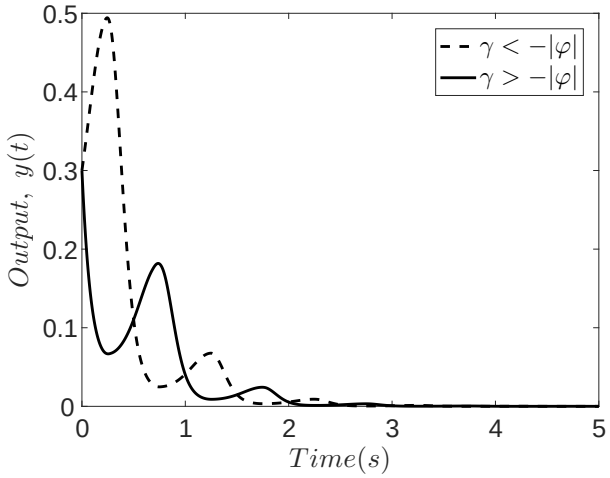

FIGURE 3.6: Output behaviour of the nonlinear terms of Bouc-Wen model with $\varphi = 0.05$. (Dashed) $\gamma < -|\varphi|$. (Solid) $\gamma > -|\varphi|$.

This scenario occurs when the parameters c and γ are kept much smaller than other parameters, specifically within [0,1).

A subtle difference can be observed as the parameter c or γ is increased or decreased; this parameter makes the Backlash or the BW model distinct to the Dahl model. Parameter c physically change the gradient of the curves while γ reflects the upper and the lower branch of the curves as depicted in Fig. 3.3 (for positive c or positive γ) and Fig. 3.4 (negative c, i.e. $c < -|a|$ or negative γ, i.e., $\gamma < -|\varphi|$). In this simulation study, the parameters for each model are set as the same condition as in the first first analysis, i.e., $a = \alpha = \varphi$, $b = \beta = \xi$, and $c = \gamma$. An important observation relating to the Backlash model that can be made is that by setting b to zero in (3.1), the remaining relations can still yield hysteresis curves as illustrated in Fig. 3.5. Note that the orientation of the hysteresis curves depicted in Fig. 3.5 is the opposite of the one described in either Fig. 3.2, Fig. 3.3, or Fig. 3.4. Normally, when the output lags the input, the phase plot of the input-output signals undergoes a counter-clockwise behaviour and this type of phenomena is called counter-clockwise (CCW) input-output behaviour. For example, Preisach model with positive weights generates CCW curves. On the other hand, when the output leads the input, the phase plot of the input-output signals undergoes a clockwise (CW) behaviour. Note that the original form of Backlash model generates CW hysteresis curves and once the linear term is removed from the equation, i.e., $b = 0$, CCW curves are observed.

Nonetheless, BW model loses its ability to describe the hysteretic effects when the

linear term is removed. However, we wish to investigate the physical meaning of γ with respect to the input $u(t)$. The plot of $\mu(\dot{u}(t), y(t))$ (3.12) with $y(u_0) = y_0$ is shown in Fig. 3.6. It is apparent from Fig. 3.6 that γ can be less than $|\varphi|$ or vice-versa to yield an exponential decay behaviour. In addition, the convergence speed can be adjusted by a proper selection of γ value. Positive value of γ reflects a slight increment to convergence speed (negative value is conversely).

3.4 Discrete-Time Modeling

It is obvious that Duhem model (for example Backlash model) is capable of describing complex hysteresis curves that are akin to hysteresis phenomenon in the real applications. However, it is a challenge to determine proper shape functions that best describe real hysteresis effects. Furthermore, a good model does not guarantee its viability from a control standpoint.

Generally, the class of DEB model is used to describe a disturbance or uncertainty term due to its boundedness property(Xu and Li, Y., 2010). Then, linear ordinary differential equation (ODE) is commonly used to describe the hysteretic systems so that the standard control approach can be applied, while the bounded disturbance is assumed to be fed into either the input or the output channel of the system.

However, when hysteresis nonlinearities are described by the class of DEB model, the major challenge is the corresponding controller design due to the presence of variable $|\dot{u}|$. This situation makes control input depends on the sign function $sgn(\dot{u})$ which is not available in practice. Based on our analysis, only BW model is found to be successful in terms of direct model usage for the control design. The key point to this success lies in its unique structure that allows control designer to handle the $|\dot{u}|$ term appropriately. By introducing a specific restriction to parameter γ, the sign of $\mu(\dot{u}, y)$ term in (3.12) can be set to either positive or vice-versa depending on the control law requirement. In other terms, the control input will be independent of the sign function $sgn(\dot{u})$. This point is important because without any restriction to parameter γ, stability of closed-loop system can not be guaranteed.

Realizing this fact, BW model is adopted to solve the problem of characterization

and control in the smart actuators. First, a procedure for discretizing the continuous-time BW model is presented in the following subsection. Next, a new model modification to the original BW is proposed in Subsection 3.4.2. This model modification is proposed to fix the rate-independent property of the original BW model. In this case, the special case of BW model (3.9) is used as the basis for developing the modified one and its establishment is realized in the discrete-time domain. Then, control fusion methods are presented in Chapter 4 and Chapter 5. In Chapter 4, a discrete prescribed performance control (DPPC) is developed and fused into the modified BW (MBW) model. For evaluation purpose, a piezoelectrically actuated positioning system (PEA stage) is considered as the test rig. Chapter 5 describes the development of an adaptive control framework based on the MBW model along with stability analysis pertaining to closed-loop system. The control algorithm is then applied to a hysteretic GMA.

3.4.1 Discrete time Bouc-Wen model

Essentially, the discretization method is based on Taylor Series Expansion. Consider the following simple approximation of a first order derivative

$$y(t+\Delta t) = y(t) + \dot{y}(t)\cdot\Delta t + \ddot{y}(\varsigma)\cdot\frac{\Delta t^2}{2} \tag{3.13}$$

where $\varsigma \in (t, t+\Delta t)$; Δt is the sampling period; $t = k\Delta t$ is the sampling instant.

If $y(t) \neq 0$ and upon a simple rearrangement, the following relation is obtained

$$\dot{y}(t) = \frac{y(t+\Delta t) - (1-\vartheta_1)y(t)}{\Delta t} \tag{3.14}$$

in which $\vartheta_1 = (\frac{\ddot{y}(\varsigma)}{y(t)}\cdot\frac{\Delta t^2}{2})$ is defined as a higher order positive function of Δt. If the sampling period Δt is chosen to be very small, then $(1-\vartheta_1)$ will be nearly equal to 1. Thus, the derivative $\dot{y}(t)$ can be approximately expressed as

$$\dot{y}(t) \cong \frac{y(t+\Delta t) - \delta_1 y(t)}{\Delta t} \tag{3.15}$$

where δ_1 is a parameter which is nearly equal to 1 when Δt is sufficiently small. It can be easily seen that (3.15) is also valid even if $y(t) = 0$.

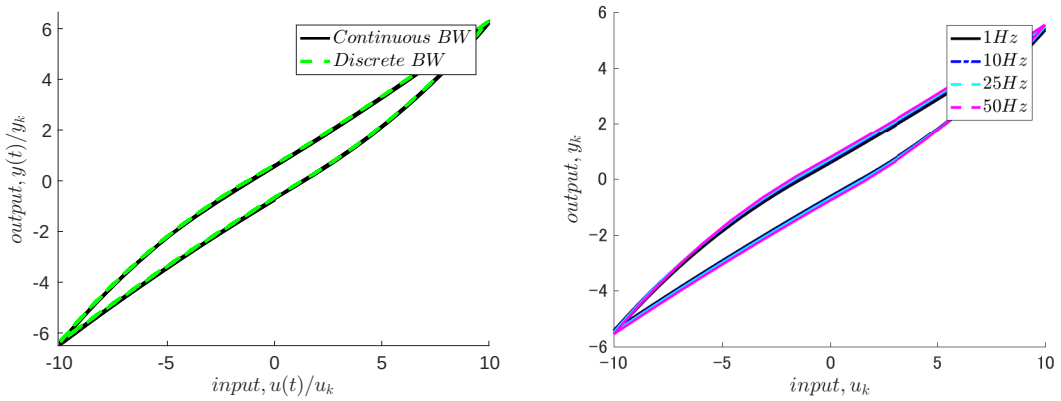

(A) Comparison of input-output relations by (3.9) and (3.19).

(B) Comparison of input-output relations described by (3.19) at different frequencies

FIGURE 3.7: The plots of input-output relations described by continuous BW model (3.9) and discrete BW model (3.19).

Similarly, $\dot{u}(t)$ can also be approximately expressed as

$$\dot{u}(t) \cong \frac{u(t+\Delta t) - \delta_2 u(t)}{\Delta t} \tag{3.16}$$

where δ_2 is a parameter which is nearly equal to 1 when Δt is sufficiently small.

In view of (3.15) – (3.16), Eqn. (3.9) can be expressed as

$$\begin{aligned} y(k\Delta t + \Delta t) = \delta_1 y(k\Delta t) + \Delta t\xi \frac{u(k\Delta t + \Delta t) - \delta_2 u(k\Delta t)}{\Delta t} \\ - \Delta t\varphi |\frac{u(k\Delta t + \Delta t) - \delta_2 u(k\Delta t)}{\Delta t}| y(k\Delta t) \\ - \Delta t\gamma \frac{u(k\Delta t + \Delta t) - \delta_2 u(k\Delta t)}{\Delta t} |y(k\Delta t)| \end{aligned} \tag{3.17}$$

For simplicity, denote $k\Delta t$ as k and define

$$\nu_k = \frac{u_k - \delta_2 u_{k-1}}{\Delta t}, \quad \zeta = \Delta t\xi, \quad \psi = \Delta t\varphi, \quad \alpha = \Delta t\gamma \tag{3.18}$$

Then, Eqn. (3.17) can be further simplified as

$$y_k = \delta_1 y_{k-1} + \zeta\nu_k - \psi|\nu_k|y_{k-1} - \alpha\nu_k|y_{k-1}| \tag{3.19}$$

Relation (3.19) is the representation of BW model in the discrete-time domain. Figure 3.7a shows the plot of hysteresis curves described by continuous BW model (3.9) and discrete BW model (3.19) where the parameters of both models are chosen as

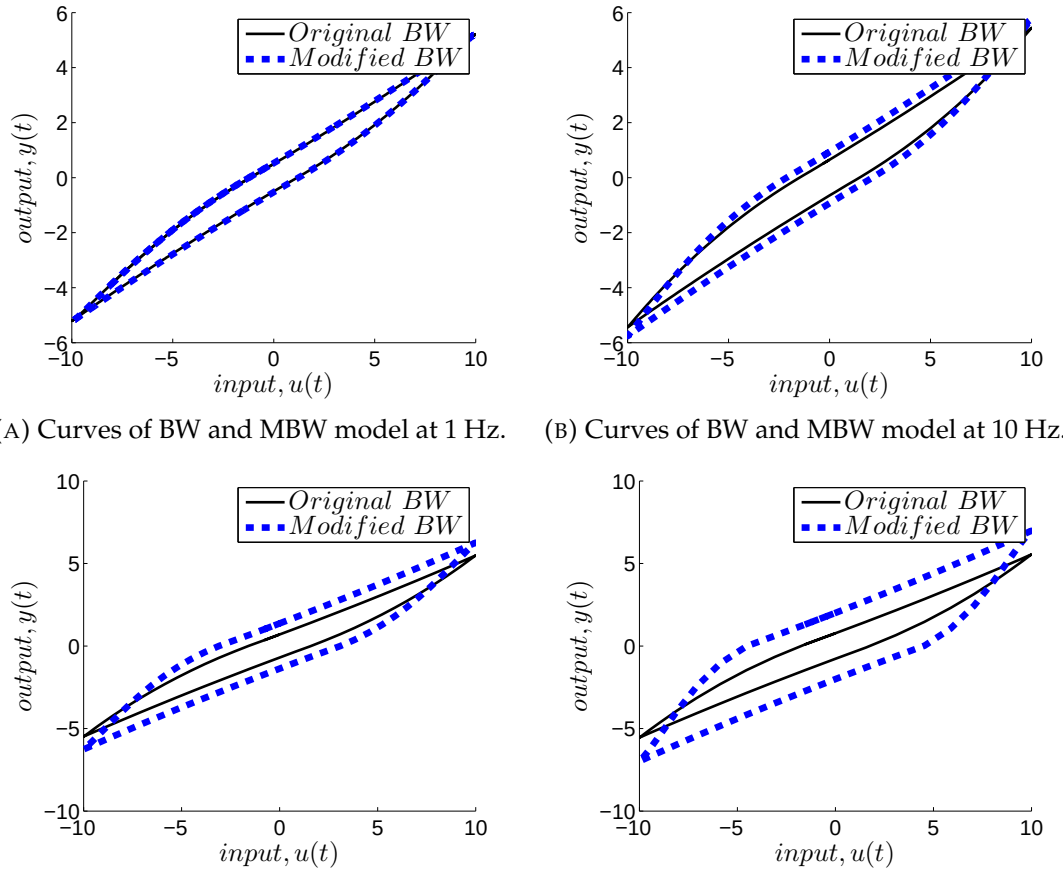

(A) Curves of BW and MBW model at 1 Hz.

(B) Curves of BW and MBW model at 10 Hz.

(C) Curves of BW and MBW model at 25 Hz.

(D) Curves of BW and MBW model at 50 Hz.

FIGURE 3.8: The comparison of input-output plots between the original BW model (solid) and MBW model (Dashed) at different frequencies.

$\zeta = \xi = 0.5$, $\psi = \varphi = 0.02$, $\alpha = \gamma = -0.05$, and $\delta_1 = \delta_2 = 0.9998$, while, the sampling period is set as $0.5ms$. As can be observed in Figure 3.7a, the hysteresis curves described by the discrete BW model are well matched with the continuous ones. The reconstruction accuracy is about 97%.

3.4.2 The Modified Discrete-Time Bouc-Wen Model

From the literature, it is well known that BW model is rate-independent, i.e., limited to describing invariant hysteresis curves regardless the increment/decrement of the input frequency. This behaviour can be clearly seen in Fig. 3.7b. Besides, hysteretic effects found in most smart materials, especially in ferromagnetic and ferroelectric materials are rate-dependent. In such cases, the use of standard BW model could yield considerable errors under inputs that are applied at varying rates.

To the best of our knowledge, there are a number of extensions of BW model which have been reported in the literature, but the most significant model improvements are as described by Song and Der Kiureghian, A., 2006; Wang et al., 2015a. In Song and Der Kiureghian, A., 2006, additional nonlinear terms are introduced into the standard BW form that not only depend on the sign of the input derivative but also the input itself. This extension offers better flexibility in shape control and is capable of describing highly asymmetric hysteresis curves with the time-invariant parameters. Meanwhile, the extension proposed by Wang et al., 2015a is essentially based on the addition of a further nonlinear memoryless function, i.e., a polynomial input function is introduced in cascade with the standard BW model which has locally Lipschitz continuous property. It is observed that both of these extensions require meticulous identification methods to yield satisfactory results. Additionally, none of them could be directly synthesized into the control design due to the special structure of their input functions.

To solve and improve above limitations, Eqn. (3.19) is further modified by introducing the first-order input difference term, $v_{u,k}$ which is defined as

$$v_{u,k} = |u_k - u_{k-1}| \tag{3.20}$$

Then, the modified BW (MBW) model is given as follows:

$$\begin{aligned} y_k = \delta_1 y_{k-1} + (\zeta_1 + \zeta_2 v_{u,k})\nu_k - (\psi_1 + \psi_2 v_{u,k})|\nu_k| y_{k-1} \\ - (\alpha_1 + \alpha_2 v_{u,k})\nu_k |y_{k-1}| \end{aligned} \tag{3.21}$$

Remark 3.1: The introduced first-order input difference term $v_{u,k}$ ensures that the generated hysteresis curves are varying to the speed of input variations, in other terms, the MBW model is a dynamic or rate-dependent hysteresis operator.

To illustrate ***Remark 3.1***, simulation experiments are conducted to compare the input-output curves described by the original BW model (3.19) and the proposed MBW model (3.21) where sinusoidal input of $u_k = 10sin(2\pi * Hz * k * 0.0005)$ is used. In this case, four different frequencies, namely $1\ Hz$, $10\ Hz$, $25\ Hz$, and $50\ Hz$ are studied. The parameters of both models are chosen as $\zeta = \zeta_1 = 0.4346$, $\psi = \psi_1 = 0.0345$, $\alpha = \alpha_1 = -0.05$, $\zeta_2 = 1e-6$, $\psi_2 = 0.09$, $\alpha_2 = -0.09$, and $\delta_1 = \delta_2 = 0.9995$. As can

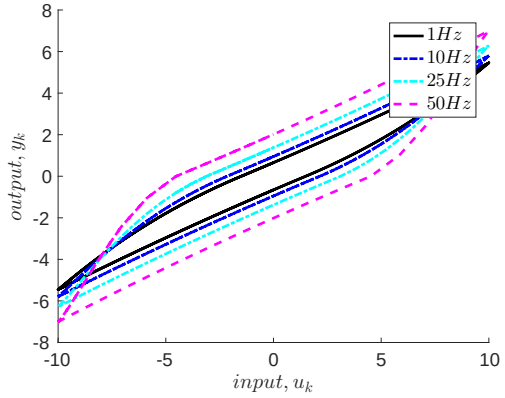

(A) Curves of MBW model at $1Hz - 50Hz$ with $v_{u,k}$ is chosen as (3.20).

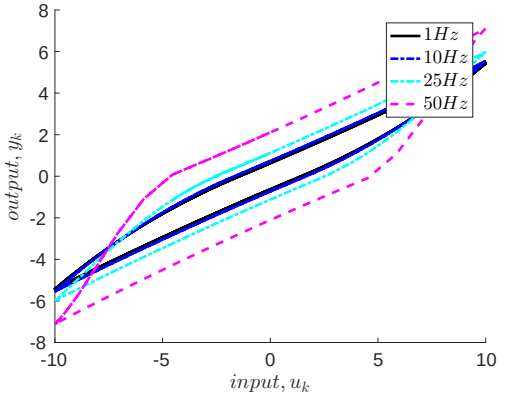

(B) Curves of MBW model at $1Hz - 50Hz$ with $v_{u,k}$ is chosen as $v_{u,k} = |(u_k - u_{k-1})^2|$.

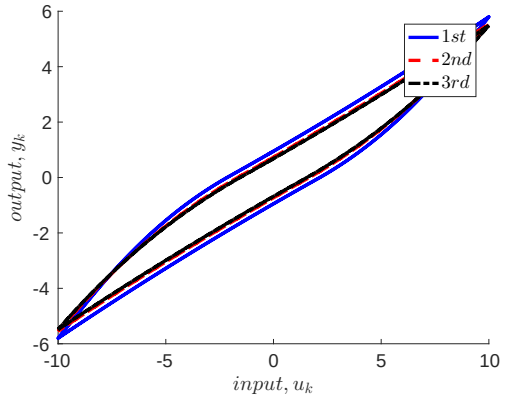

(C) Curves of MBW model at $10Hz$ with $v_{u,k}$ is chosen as $1st$, $2nd$, and $3rd$ order difference.

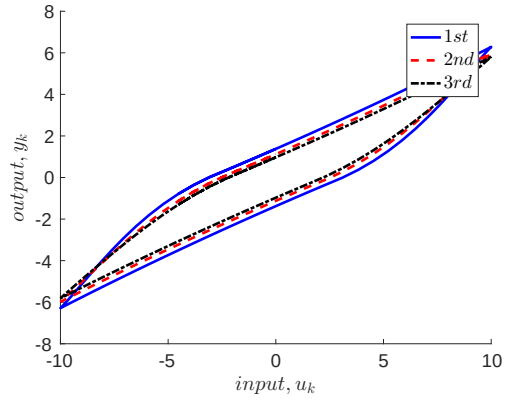

(D) Curves of MBW model at $25Hz$ with $v_{u,k}$ is chosen as $1st$, $2nd$, and $3rd$ order difference.

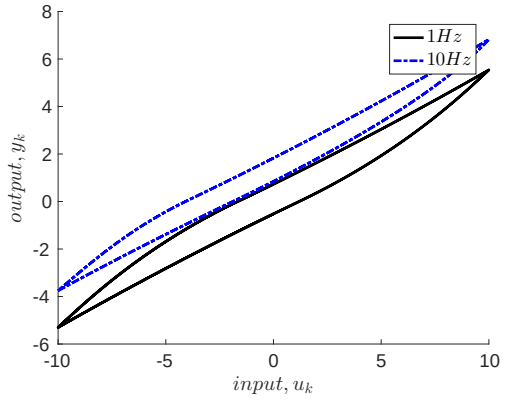

(E) Curves of MBW model at $1Hz - 10Hz$ with $v_{u,k}$ is chosen as $v_{u,k} = u_k - u_{k-1}$.

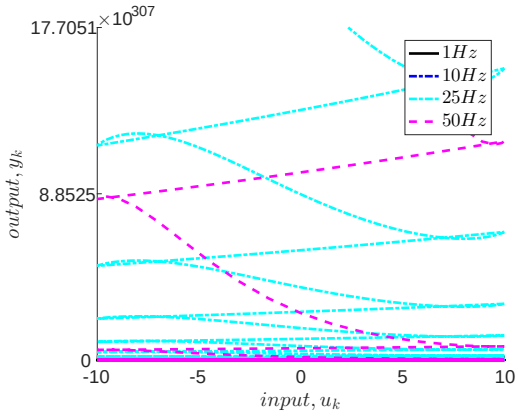

(F) Curves of MBW model at $1Hz - 50Hz$ with $v_{u,k}$ is chosen as $v_{u,k} = u_k - u_{k-1}$.

FIGURE 3.9: The comparison of input-output plots described by MBW model under various choices of $v_{u,k}$.

be noticed in Fig. 3.8, the curves described by MBW model are vary with respect to the increment of input frequency. While the curves described by the original BW model remain unchanged regardless the frequency changes.

In-fact, higher order difference term $v_{u,k}$ can be used to include rate-dependent property to BW model (3.19) as illustrated in Fig. 3.9b through Fig. 3.9d. Obviously, by increasing the order of difference term $v_{u,k}$, shape of input-output curves become thinner as input frequency is increasing.

However, without absolute term as described in (3.20), i.e., when $v_{u,k}$ is chosen as $v_{u,k} = u_k - u_{k-1}$, hysteresis curves will be offset along y–axis and as input frequency is increased, and the MBW model will no longer able describe hysteresis curves as can be observed in Fig.3.9e and Fig.3.9f. For this reason, in the following developments, we only consider $v_{u,k}$ as described by relation (3.20).

3.4.3 Model Validation

By and large, the least square identification method is usually used to estimate the parameters of a certain model. However, the nonlinear nature of Eqn. (3.21) increases the difficulty of parameter estimation process. Therefore, the common identification technique is not effective to yield best result. In order to validate the proposed model, we consider the extended version of Particle Swarm Optimization (EPSO) technique which adopted from Alrasheed et al., 2007 to effectively estimate the parameters of MBW model. In the standard PSO, the particles are tend to be trapped in the local minima. As a result, the particles are unable to adequately explore the feasible domain and yield to a premature solution. The proposed EPSO is incorporated with a chaotic acceleration function to ensure that the particles properly explore the search space, and thus improve quality of the solution. The chaotic acceleration function is defined as

$$\vartheta_{k+1} = \eta \cdot \vartheta_k(1 - \vartheta_k) \tag{3.22}$$

in which η is a positive constant.

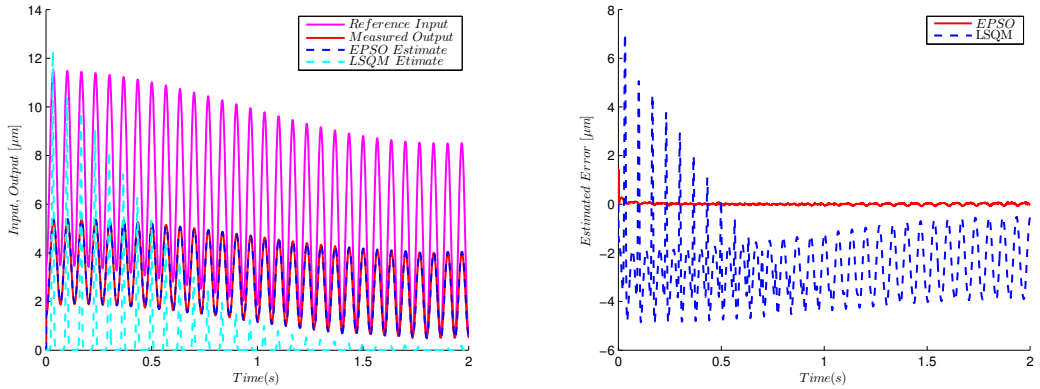

FIGURE 3.10: The graph of input-output relations obtained from experiment (solid) and MBW model (Dashed) using identified parameters (A sinusoidal input case of PEA).

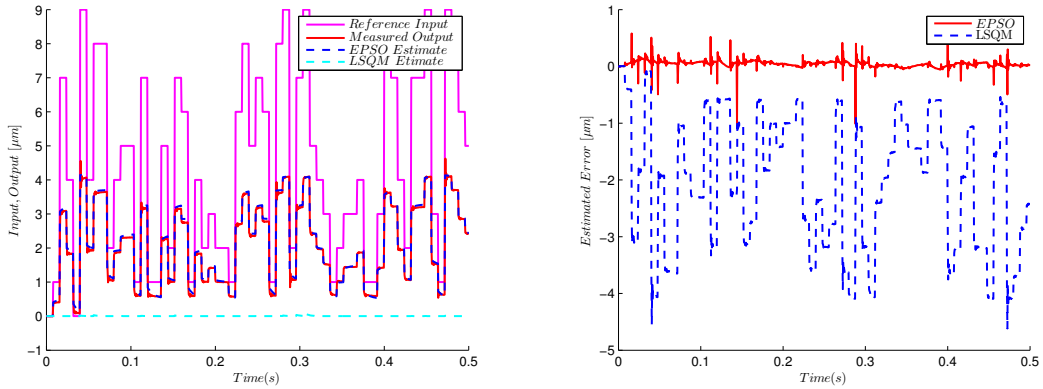

FIGURE 3.11: The graph of input-output relations obtained from experiment (solid) and MBW model (Dashed) using identified parameters (A random input case of PEA.)

Then, the velocity and position updates which are described in (2.37) and (2.38) are modified as in Eqn. (3.23) and Eqn. (3.24) respectively.

$$v_{k+1}^{i,d} = I_w \cdot v_k^{i,d} + \rho_1 \cdot r_1 \cdot (Pb_k^{i,d} - x_k^{i,d}) + \vartheta_k \cdot \rho_2 \cdot r_2 \cdot (Gb_k^{i,d} - x_k^{i,d}) \tag{3.23}$$

$$x_{k+1}^{i,d} = x_k^{i,d} + \vartheta_k \cdot v_{k+1}^{i,d} \tag{3.24}$$

Empirical studies of PSO pertaining to the inertia weight I_w have shown that a relatively large I_w has more global search ability while a relatively small I_w results in a faster convergence (Yang et al., 2007). In this validation process, the inertia weight I_w is defined as follows

$$I_w = I_{w,max} - \frac{(I_{w,max} - I_{w,min})e^{-0.02\vartheta_k} \cdot k}{N} \tag{3.25}$$

where $I_{w,max}$ is the maximum inertia weight which is set as 0.9, and $I_{w,min}$ is the minimum inertia weight, and is set to 0.2. Eqn. (3.25) is a dynamic inertia weight designed to trade-off between the search ability and convergence rate.

TABLE 3.1: The selected parameter bounds for the identification process.

Parameter	Lower Bound values	Upper Bound values
ζ_1	0.00001	0.9
ζ_2	0.00001	1.0
ψ_1	0.00001	0.95
ψ_2	-1.0	1.0
α_1	-0.00001	0.9
α_2	-1.0	1.0

Experimental data from three types of smart-material based actuators are considered namely, a piezoelectric actuator (PEA), a giant-magnetostrictive actuator (GMA), and an ionic polymer metal composites actuator (IPMC) to study the capacity of the proposed model in fitting and matching the real input-output relations. In this case, the cost function is described by the root mean-square error (RMSE) as in Eqn. (3.26).

$$J_{RSME} = \sqrt{\frac{\sum_{n=1}^{L}(Y_{exp}^n - Y_{MBW}^n)^2}{L}} \tag{3.26}$$

where Y_{exp}^n is the measured experiment data at the nth sampling instant, Y_{MBW}^n is the corresponding estimated output from the MBW model, and L is the total number of samples. In order to fit the MBW model output and experimental data accurately, the following fitness function is considered

$$f(\zeta_1, \zeta_2, \psi_1, \psi_2, \alpha_1, \alpha_2) = min(J_{RSME}) \tag{3.27}$$

In the simulation study, the parameters of EPSO algorithm are chosen as $\rho_1 = 1.5$, $\rho_2 = 2.5$, and $\eta = 4.0$. In addition, the population size N_s is set as 40 particles and the chaotic function is initiated by a random number. By experiential judgement, the parameter bounds are set as in Table 3.1. For a benchmarking purpose, we consider the

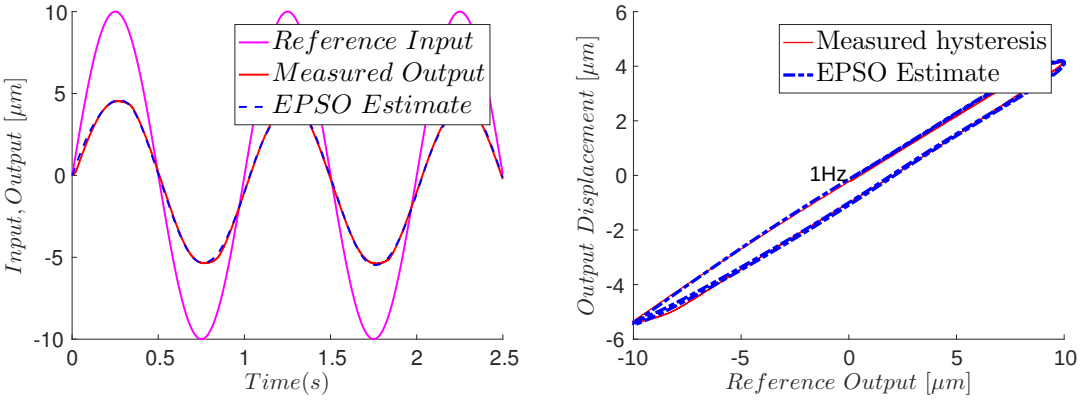

FIGURE 3.12: Comparison of input-output map between experimental data of the PEA (Solid) and MBW model (Dashed) at $1Hz$

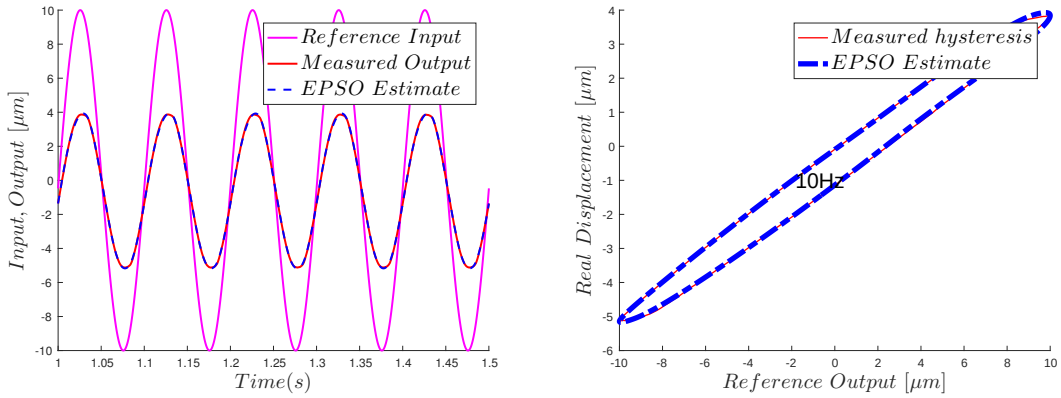

FIGURE 3.13: Comparison of input-output map between experimental data of the PEA (Solid) and MBW model (Dashed) at $10Hz$.

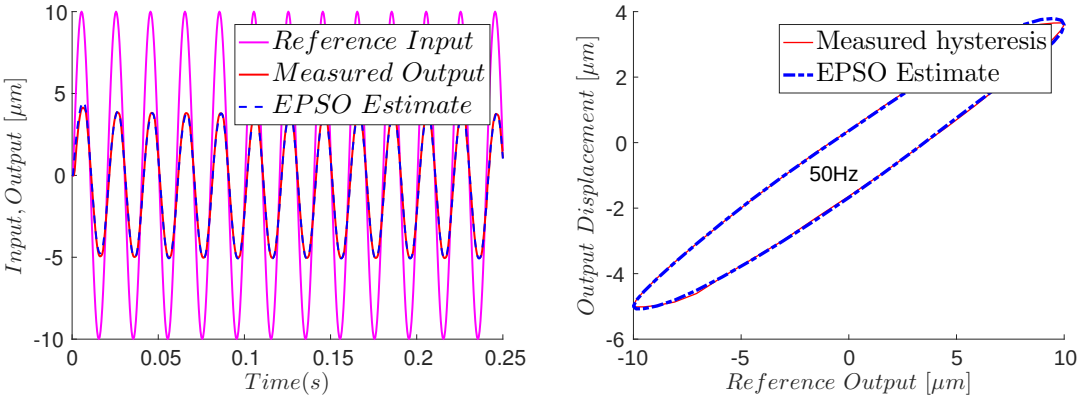

FIGURE 3.14: Comparison of input-output map between experimental data of the PEA (Solid) and MBW model (Dashed) at $50Hz$.

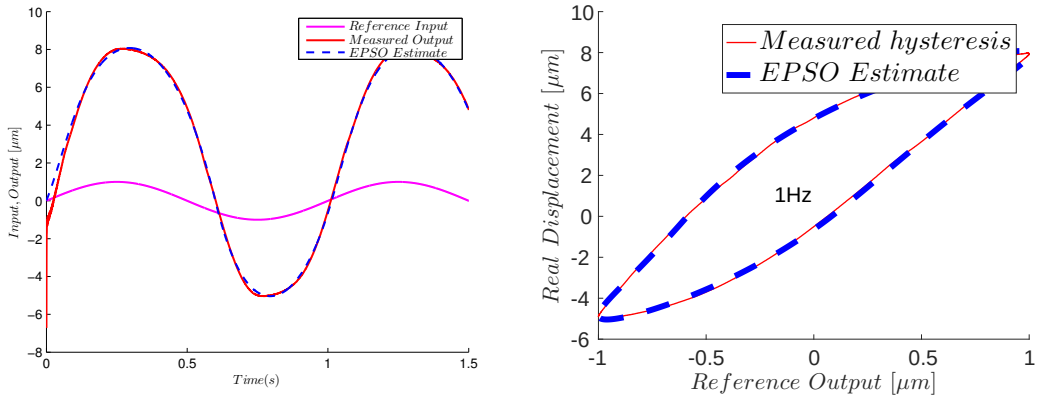

FIGURE 3.15: Comparison of input-output map between experimental data of the GMA (Solid) and MBW model (Dashed) at $1Hz$.

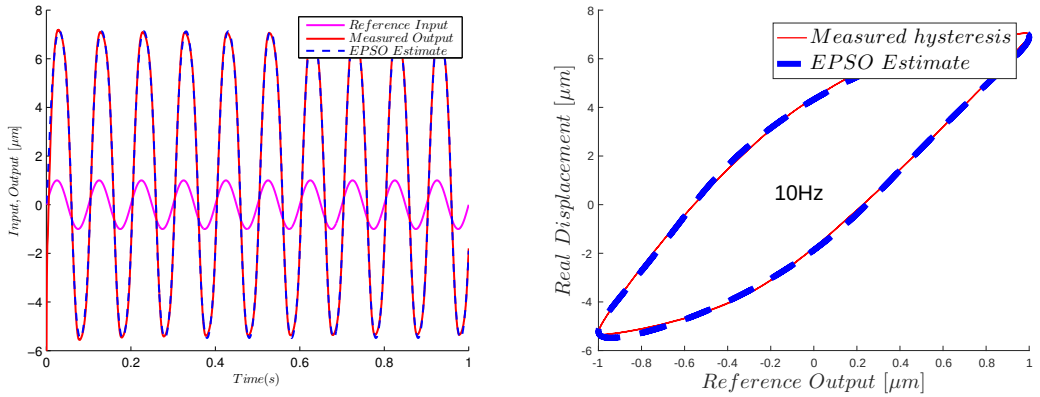

FIGURE 3.16: Comparison of input-output map between experimental data of the GMA (Solid) and MBW model (Dashed) at $10Hz$.

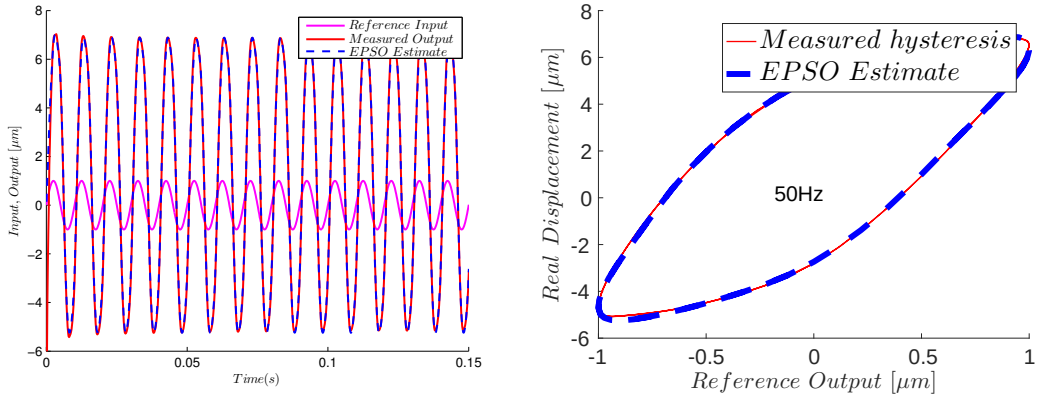

FIGURE 3.17: Comparison of input-output map between experimental data of the GMA (Solid) and MBW model (Dashed) at $50Hz$.

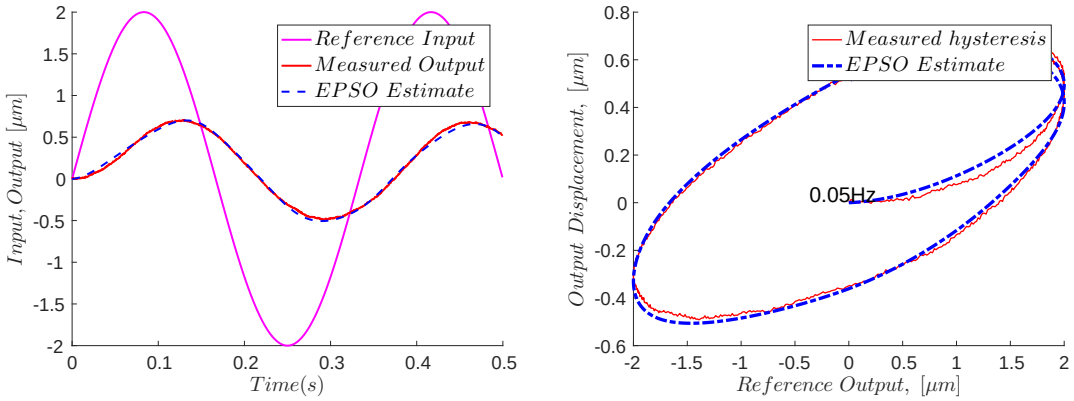

FIGURE 3.18: The graph of input-output relations obtained from experiment (solid) and MBW model (Dashed) using identified parameters the case of IPMC at $0.05Hz$.

standard nonlinear least square curve fitting method (LSQM) provided by MATLAB software. In this case, the parameter bounds are set to be the same for both methods.

Fig. 3.10 compares the input-output relations measured in the experiments (PEA) to those obtained through the simulations based on the identified parameters. Referring to Fig. 3.10, it is clear that, EPSO performs much better than the LSQM. The RMSE for both methods are recorded as $0.0318\mu m$ for EPSO and $2.9363\mu m$ for LSQM.

While Fig. 3.11 further illustrates the effectiveness of EPSO. In this case, a random input is used to check and verify whether EPSO algorithm is able to escape from the local minima. By the help of EPSO technique, it can be seen the output generated by MBW model is well matched with the measured output of PEA. The LSQM, on the other hand, is stuck in the local minima and is unable to yield a good result. The recorded RMSE values for this case are $0.0993\mu m$ (EPSO) and $2.4297\mu m$ (LSQM).

Additionally, Fig. 3.12 through Fig. 3.17 indicate hysteresis curves measured in the experiments of both PEA stage and GMA to those obtained through MBW model (3.21) with the identified parameters (by EPSO) at $1Hz$, $10Hz$ and $50Hz$ respectively. The RMSE for each case is recorded and tabulated in Table 3.2. Meanwhile, Fig. 3.18 and Fig. 3.19 portray and compare real input-output relations of ionic polymer metal composites (IPMC) with the estimated input-output relations at $0.05Hz$ and $0.2Hz$ respectively. In this case, RMSE values are recorded as 0.0271 and 0.0795 correspondingly.

Clearly, experimental data show that the hysteresis phenomenon in most smart actuators especially piezoelectric, magnetostrictive and IPMC actuators are rate-dependent.

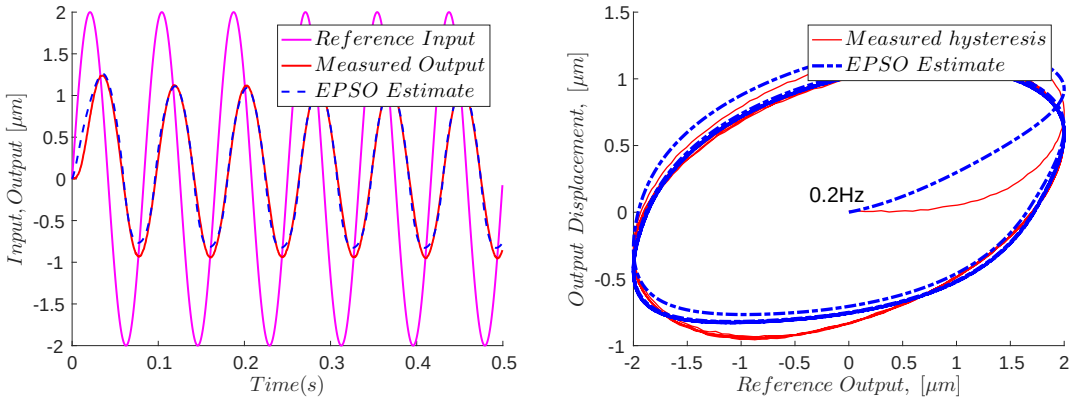

FIGURE 3.19: The graph of input-output relations obtained from experiment (solid) and MBW model (Dashed) using identified parameters for the case of IPMC at $0.2Hz$.

This behaviour is clearly shown in Fig. 3.12 through Fig. 3.19. The shape of hysteresis loops are changing with respect to the input frequency. With the help of EPSO technique, it is verified that the proposed MBW model (3.21) is able to capture the dynamic and hysteretic behavior not only of PEA, but also GMA and IPMC with relatively good accuracies. Thus, it is proven that the proposed MBW model is not unique and would be capable of fitting and matching the input-output relations of other smart actuators.

TABLE 3.2: The RMSE value relating to the estimated (by EPSO) and measured hysteresis curves

Input Frequency	RMSE Value	
	PEA Case (μm)	GMA Case (μm)
1 Hz	0.0248	0.1090
10 Hz	0.0273	0.1056
50 Hz	0.0290	0.1015

Now it is confirmed that the proposed MBW model is capable of describing and characterizing the input-output relations of hysteretic smart actuators. It will be much useful if the proposed model can be directly exploited for synthesizing the control algorithm so that the hysteresis effects can be alleviated or significantly reduced. For this reason, we consider developing two control architectures based on the proposed model (3.21). The details of control developments are discussed in Chapter 4 and Chapter 5.

3.5 Concluding Remarks

In the first stage, the feasibility of differential equations based models towards hysteresis characterization and control fusion are carefully examined. Through this investigation, it is discovered that only BW model is applicable in terms of direct model usage for the control law design. Then, a new model modification to BW model is developed to introduce rate-dependent property. The development is established in the discrete-time domain. Further, the results from validation process show that MBW model is not unique and is capable of describing input-output relations of the smart actuators, especially piezoelectric and magnetostrictive-based actuators with a sound accuracy.

Chapter 4

Discrete Nonlinear Prescribed Performance Control

4.1 Introduction

Inspired by the work of Bechlioulis and Rovithakis, G. A., 2011, the prescribed performance control (PPC) framework is considered in developing the discrete nonlinear PPC (DPPC). The essential point of PPC is to guarantee the convergence of output tracking error to a predefined arbitrarily small region by transforming the system output error into a new coordinate. Then, the transformed error is employed in the control design to modulate the original tracking error with respect to a predefined performance function. The concept of PPC is quite similar to funnel control (FC) (Wang et al., 2016). FC is developed by Ilchmann et al., 2002 for systems with BIBO stable zero-dynamics, known relative degree, and known sign of the high-frequency gain and it is a time-varying (high-gain based) control strategy. The major difference between PPC and FC is the function used to transform output tracking error into a new coordinate.

There is a growing body of literature that related to PPC and FC techniques in addressing the performance issues of the nonlinear systems including Hua and Li, Y., 2015; Kostarigka and Rovithakis, G. A., 2012; Li et al., 2014; Na, 2013 (for PPC); Hackl, 2015; Hopfe et al., 2010; Wang et al., 2016 (for FC). However, these results are established in the continuous-time domain. In this thesis, the PPC is designed directly in discrete-time domain instead of the continuous-time domain. This consideration is taken to avoid numerical approximation which normally degrades the system performance. A new performance function is introduced to properly define the ultimate

allowable steady-state error bound and transient behaviour. In addition, stability analysis of the closed-loop system is also systematically discussed. For evaluation purpose, a commercial PEA product is considered as the test-rig. Experimental results substantiate that the formulated control strategy has the capacity for improving the tracking performance of the PEA without compromising the system's stability.

4.2 Formulation of Control Algorithm

To facilitate the development of the control law, Eqn. (3.21) in Chapter 3 is rewritten as follows

$$y_k = \delta_1 y_{k-1} + \nu_k \mu_k(\nu, y) \tag{4.1}$$

where $\mu_k(\nu, y)$ is defined as

$$\begin{aligned} \mu_k(\nu, y) = \zeta_1 - |y_{k-1}|(\psi_1 sign(\nu_k, y_{k-1}) + \alpha_1) \\ + (\zeta_2 - |y_{k-1}|(\psi_2 sign(\nu_k, y_{k-1}) + \alpha_2))v_{u,k} \end{aligned} \tag{4.2}$$

In view of (4.2), it is obvious that the term $v_{u,k}$ is only available in the open-loop condition. For developing the feedback control strategy, the term $v_{u,k}$ is replaced by the first-order difference of the external desired signal, which is given as

$$r_{u,k} = |r_k - r_{k-1}| \tag{4.3}$$

Thus, Eqn. (4.1)–(4.2) can be rewritten as

$$y_k = \delta_1 y_{k-1} + \nu_k \mu_{r,k}(\nu, y) \tag{4.4}$$

and

$$\begin{aligned} \mu_{r,k}(\nu, y) = \zeta_1 - |y_{k-1}|(\psi_1 sign(\nu_k, y_{k-1}) + \alpha_1) \\ + (\zeta_2 - |y_{k-1}|(\psi_2 sign(\nu_k, y_{k-1}) + \alpha_2))r_{u,k} \end{aligned} \tag{4.5}$$

Assumption 4.1 : Assume that $\zeta_1 \geq \zeta_0 > 0$ and $\zeta_2 \geq 0$, where ζ_0 is a small known constant.

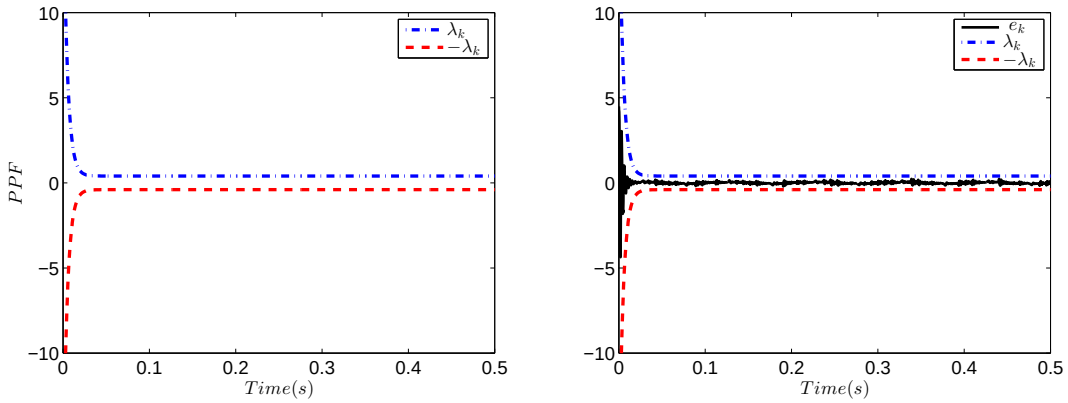

(A) Illustration of performance function λ_k (4.7) with $\omega = 0.01$, $\lambda_0 = 10$, and $\lambda_\infty = 0.4$.

(B) Illustrative example of tracking error e_k evolution specified by (4.8).

FIGURE 4.1: Illustration of performance function λ_k and evolution of tracking error e_k.

The main control objective is to design an appropriate feedback control signal u_k such that the state y_k in (4.4) follows the specified reference trajectory, r_k, i.e., $y_k \to r_k$ within a desired accuracy as $k \to \infty$, where the reference trajectory r_k is a bounded sequence. In this case, we consider synthesizing MBW model (4.4) into the DPPC control framework to solve the motion tracking problem of the piezoelectric based actuators. Define

$$e_k = y_k - r_k \tag{4.6}$$

where y_k and r_k are the measured output and the desired output at time instant k.

Consider the following performance function

$$\lambda_{k+1} = (1 - \omega)\lambda_k + \omega\lambda_\infty \tag{4.7}$$

where λ_k is a positive decreasing function satisfying $\lim_{k\to\infty} \lambda_k = \lambda_\infty$ with $\lambda_0 > \lambda_\infty > 0$, and ω is a constant. Variable λ_∞ defines the ultimate allowable steady-state error bound, while λ_0 denotes the maximum bound of the initial tracking error, i.e., maximum overshoot. Fig. 4.1a depicts the bounds for transient and steady-state specified by relation (4.7).

The control purpose is that the error e_k should evolve strictly within the following region

$$-\underline{h}\lambda_k < e_k < \bar{h}\lambda_k \tag{4.8}$$

This is the so-called prescribed performance control (PPC), where $\underline{h}$ and $\bar{h}$ are strictly positive. Illustrative example of e_k evolution is shown in Fig. 4.1b.

To achieve the prescribed performance of (4.8), the control law is designed as follows

Step 0 : *Choose* λ_0, $\underline{h}$, *and* $\bar{h}$ *such that* $-\underline{h}\lambda_0 < e_0 < \bar{h}\lambda_0$. *Define*

$$\epsilon_0 = 0.5ln(\frac{\lambda_0\underline{h} + e_0}{\lambda_0\bar{h} - e_0}), \tag{4.9}$$

and $\nu_0 = 0$, $u_0 = 0$.

Step k : *Calculate* λ_k *based on (4.7) and define*

$$\epsilon_{k-1} = 0.5ln(\frac{\lambda_{k-1}\underline{h} + e_{k-1}}{\lambda_{k-1}\bar{h} - e_{k-1}}). \tag{4.10}$$

Then choose the signal ν_k *as*

$$\nu_k = \frac{(r_k - \delta_1 y_{k-1})(1 + e^{2\chi\epsilon_{k-1}}) + \lambda_k(\bar{h}e^{2\chi\epsilon_{k-1}} - \underline{h})}{\mu_{r,k}(\nu, y)(1 + e^{2\chi\epsilon_{k-1}})} \tag{4.11}$$

in which $0 < \chi < 1$ *is a design constant. Consequently, the control input* u_k *is determined as*

$$u_k = \nu_k \cdot \Delta t + \delta_2 u_{k-1}. \tag{4.12}$$

Let $k = k + 1$.

Note that ϵ_k is the output error in a new coordinate, i.e., transformed error. The role of ϵ_k is to modulate the tracking error e_k with respect to the required performance bounds imposed by (4.8).

Remark 4.1: The values of parameter α_1 and α_2 in relation (4.5) are restricted such that $\alpha_1 < -|\psi_1|$ and $\alpha_2 < -|\psi_2|$. These restrictions are imposed to guarantee that $\mu_{r,k}(\nu, y)$ is always positive definite satisfying $\mu_{r,k}(\nu, y) > \zeta_0$. Simulation results also show that

this assumption is meaningful as can be observed in Figure 3.8 in Chapter 3.

By referring to ***Remark 4.1***, it can be inferred that ν_k have same sign with the numerator part of (4.11). Define

$$y_{r,k} = \frac{1}{\sigma_k}((r_k - \delta_1 y_{k-1})\sigma_k + \lambda_k(\bar{h}e^{2\chi\epsilon_{k-1}} - \underline{h})) \tag{4.13}$$

where σ_k is defined as $1 + e^{2\chi\epsilon_{k-1}}$.

As a result, ν_k is calculated as follows:

$$\nu_k = \begin{cases} \dfrac{y_{r,k}}{\mu^{+}_{r,k}(\nu, y)}, & \text{if } y_{r,k} \geq 0; \\ \\ \dfrac{y_{r,k}}{\mu^{-}_{r,k}(\nu, y)}, & \text{if } y_{r,k} < 0. \end{cases} \tag{4.14}$$

where $\mu^{+}_{r,k}(\nu, y)$ and $\mu^{-}_{r,k}(\nu, y)$ are given in the following

$$\begin{aligned} \mu^{+}_{r,k}(\nu, y) = \zeta_1 - |y_{k-1}|(\psi_1 sign(y_{k-1}) + \alpha_1) \\ + (\zeta_2 - |y_{k-1}|(\psi_2 sign(y_{k-1}) + \alpha_2))r_{u,k} \end{aligned} \tag{4.15}$$

$$\begin{aligned} \mu^{-}_{r,k}(\nu, y) = \zeta_1 + |y_{k-1}|(\psi_1 sign(y_{k-1}) - \alpha_1) \\ + (\zeta_2 + |y_{k-1}|(\psi_2 sign(y_{k-1}) - \alpha_2))r_{u,k} \end{aligned} \tag{4.16}$$

We have the following theorem to describe the stability of the controlled system.

Theorem 4.1: Consider system (4.4) – (4.5) controlled by (4.12)-(4.16). The prescribed performance of e_k in the sense of (4.8) is achieved for $k \geq 0$ and all the signals in the closed-loop system are bounded. Additionally, the tracking error e_k asymptotically goes to zero as k approaches to infinity, i.e., $\lim_{k\to\infty} e_k = 0$.

Proof:

Substituting the control law (4.11)-(4.12) into the closed-loop system yields

$$e_k = \frac{\lambda_k(\bar{h}e^{2\chi\epsilon_{k-1}} - \underline{h})}{1 + e^{2\chi\epsilon_{k-1}}}. \tag{4.17}$$

Since λ_k is positive, it gives

$$\frac{\lambda_k(-\underline{h}e^{2\chi\epsilon_{k-1}} - \underline{h})}{1+e^{2\chi\epsilon_{k-1}}} < e_k < \frac{\lambda_k(\bar{h}e^{2\chi\epsilon_{k-1}} + \bar{h})}{1+e^{2\chi\epsilon_{k-1}}} \tag{4.18}$$

i.e.

$$-\underline{h}\lambda_k < e_k < \bar{h}\lambda_k \tag{4.19}$$

which means that the prescribed performance of e_k in the sense of (4.8) is satisfied. From (4.19), it can be seen that ϵ_k is well defined. At the $(k+1)th$ step, ϵ_k is calculated as

$$\epsilon_k = 0.5ln(\frac{\lambda_k\underline{h} + e_k}{\lambda_k\bar{h} - e_k}). \tag{4.20}$$

Substituting (4.17) into (4.20) gives

$$\begin{aligned}
\epsilon_k &= 0.5ln\left(\frac{\lambda_k\underline{h} + \frac{\lambda_k(\bar{h}e^{2\chi\epsilon_{k-1}} - \underline{h})}{1+e^{2\chi\epsilon_{k-1}}}}{\lambda_k\bar{h} - \frac{\lambda_k(\bar{h}e^{2\chi\epsilon_{k-1}} - \underline{h})}{1+e^{2\chi\epsilon_{k-1}}}}\right) \\
&= 0.5ln\left(\frac{\lambda_k(\underline{h}\sigma_k + \bar{h}e^{2\chi\epsilon_{k-1}} - \underline{h})}{\lambda_k(\bar{h}\sigma_k - \bar{h}e^{2\chi\epsilon_{k-1}} - \underline{h})}\right) \\
&= 0.5ln\left(\frac{(\bar{h}+\underline{h})e^{2\chi\epsilon_{k-1}}}{\bar{h}+\underline{h}}\right) \\
&= \chi\epsilon_{k-1}
\end{aligned} \tag{4.21}$$

which means that $|\epsilon_k|$ is decreasing and bounded satisfying $\lim_{k\to\infty}\epsilon_k = 0$. By (4.17), it is obvious that the tracking error e_k can be asymptotically brought to zero as k goes to infinity, i.e., $\lim_{k\to\infty} e_k = 0$ if the upper bound $\bar{h}$ and the lower bound $\underline{h}$ are chosen such that $\underline{h} = \bar{h}$. In addition, it is also established that the control signal ν_k is bounded by observing relation in (4.11) where $\mu_{r,k}(\nu, y) > \zeta_0$ is used. Finally, from (4.12), since $0 < \delta_2 < 1$, we can conclude that the control input u_k is bounded.

4.3 Experimental Verification

This section is devoted to implementation of the formulated control framework in a real case application. Subsection 4.3.1 discusses the experimental environment and the

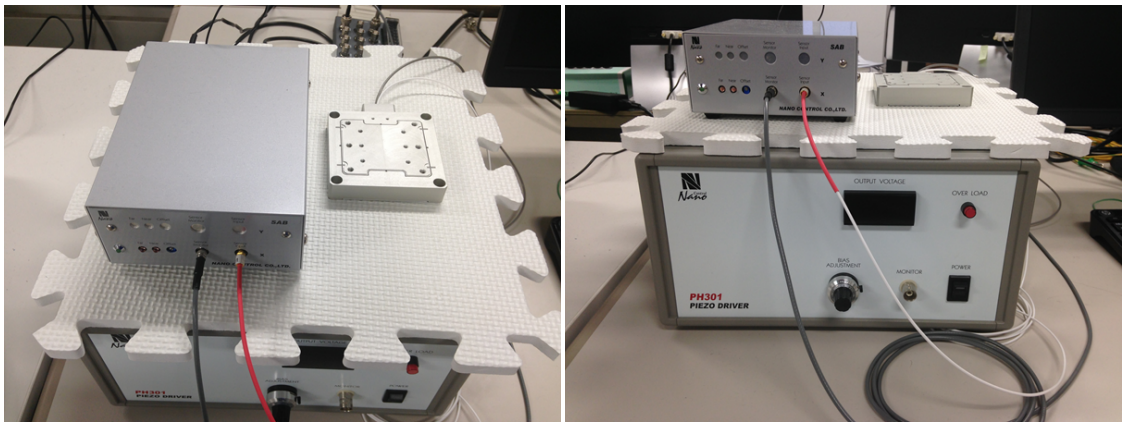

FIGURE 4.2: The physical diagram of the experimental platform.

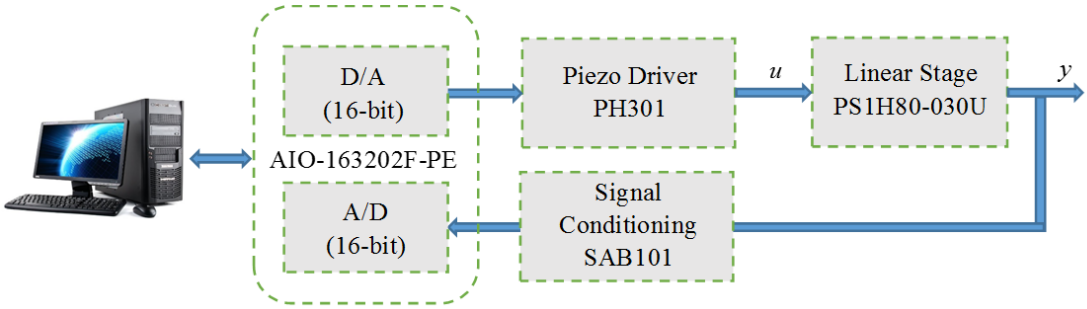

FIGURE 4.3: The setup diagram of the experimental platform.

dedicated setup. Then, Subsection 4.3.2 presents the experimental results along with the discussions.

4.3.1 Experimental Environment

Fig. 4.2 and Fig. 4.3 depict the experimental platform used in this section. The PEA stage PS1H80-030U (Nano Control Co. Ltd., Japan) consists of a moving table (one directional movement), a piezoelectric actuator and a built-in displacement sensor. The travel range of the PEA stage is $30\mu m$. While the resolution of the built-in sensor is $2nm$. The sensor's output is connected to the SAB101 signal conditioning device, which maps the measured displacement into voltage signal. The PEA stage is powered by PH301 power unit, which has a range of $0V$ to $150V$ with a bandwidth of $6kHz$. An analog interface board (AIO-163202F-PE) is used for data collection throughout the experimentation. The interface board is equipped with 32 analog inputs (AIs) and 2 analog outputs (AOs) with 16bits resolution and $500kHz$ sampling rate. The control algorithm is implemented on a personal computer (PC) by C language. The sampling frequency is set as $2kHz$.

4.3.2 Experimental Results and Discussion

TABLE 4.1: The optimal parameter values of MBW model (estimated by EPSO)

Parameter	Value
ζ_1	0.4029
ζ_2	6.7438e-06
ψ_1	0.0345
ψ_2	0.0149
α_1	-0.0394
α_2	-0.0245
δ_1	0.9620
δ_2	0.9511

TABLE 4.2: The chosen controller gains of DPPC

Controller Gain	Value
λ_0	20
λ_∞	0.4
ω	0.01
χ	0.1
$\underline{h} = \bar{h}$	1.0

A series of experimental studies are conducted to evaluate the performance of the proposed control design. In order to quantify the tracking results, the RMSE and the Maximum Absolute Error (MAE) are used. Throughout the experiment study, the optimal parameters of MBW model which identified by EPSO technique are used. These parameters are tabulated in Table 4.1. Meanwhile the controller gains of the DPPC are chosen as in Table 4.2.

Initially, experiments are conducted without taking into account any control scheme, i.e., open loop condition. Fig. 4.4 through Fig. 4.6 show the input-output plot for the case of the typical step input, and sinusoidal inputs with $1Hz$ and $20Hz$ frequencies. In both cases, it can be seen that the system is affected by a strong hysteresis nonlinearity. Without any control effort, large errors are noticed, the performance of the system is very poor that merely 50% of the output tracking is achieved.

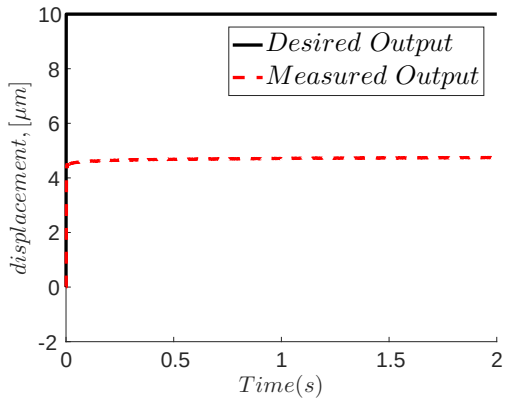

FIGURE 4.4: Input-output plot of the PEA stage without any control efforts (Open-loop condition of a step input case).

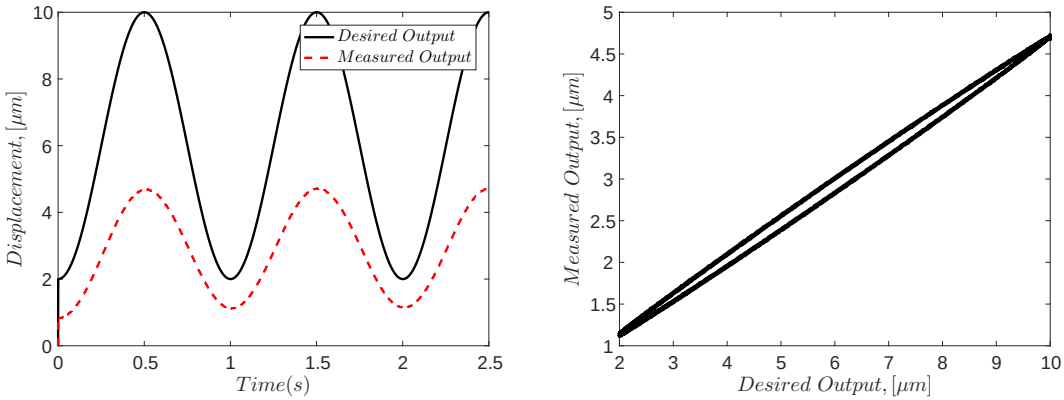

FIGURE 4.5: Input-output plot of the PEA stage without any control efforts (Open-loop condition of $1Hz$ sinusoidal input).

Now, the formulated control scheme is employed to see how well it can mitigate the hysteresis effects. Several experimental cases are considered and designed to study the tracking performance and the closed-loop behaviour. Firstly, experiments with Step and Ramp trajectory references are conducted. As illustrated in Fig. 4.7 and Fig. 4.8, superior performance are achieved for all cases. Furthermore, the settling time is very fast that the steady-state is reached within less than $80ms$ for the case of Step input. While for the combination of Step and Ramp (Step-Ramp) input, there is no transient response is observed. In both cases, the tracking errors vary from -0.01 to $0.01\mu m$ in the steady-state.

Next, we consider tracking experiments for Sinusoidal references. In this case, several numbers of excitation frequencies are studied, i.e., from $1Hz - 30Hz$. Fig. 4.9 and Fig. 4.10 depict the motion tracking performance for the case of $5Hz$ and $20Hz$ respectively, from these figures we can observe that good agreements are achieved between

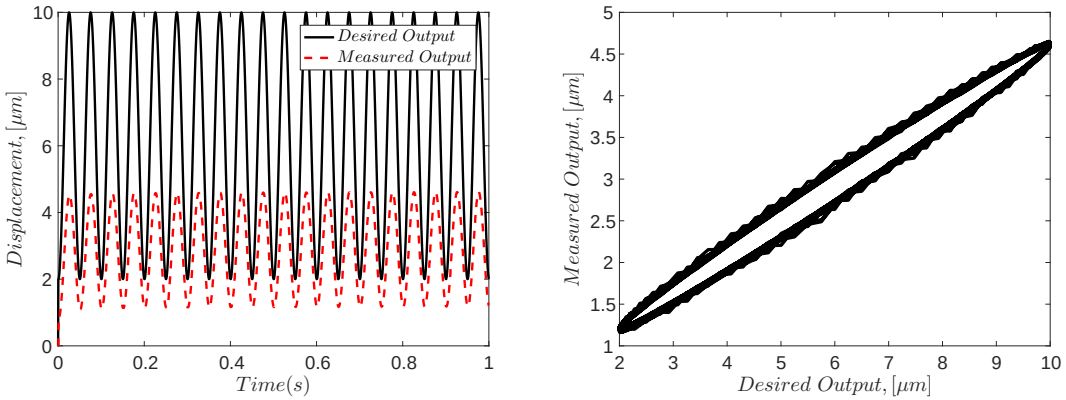

FIGURE 4.6: Input-output plot of the PEA stage without any control efforts (Open-loop condition of $20Hz$ sinusoidal input).

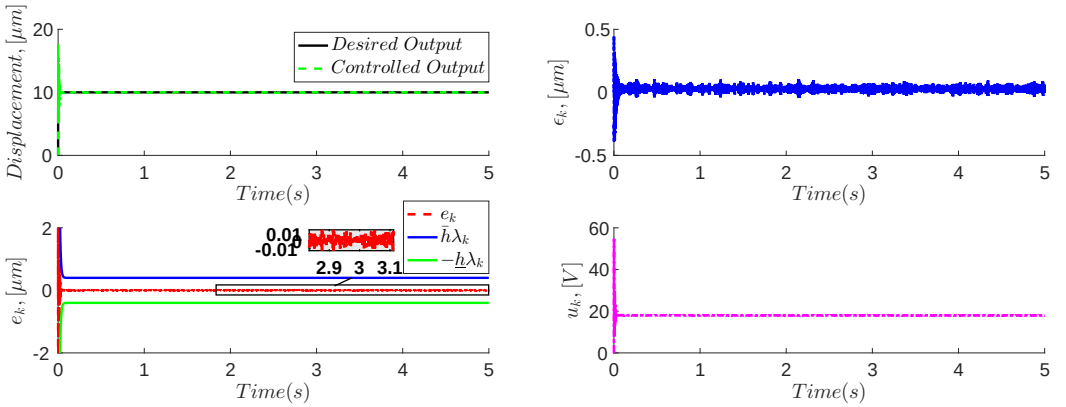

(A) Comparison of Desired output and Controlled output.

(B) The plots of transformed error ϵ_k and control effort u_k.

FIGURE 4.7: The plots of performance tracking for the Step input case.

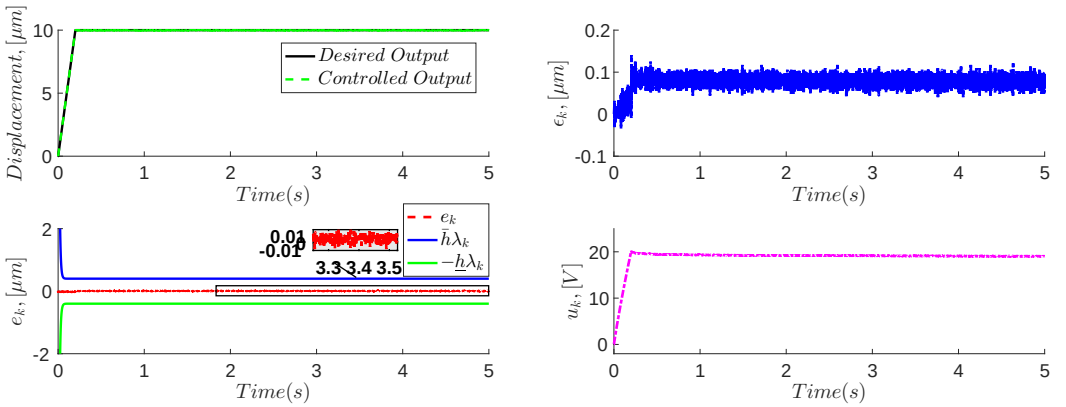

(A) Comparison of Desired output and Controlled output.

(B) The plots of transformed error ϵ_k and control effort u_k.

FIGURE 4.8: The plots of performance tracking for the case of Step-Ramp input.

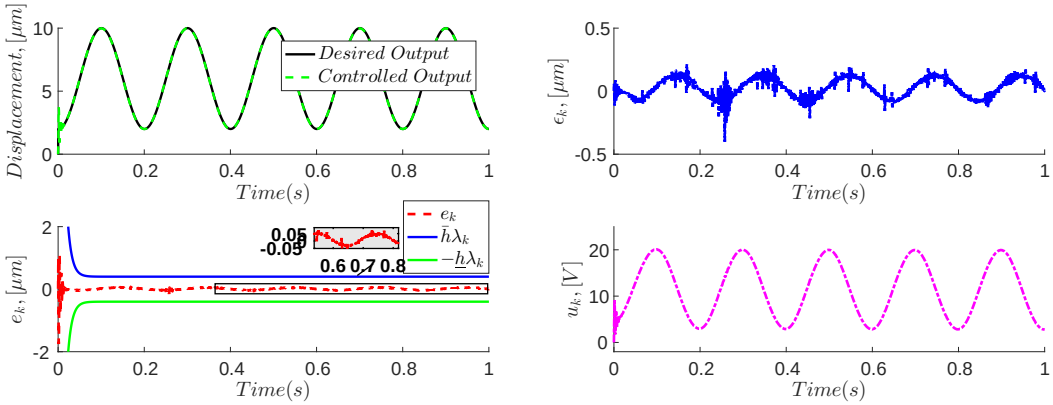

(A) Comparison of Desired output and Controlled output.

(B) The plots of transformed error ϵ_k and control effort u_k.

FIGURE 4.9: The plots of performance tracking for the sinusoidal input case ($5Hz$).

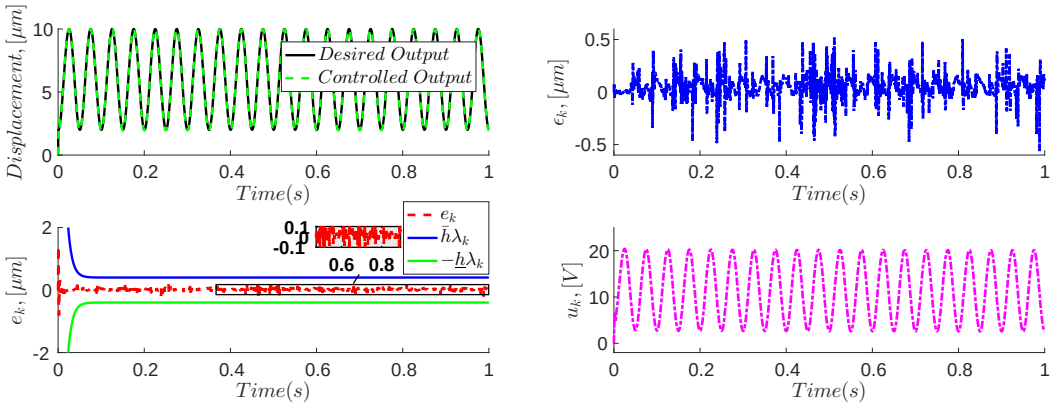

(A) Comparison of Desired output and Controlled output.

(B) The plots of transformed error ϵ_k and control effort u_k.

FIGURE 4.10: The plots of performance tracking for the sinusoidal input case ($20Hz$).

the desired and controlled outputs. In addition, good settling times are attained (within $50ms$) in comparison to the step trajectory tracking. Meanwhile, Fig. 4.11 provides the input-output plots for the closed-loop condition of Sinusoidal inputs with $5Hz$ and $20Hz$ frequencies, i.e., when the DPPC scheme is employed. It can be witnessed that a significant performance improvement is achieved with the implementation of the proposed control algorithm.

Meanwhile, Table 4.3 summarizes the tracking performance in terms of RMSE and MAE for the input references relating to Step, Ramp, and Sinusoidal cases. As can be seen in Table 4.3, the performance index for the step and ramp cases are much better compared to the sinusoidal case with practically small RMSE and MAE. This situation

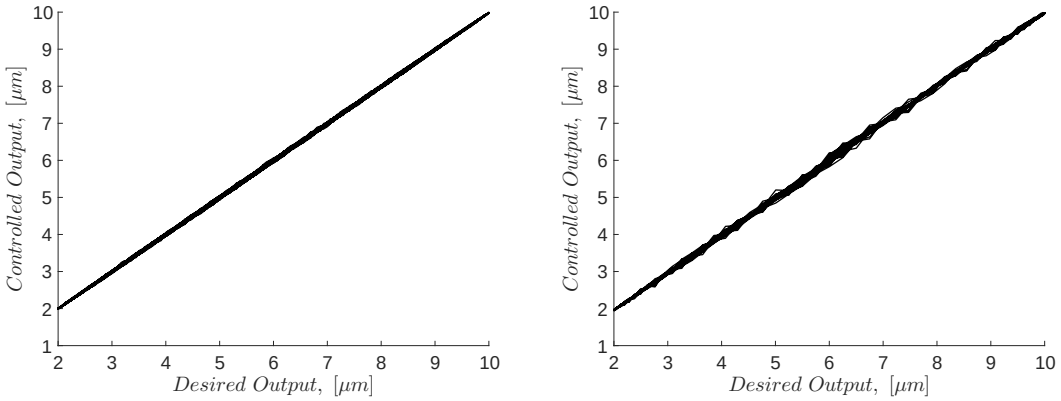

(A) $5Hz$ sinusoidal input. (B) $20Hz$ sinusoidal input.

FIGURE 4.11: The plots of input-output relations, i.e. closed-loop condition.

is common because less control effort is needed to regulate Step and Ramp input trajectories. Furthermore, these inputs are not as complicated as the Sinusoidal input.

To further confirm the effectiveness of MBW model and the proposed control scheme, we consider more complex inputs that involving multiple frequencies, i.e., to imitate the situation of rate-dependent behaviour. Three different input trajectories are designed. The first one is a wave input with multiple frequencies (a combination of 5Hz, 15Hz, and 40Hz) (**C1**). The second case is essentially an input with a varied frequency (**C2**). While the third one is an input with two sinusoidal functions that combined together (**C3**). Results corresponding to these inputs are shown in Fig. 4.12 to Fig. 4.14. As can be observed through these figures, the tracking performance for each case is relatively good. It is recorded that the range of tracking errors in the steady-state are within ± 0.08 μm for **C1**, ± 0.1 μm for **C2**, and ± 0.12 μm for **C3**. While Table 4.4 tabulates the performance index for each case (RMSE and MAE) for **C1**, **C2**, and **C3** respectively.

Additionally, it can be seen that the control efforts are stable throughout the experiments. This stability is achieved due to steady evolution of the transformed error ϵ_k. As a results, the progression of error in each experimental study is restricted in the specified region Eqn. (4.8). In other terms, the proposed DPPC can guarantee the prescribed transient and steady-state boundaries.

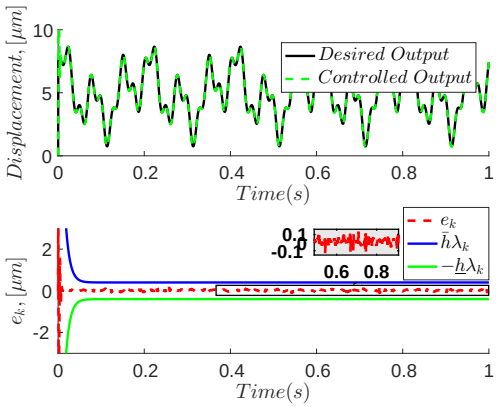

(A) Comparison of Desired output and Controlled output.

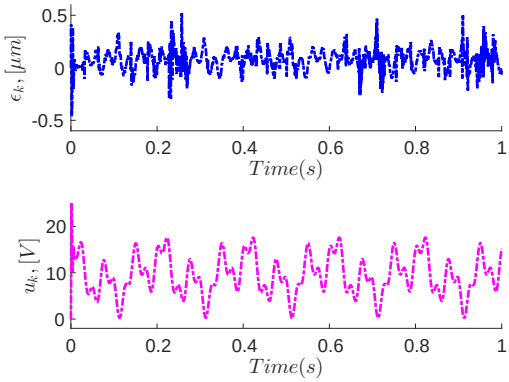

(B) The plots of transformed error ϵ_k and control effort u_k.

FIGURE 4.12: The plots of performance tracking for complex input case (**C1**).

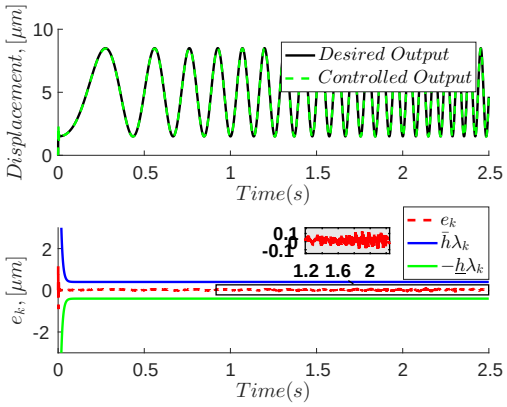

(A) Comparison of Desired output and Controlled output.

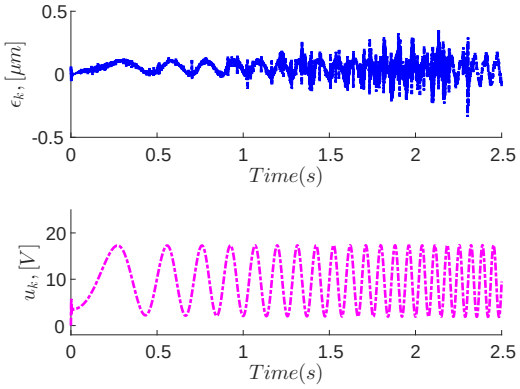

(B) The plots of transformed error ϵ_k and control effort u_k.

FIGURE 4.13: The plots of performance tracking for complex input case (**C2**).

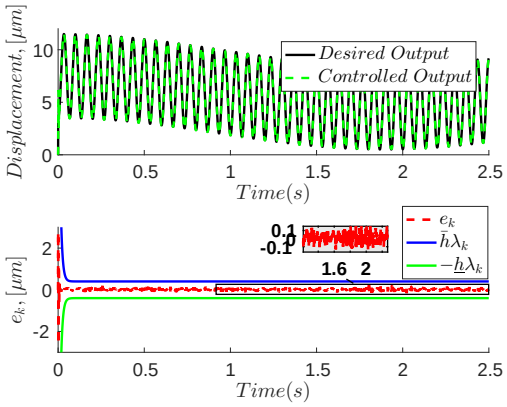

(A) Comparison of Desired output and Controlled output.

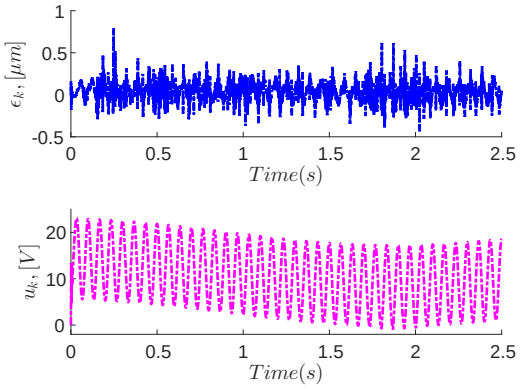

(B) The plots of transformed error ϵ_k and control effort u_k.

FIGURE 4.14: The plots of performance tracking for complex input case (**C3**).

TABLE 4.3: The summary of the tracking performance for the input related to step, ramp and sinusoidal functions

	Performance Index	
Type of Input	RMSE (μm)	MAE (μm)
Step	0.00518	0.02075
Ramp	0.00673	0.02626
Step + Ramp	0.00773	0.02991
Sinusoidal (1 Hz)	0.01505	0.04044
Sinusoidal (5 Hz)	0.03246	0.09368
Sinusoidal (10 Hz)	0.03620	0.12454
Sinusoidal (20 Hz)	0.04293	0.21616
Sinusoidal (30 Hz)	0.06941	0.39607

TABLE 4.4: The summary of the tracking performance for the mixed frequency trajectories

	Performance Index	
Type of Input	RMSE (μm)	MAE (μm)
C 1 as in Fig. 4.12	0.03341	0.1343
C 2 as in Fig. 4.13	0.04691	0.2197
C 3 as in Fig. 4.14	0.03889	0.1906

4.4 Concluding Remarks

In this chapter, a new nonlinear discrete control design based on the modified version of BW model is presented. The control architecture is synthesized by fusing the MBW model into the discrete prescribed performance control strategy. Additionally, stability analysis of the closed-loop system under the formulated control algorithm is presented. Finally, a real case controller implementation is given to show the efficiency of the proposed control strategy.

Chapter 5

Discrete Model Reference Adaptive Control

5.1 Introduction

In this chapter, we exploit the MBW model (3.21) in designing a discrete model reference adaptive control strategy (DMRAC) in order to suppress hysteresis nonlinearity. This is an alternative control synthesis based on MBW model designed to improve motion tracking of smart actuators. The main merit of this control framework is that only the parameters in the controller algorithm need to be adaptively estimated, and the real values of the positioner's parameters need to be neither identified nor measured.

First, the proposed MBW model (3.21) in Chapter 3 is rearranged as follows

$$y_k = \delta_1 y_{k-1} + \nu_k \mu_k(\nu, y) \tag{5.1}$$

where $\mu_k(\nu, y)$ is defined as

$$\begin{aligned} \mu_k(\nu, y) = \zeta_1 - |y_{k-1}|(\psi_1 sign(\nu_k, y_{k-1}) + \alpha_1) \\ + (\zeta_2 - |y_{k-1}|(\psi_2 sign(\nu_k, y_{k-1}) + \alpha_2))v_{u,k} \end{aligned} \tag{5.2}$$

5.2 Controller Design

In general, the proposed control block diagram is illustrated in Fig. 5.1. The input-output relations of the smart actuators that possessing the hysteretic phenomenon are assumed to be described by Eqn. (5.1) with unknown parameters of ζ_1, ζ_2, ψ_1, ψ_2, α_1 and α_2. The control objective is to find a sequence of control signal u_k that forces the

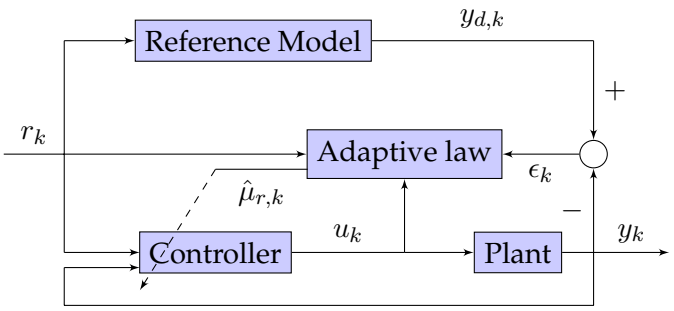

FIGURE 5.1: The block diagram of the proposed control framework.

state y_k in (5.1) to follow the desired output $y_{d,k}$ of the reference model given in (5.3) within a desired accuracy as $k \to \infty$.

$$y_{d,k} = r_k + a_m y_{d,k-1} \tag{5.3}$$

where $|a_m| < 1$ and r_k is a bounded reference input.

5.2.1 Formulation of Adaptive Algorithm

In view of (5.1)–(5.2), it is obvious that the term $v_{u,k}$ is only available in the open-loop condition. For the case of the closed-loop control strategy, the term $v_{u,k}$ is replaced by the first-order difference of the external desired signal, which is defined as

$$r_{u,k} = |r_k - r_{k-1}| \tag{5.4}$$

Thus, Eqn. (5.1)–(5.2) can rewritten as

$$y_k = (\delta_1 - a_m)y_{k-1} + a_m y_{k-1} + \nu_k \mu_{r,k}(\nu, y) \tag{5.5}$$

and

$$\begin{aligned} \mu_{r,k}(\nu, y) = \zeta_1 - |y_{k-1}|(\psi_1 sign(\nu_k, y_{k-1}) + \alpha_1) \\ + (\zeta_2 - |y_{k-1}|(\psi_2 sign(\nu_k, y_{k-1}) + \alpha_2))r_{u,k} \end{aligned} \tag{5.6}$$

This is done to preserve the rate-dependent property of MBW model in the closed-loop condition. In addition, for relations (5.5)–(5.6), same ***Assumption 4.1*** (introduced in Chapter 4) is imposed.

Now define the tracking error

$$e_k = y_k - y_{d,k} \tag{5.7}$$

From (5.3) and (5.5), it yields

$$e_k = (\delta_1 - a_m)y_{k-1} - r_k + a_m e_{k-1} + \nu_k \mu_{r,k}(\nu, y) \tag{5.8}$$

Indeed the unknown parameters ζ_1, ζ_2, ψ_1, ψ_2, α_1 and α_2 could be identified via the EPSO technique, but it is much desirable that if all the parameters can be adaptively estimated. Thus, an online adaptive method is formulated for estimating the above mentioned unknown parameters.

Let $\hat{\zeta}_{1,k}$, $\hat{\zeta}_{2,k}$, $\hat{\psi}_{1,k}$, $\hat{\psi}_{2,k}$, $\hat{\alpha}_{1,k}$ and $\hat{\alpha}_{2,k}$ be the estimates of ζ_1, ζ_2, ψ_1, ψ_2, α_1 and α_2 at the kth step, respectively.

Next, define the estimation error as

$$\epsilon_k = \delta_1 y_{k-1} + \nu_k \hat{\mu}_{r,k}(\nu, y) - y_k \tag{5.9}$$

with

$$\begin{aligned} \hat{\mu}_{r,k}(\nu, y) = \hat{\zeta}_1 - |y_{k-1}|(\hat{\psi}_1 sign(\nu_k, y_{k-1}) + \hat{\alpha}_1) \\ + (\hat{\zeta}_2 - |y_{k-1}|(\hat{\psi}_2 sign(\nu_k, y_{k-1}) + \hat{\alpha}_2))r_{u,k} \end{aligned} \tag{5.10}$$

Finally, for simplicity, introduce

$$N_k = \sqrt{1 + (\nu_k^2 + 2(\nu_k y_{k-1})^2)(1 + r_{u,k}^2)} \tag{5.11}$$

The estimates of $\hat{\zeta}_{1,k}$, $\hat{\zeta}_{2,k}$, $\hat{\psi}_{1,k}$, $\hat{\psi}_{2,k}$, $\hat{\alpha}_{1,k}$ and $\hat{\alpha}_{2,k}$ are updated by the following constrained adaptation laws

$$\hat{\zeta}'_{1,k} = |\hat{\zeta}'_{1,k-1} - \kappa \frac{\epsilon_{k-1}\nu_{k-1}}{N_{k-1}^2}| \tag{5.12a}$$

$$\hat{\zeta}_{1,k} = \begin{cases} \hat{\zeta}'_{1,k}, & \textit{if } \hat{\zeta}'_{1,k} > \zeta_0 \\ \zeta_0, & \textit{otherwise} \end{cases} \tag{5.12b}$$

$$\hat{\zeta}'_{2,k} = |\hat{\zeta}'_{2,k-1} - \kappa \frac{\epsilon_{k-1} r_{u,k-1}\nu_{k-1}}{N_{k-1}^2}| \tag{5.13a}$$

$$\hat{\zeta}_{2,k} = \begin{cases} \hat{\zeta}'_{2,k}, & \textit{if } \hat{\zeta}'_{2,k} \geq 0 \\ 0, & \textit{otherwise} \end{cases} \tag{5.13b}$$

$$\hat{\psi}_{1,k} = \hat{\psi}_{1,k-1} + \kappa \frac{\epsilon_{k-1}|\nu_{k-1}|y_{k-2}}{N_{k-1}^2} \tag{5.14}$$

$$\hat{\psi}_{2,k} = \hat{\psi}_{2,k-1} + \kappa \frac{\epsilon_{k-1} r_{u,k-1}|\nu_{k-1}|y_{k-2}}{N_{k-1}^2} \tag{5.15}$$

$$\hat{\alpha}'_{1,k} = \hat{\alpha}'_{1,k-1} + \kappa \frac{\epsilon_{k-1}\nu_{k-1}|y_{k-2}|}{N_{k-1}^2} \tag{5.16a}$$

$$\hat{\alpha}_{1,k} = \begin{cases} \hat{\alpha}'_{1,k}, & \textit{if } \hat{\alpha}'_{1,k} < -|\hat{\psi}_{1,k}| - \varrho \\ -|\hat{\psi}_{1,k}| - \varrho, & \textit{otherwise} \end{cases} \tag{5.16b}$$

$$\hat{\alpha}'_{2,k} = \hat{\alpha}'_{2,k-1} + \kappa \frac{\epsilon_{k-1} r_{u,k-1} \nu_{k-1} |y_{k-2}|}{N_{k-1}^2} \tag{5.17a}$$

$$\hat{\alpha}_{2,k} = \begin{cases} \hat{\alpha}'_{2,k}, & \text{if } \hat{\alpha}'_{2,k} < -|\hat{\psi}_{2,k}| \\ -|\hat{\psi}_{2,k}|, & \text{otherwise} \end{cases} \tag{5.17b}$$

Remark 5.1: The parameter adaptation gain κ $(0 < \kappa < 2)$ in (5.12)-(5.17) is introduced to adjust the adaptation speed, while ϱ in (5.16) is a very small positive constant.

Lemma 5.1: For the adaptation algorithms described in (5.12)-(5.17), we have the following properties:

(P1) $\hat{\zeta}_{1,k}$, $\hat{\zeta}_{2,k}$, $\hat{\psi}_{1,k}$, $\hat{\psi}_{2,k}$, $\hat{\alpha}_{1,k}$ and $\hat{\alpha}_{2,k}$ are bounded for all $k > 0$.

(P2) $\sum_{k=1}^{\infty} (\frac{\epsilon_k^2}{N_k^2}) < \infty$.

(P3) $\lim_{k \to \infty} (\frac{|\epsilon_k|}{N_k}) = 0$.

(P4) For any positive integer p and for $i = 1, 2$, it yields

$$\sum_{k=p}^{\infty} \|\hat{\zeta}_{i,k} - \hat{\zeta}_{i,k-p}\|_2^2 < \infty$$

$$\sum_{k=p}^{\infty} \|\hat{\psi}_{i,k} - \hat{\psi}_{i,k-p}\|_2^2 < \infty$$

$$\sum_{k=p}^{\infty} \|\hat{\alpha}_{i,k} - \hat{\alpha}_{i,k-p}\|_2^2 < \infty$$

Proof:

First, define

$$\tilde{\zeta}_{i,k} = \hat{\zeta}_{i,k} - \zeta_i \tag{5.18a}$$

$$\tilde{\psi}_{i,k} = \hat{\psi}_{i,k} - \psi_i \tag{5.18b}$$

$$\tilde{\alpha}_{i,k} = \hat{\alpha}_{i,k} - \alpha_i \tag{5.18c}$$

for $i = 1, 2$.

Next, introduce the Lyapunov function:

$$L_k = \tilde{\zeta}_{1,k}^2 + \tilde{\zeta}_{2,k}^2 + \tilde{\psi}_{1,k}^2 + \tilde{\psi}_{2,k}^2 + \tilde{\alpha}_{1,k}^2 + \tilde{\alpha}_{2,k}^2 \tag{5.19}$$

Taking the difference of L_k along the trajectories of (5.12)-(5.17) gives

$$\begin{aligned}
L_k - L_{k-1} &= \tilde{\zeta}_{1,k}^2 - \tilde{\zeta}_{1,k-1}^2 + \tilde{\zeta}_{2,k}^2 - \tilde{\zeta}_{2,k-1}^2 + \tilde{\psi}_{1,k}^2 - \tilde{\psi}_{1,k-1}^2 \\
&\quad + \tilde{\psi}_{2,k}^2 - \tilde{\psi}_{2,k-1}^2 + \tilde{\alpha}_{1,k}^2 - \tilde{\alpha}_{1,k-1}^2 + \tilde{\alpha}_{2,k}^2 - \tilde{\alpha}_{2,k-1}^2 \\
&\leq 2\kappa \frac{\epsilon_{k-1}\tilde{\alpha}_{1,k-1}\nu_{k-1}}{N_{k-1}^2} - 2\kappa \frac{\epsilon_{k-1}\tilde{\alpha}_{2,k-1} r_{u,k-1}\nu_{k-1}}{N_{k-1}^2} \\
&\quad + 2\kappa \frac{\epsilon_{k-1}\tilde{\psi}_{1,k-1}|\nu_{k-1}|y_{k-2}}{N_{k-1}^2} + 2\kappa \frac{\epsilon_{k-1}\tilde{\psi}_{2,k-1} r_{u,k-1}|\nu_{k-1}|y_{k-2}}{N_{k-1}^2} \\
&\quad + 2\kappa \frac{\epsilon_{k-1}\tilde{\alpha}_{1,k-1}\nu_{k-1}|y_{k-2}|}{N_{k-1}^2} + 2\kappa \frac{\epsilon_{k-1}\tilde{\alpha}_{2,k-1} r_{u,k-1}\nu_{k-1}|y_{k-2}|}{N_{k-1}^2} \\
&\quad + \kappa^2 \frac{\epsilon_{k-1}^2(1 + r_{u,k-1}^2)\nu_{k-1}^2}{N_{k-1}^2} + \kappa^2 \frac{\epsilon_{k-1}^2 2(1 + r_{u,k-1}^2)(\nu_{k-1}y_{k-1})^2}{N_{k-1}^2} \\
&\leq -2\kappa \frac{\epsilon_{k-1}^2}{N_{k-1}^2} + \kappa^2 \frac{\epsilon_{k-1}^2 N_{k-1}^2}{N_{k-1}^4} \\
&= -\kappa(2 - \kappa)\frac{\epsilon_{k-1}^2}{N_{k-1}^2}
\end{aligned} \tag{5.20}$$

Because L_k is a positive function, the properties of ***Lemma 5.1*** can be further proved by Lemma 3.3.2 in Goodwin and Sin, K. S., 2009.

5.2.2 Adaptive Control Design

This subsection presents the formulation of the control signal u_k. Based on relation (5.8), and the developed adaptive algorithm (5.12)-(5.17) in the previous subsection, a

robust adaptive control law can be realized and is derived as follows:

$$\nu_k \hat{\mu}_{r,k}(\nu, y) + (\delta_1 - a_m) y_{k-1} = r_k \tag{5.21}$$

It follows that

$$\nu_k = \frac{r_k - (\delta_1 - a_m) y_{k-1}}{\hat{\mu}_{r,k}(\nu, y)} \tag{5.22}$$

Consequently, the control input u_k is obtained as

$$u_k = \delta_2 u_{k-1} + \nu_k \cdot \Delta t \tag{5.23}$$

Remark 5.2: By scrutinizing the formulated constraints penalized on $\hat{\alpha}_{1,k}$ and $\hat{\alpha}_{2,k}$ in (5.16) and (5.17) respectively, it can be induced that $\hat{\mu}_k(\nu, y)$ in (5.22) will always be positive definite satisfying $\hat{\mu}_k(\nu, y) \geq \varrho |y_{k-1}| + \xi_0 > 0$.

Thus, it can be established that ν_k must have same sign with the numerator part of (5.22). Define

$$y_{r,k} = r_k - (\delta_1 - a_m) y_{k-1} \tag{5.24}$$

As a result, ν_k is calculated as follows:

$$\nu_k = \begin{cases} \dfrac{y_{r,k}}{\hat{\mu}^{+}_{r,k}(\nu, y)}, & \text{if } y_{r,k} \geq 0 \\ \\ \dfrac{y_{r,k}}{\hat{\mu}^{-}_{r,k}(\nu, y)}, & \text{if } y_{r,k} < 0 \end{cases} \tag{5.25}$$

where $\hat{\mu}^{+}_{r,k}(\nu, y)$ and $\hat{\mu}^{-}_{r,k}(\nu, y)$ are given by the following relations

$$\begin{aligned} \hat{\mu}^{+}_{r,k}(\nu, y) = \hat{\zeta}_1 - |y_{k-1}|(\hat{\psi}_1 sign(y_{k-1}) + \hat{\alpha}_1) \\ + (\hat{\zeta}_2 - |y_{k-1}|(\hat{\psi}_2 sign(y_{k-1}) + \hat{\alpha}_2)) r_{u,k} \end{aligned} \tag{5.26}$$

$$\begin{aligned} \hat{\mu}^{-}_{r,k}(\nu, y) = \hat{\zeta}_1 + |y_{k-1}|(\hat{\psi}_1 sign(y_{k-1}) - \hat{\alpha}_1) \\ + (\hat{\zeta}_2 + |y_{k-1}|(\hat{\psi}_2 sign(y_{k-1}) - \hat{\alpha}_2)) r_{u,k} \end{aligned} \tag{5.27}$$

We have the following theorem to describe the stability of the controlled system.

Theorem 5.1: For the system (5.5)-(5.6) controlled by (5.23)-(5.27), all the signals in the closed-loop system are bounded and the output tracking error e_k approaches to zero asymptotically as k approaches to infinity.

Proof:

Eqn. (5.21) can be expressed as

$$r_k - (\delta_1 - a_m)y_{k-1} = \nu_k \hat{\mu}_{r,k}(\nu, y) \tag{5.28}$$

Substituting (5.28) into (5.9) yields

$$\epsilon_k = r_k + a_m y_{k-1} - y_k \tag{5.29}$$

From the definition of N_k in (5.11), it yields

$$N_k \leq 1 + (1 + \sqrt{2}|y_{k-1}|)(1 + r_{u,k})|\nu_k| \tag{5.30}$$

Since the reference input r_k is bounded, denote R as the boundary of r_k, it gives

$$r_{u,k} \leq 2R \tag{5.31}$$

By substituting (5.31) into (5.30), we obtain

$$N_k \leq 1 + (1 + \sqrt{2}|y_{k-1}|)(1 + 2R)|\nu_k| \tag{5.32}$$

In virtue of (5.22) and ***Remark 5.2***, there exist positive constants A_1 and A_2 such that

$$|\nu_k| \leq \frac{A_1 + A_2|y_{k-1}|}{\zeta_0 + \varrho|y_{k-1}|} \tag{5.33}$$

which implies that

$$|\nu_k| \leq B \tag{5.34}$$

From (5.29), (5.32) and (5.34), we obtain

$$\begin{aligned}
|y_k| &= |-\epsilon_k + a_m y_{k-1} + r_k| \\
&\leq \frac{|\epsilon_k|}{N_k} N_k + a_m|y_{k-1}| + |r_k| \\
&\leq \frac{|\epsilon_k|}{N_k}(1 + (1+\sqrt{2}|y_{k-1}|)(1+2R)|\nu_k|) + a_m|y_{k-1}| + |r_k| \\
&\leq \frac{|\epsilon_k|}{N_k}(1 + (1+\sqrt{2}|y_{k-1}|)(1+2R)B) + a_m|y_{k-1}| + |r_k| \\
&= \frac{|\epsilon_k|}{N_k}(1 + (1+2R)B) + \frac{|\epsilon_k|}{N_k}\sqrt{2}B(1+2R)|y_{k-1}| + a_m|y_{k-1}| + |r_k|
\end{aligned} \tag{5.35}$$

Since $\lim_{k\to\infty} \frac{|\epsilon_k|}{N_k} = 0$ and $|a_m| < 1$, there exist an instant K and positive constants C_1, and C_2 such that

$$|y_k| \leq C_1 + C_2|y_{k-1}| \tag{5.36}$$

for all $k > K$, where $C_2 < 1$.

At step i (for $K+1 \leq i \leq k$), multiplying both sides of (5.36) with C_2^{k-i} gives

$$C_2^{k-i}|y_i| \leq C_1 C_2^{k-i} + C_2^{k-i+1}|y_{i-1}| \tag{5.37}$$

Summing both sides of (5.37) from $i = K+1$ to $i = k$ gives

$$|y_k| \leq C_1\Big(C_1C_2 + C_1C_2^2 + \cdots + C_1C_2^{k-K-1}\Big) + C_2^{k-K}|y_K| \tag{5.38}$$

Thus, the upper bound of controlled output y_k can be expressed as follows

$$|y_k| \leq C_1\Big(\frac{1-C_2^{k-K}}{1-C_2}\Big) + C_2^{k-K}|y_K| \tag{5.39}$$

By now, it is obvious from Eqn. (5.34), that the input variable ν_k is bounded. In addition, from Eqn. (5.23), since $0 < \delta_2 < 1$, it can be induced that the input u_k is also bounded. Then, by Eqn. (5.32), it can be seen that N_k is bounded. Thus, based on property (P3) in ***Lemma 5.1***, it can be inferred that $\lim_{k\to\infty} \epsilon_k = 0$.

From (5.3) and (5.21), it follows that

$$\begin{aligned}
\epsilon_k &= r_k + a_m y_{k-1} - y_k \\
&= -e_k + a_m e_{k-1}
\end{aligned} \tag{5.40}$$

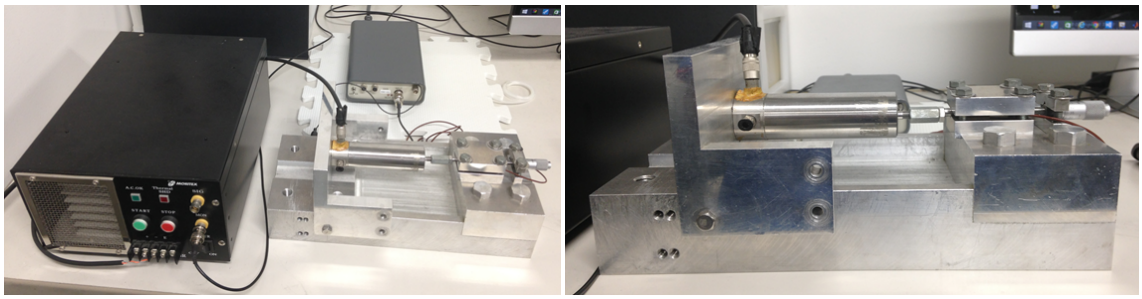

FIGURE 5.2: The diagram of experimental test-bed considered in this section.

i.e., $e_k \to 0$ as $k \to \infty$. Finally, it can be established that the tracking error will approach to zero asymptotically as k goes to infinity.

5.3 Experimental Verification

This section is devoted to the implementation of the formulated DMRAC framework in a real case application. Subsection 5.3.1 discusses the experimental environment and the dedicated setup. Then, Subsection 5.3.2 presents the experimental results along with the discussions.

Fig. 5.2 and 5.3 depict the setup of experimental platform used in this section. The GMA (a) MA-50/6-ac GMA (MORITEX Corporation, Japan) is driven by an analog input signal from the PC-based real-time controller after being amplified by MO24BR GMA driver (b) (MORITEX Corporation, Japan).

The contactless PS-1A (c) capacitive displacement sensor provides the real-time output measurement via a probe (d) which attached at the end of the GMA. For the optimal output measurement, the offset distance of the probe is maintained between 50 μm and 60 μm from the tip of the GMA using the micrometer head MHS1-13 (e). Similar to experimental setup in Chapter 4, this platform also uses the same analog interface board AIO-163202F-PE for data collection throughout the experimentation. The sampling frequency is set as $2kHz$. The control algorithm is implemented on a personal computer (PC) by C language. The specification details of the experimental equipments are shown in Table 5.1.

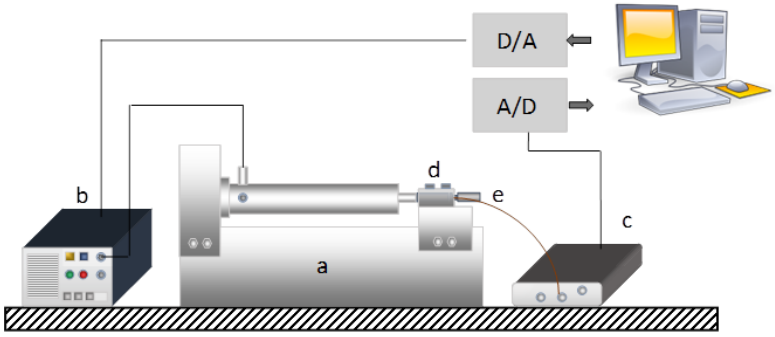

FIGURE 5.3: The diagram of setup environment for the experimental test-bed.

TABLE 5.1: The specification of MORITEX MA-50/6-ac and MORITEX MO24BR

MORITEX MA-50/6-ac	Value (unit)
Resolution	$\pm 20(\mu m)$
Natural Frequency	3000(Hz)
Frequency Range	(DC) 4(kHz)
Maximum Dynamic Force	± 220(N)
Block Force	462(N)
Input Current	± 2(A)
DC Resistance	$4.8(\Omega)$
MORITEX MO24BR	**Value (unit)**
Input Voltage	80 120V (AC)
Input Control	Voltage ± 5(V)
Output Current	± 3(A)
Output Voltage	0 40(V)
Current Protection	$< \pm 3$(A)

5.3.1 Experimental Environment

5.3.2 Experimental Results and Discussion

In this experimental study, we consider three input cases. The first one is the input reference that involving Step and Ramp functions and denoted as Case 1. The second case is Sinusoidal input which similar to Chapter 4 with $1Hz$–$30Hz$ of excitation frequencies (Case 2). While the third case is essentially an input that is a combination of two Sinusoidal functions to imitate the rate-dependent behaviour (Case 3). The performance index for each tracking result is measured and quantified by the RMSE and the MAE.

The initial value for parameters $\hat{\zeta}_{1,0}$, $\hat{\zeta}_{2,0}$, $\hat{\psi}_{1,0}$, $\hat{\psi}_{2,0}$, $\hat{\alpha}_{1,0}$ and $\hat{\alpha}_{2,0}$ are obtained through the offline identification based on EPSO technique discussed in Chapter 3. In this way,

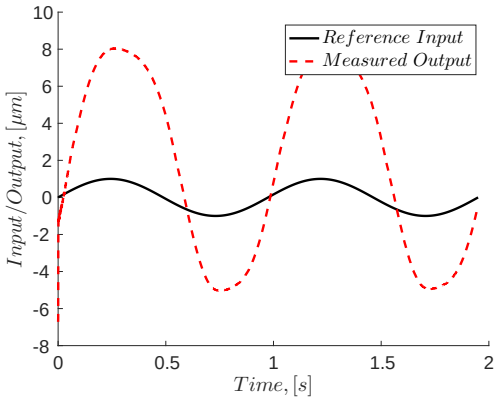

(A) Plot of Input/Output vs. time for $1Hz$ input frequency.

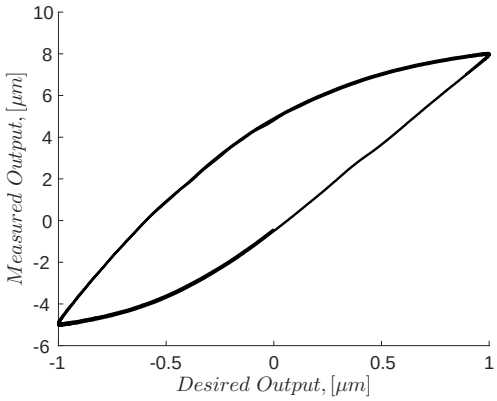

(B) Measured of input-output curves for $1Hz$ input frequency.

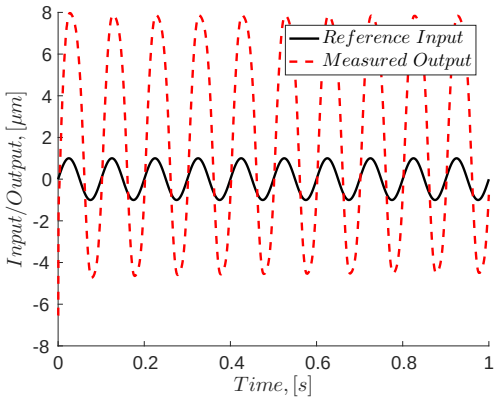

(C) Plot of Input/Output vs. time for $10Hz$ input frequency.

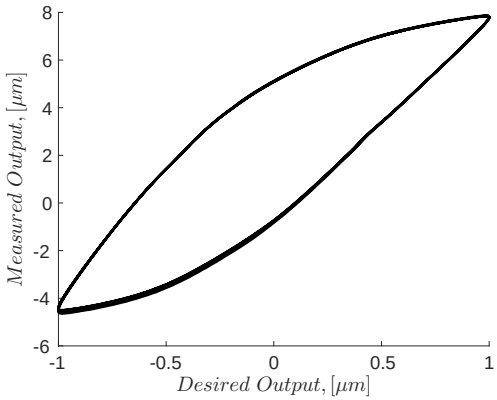

(D) Measured of input-output curves for $10Hz$ input frequency.

FIGURE 5.4: The input-output plot of the GMA without any control effort corresponding to Case 2 input trajectories.

the initial estimate for each parameter is set as $\hat{\zeta}_{1,0} = \hat{\zeta}_{2,0} = 0.008$, $\hat{\psi}_{1,0} = \hat{\psi}_{2,0} = -0.002$, and $\hat{\alpha}_{1,0} = \hat{\alpha}_{2,0} = -0.005$. The parameter adaptation gain κ is set as 0.01.

Prior to the control implementation, we conduct several open-loop experiments to have an insight of the hysteresis phenomenon in the GMA. Fig. 5.4 shows the plot of input-output relations for the GMA without any control scheme. These experimental data show that the hysteresis phenomenon in magnetostrictive based actuators are rate-dependent. This behaviour can also be seen clearly in Fig. 3.12 through Fig. 3.19 of Chapter 3. The shape of hysteresis loop is changing with respect to the input frequency. In comparison to the open-loop condition of PEA stage in Chapter 3 and 4, the affected hysteretic behaviour in GMA is more serious. Strong hysteresis effects are observed even in low input frequency, particularly at $1Hz$. In this case, it can be witnessed that the output is amplified to a staggering seven times of the desired input reference.

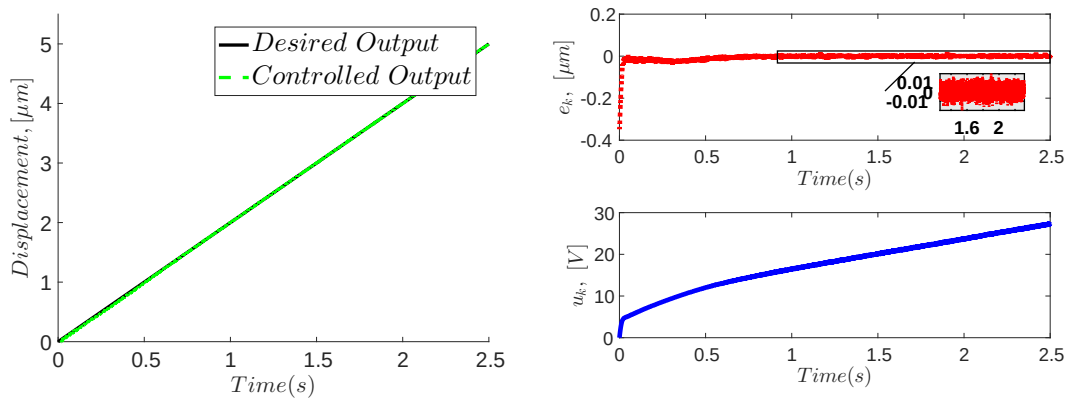

(A) Comparison of Desired output and Controlled output.

(B) The plots of tracking error e_k and control effort u_k.

FIGURE 5.5: The tracking performance for the Ramp input case.

It is shown in Chapter 3 that with the help of EPSO technique, the proposed MBW model (5.1) is able to capture the dynamic and hysteretic behavior of the GMA with a sound accuracy. Furthermore, the proposed MBW model is infused with rate-dependent property. Thus, the application of this model would help improving the tracking performance in GMA.

Subsection **5.3.2.1** gives analysis and discussion about performance tracking with respect to above mentioned three input cases, while subsection that follows further analyse the sensitivity of parameters estimates and effect of adaptive gain κ in performance tracking.

5.3.2.1 Performance Tracking

At first, reference signals of Case 1 are considered. Fig. 5.5 and Fig. 5.6 depict the output tracking performance for the Ramp and Step-Ramp inputs respectively. It can be clearly noticed that the real displacements of the GMA track the reference trajectories very well. The tracking errors in the steady-state are recorded as within $-0.01\mu m$ to $0.01\mu m$ for both inputs.

Next, the tracking experiments for sinusoidal input reference with different frequencies are made, i.e., Case 2. Fig. 5.7 to Fig. 5.9 illustrate the graphical results for the motion and tracking error with $5Hz$, $10Hz$, and $20Hz$ excitation frequencies. In addition, the steady-state errors for the respective input frequencies are recorded as $\pm$0.02 μm, $\pm$0.05 μm, and $\pm$0.1 μm respectively. Meanwhile, Fig. 5.10 depicts the results

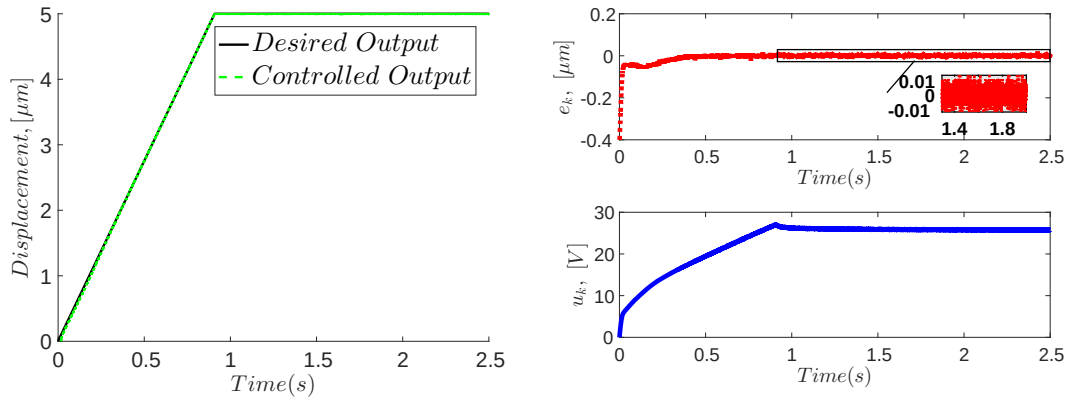

(A) Comparison of Desired output and Controlled output.

(B) The plots of tracking error e_k and control effort u_k.

FIGURE 5.6: The tracking performance for the combination of Step-Ramp input case.

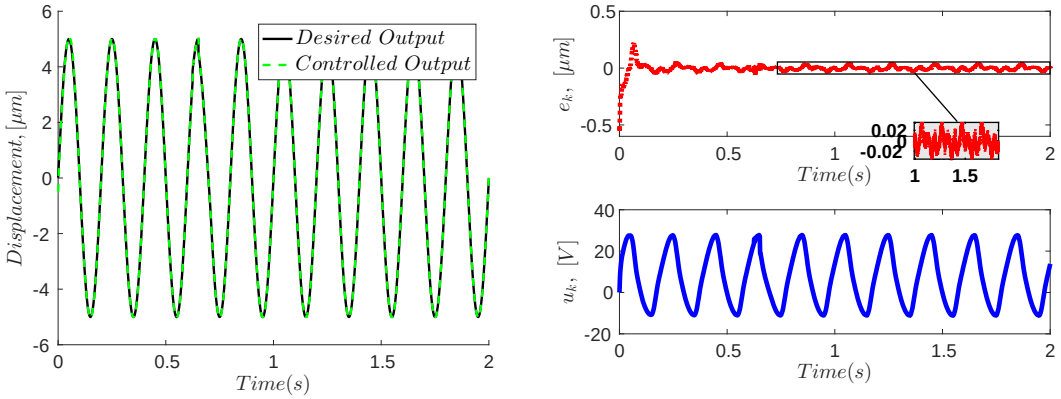

(A) Comparison of Desired output and Controlled output.

(B) The plots of tracking error e_k and control effort u_k.

FIGURE 5.7: The tracking performance for the sinusoidal reference (A $5Hz$ input case).

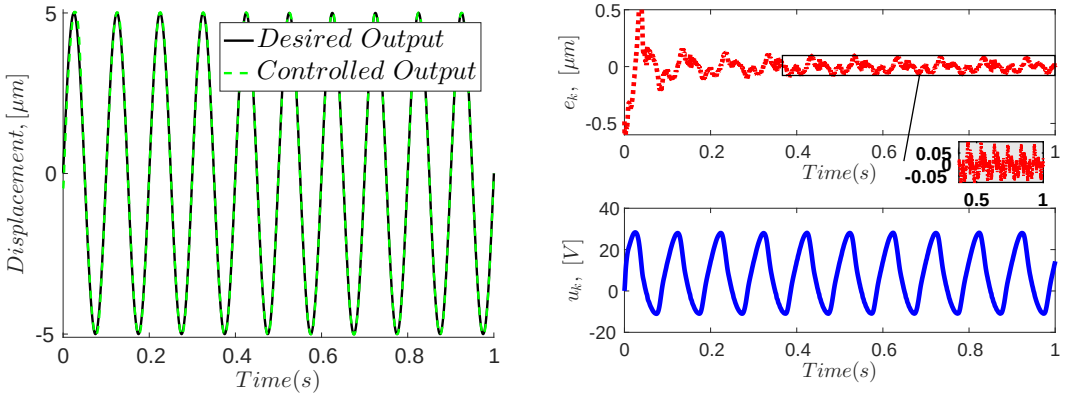

(A) Comparison of Desired output and Controlled output.

(B) The plots of tracking error e_k and control effort u_k.

FIGURE 5.8: The tracking performance for the sinusoidal reference (A $10Hz$ input case).

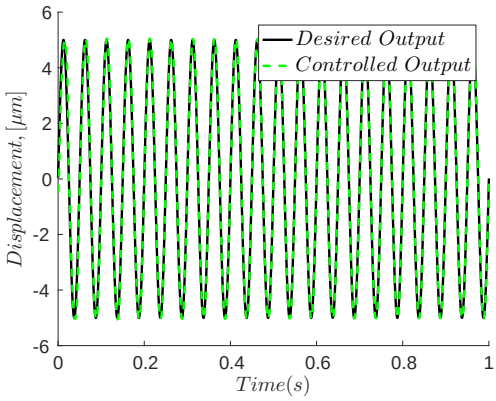

(A) Comparison of Desired output and Controlled output.

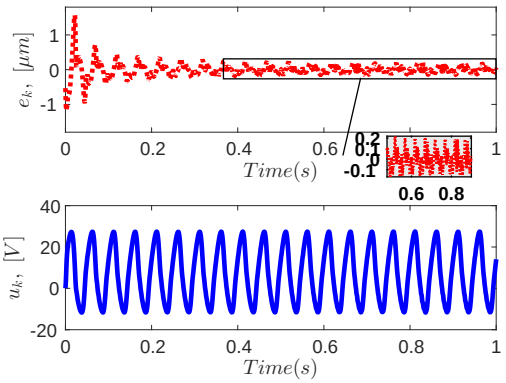

(B) The plots of tracking error e_k and control effort u_k.

FIGURE 5.9: The tracking performance for the sinusoidal reference (A $20Hz$ input case).

of input-output relations in the closed-loop condition concerning $5Hz$ and $10Hz$ input frequencies.

TABLE 5.2: The Summary of the Tracking Performance for Case 1 and Case 2 Input Trajectories

	Performance Index	
Type of Input	RMSE (μm)	MAE (μm)
Step	0.0044	0.0174
Ramp	0.0060	0.0299
Step + Ramp	0.0054	0.0201
Sinusoidal (1 Hz)	0.0056	0.0237
Sinusoidal (5 Hz)	0.0175	0.0565
Sinusoidal (10 Hz)	0.0379	0.1197
Sinusoidal (20 Hz)	0.0877	0.3283
Sinusoidal (30 Hz)	0.1695	0.4605

Meanwhile, Table 5.2 summarizes the tracking performance in terms of RMSE and MAE for Case 1 and Case 2 input references. The performance index for the inputs related to Case 1 are much better compared to Case 2. This situation is common because less control effort is needed to regulate the GMA with input trajectories of Case 1 compared to Case 2. Furthermore, the input trajectories of Case 2 are slightly complicated than in Case 1.

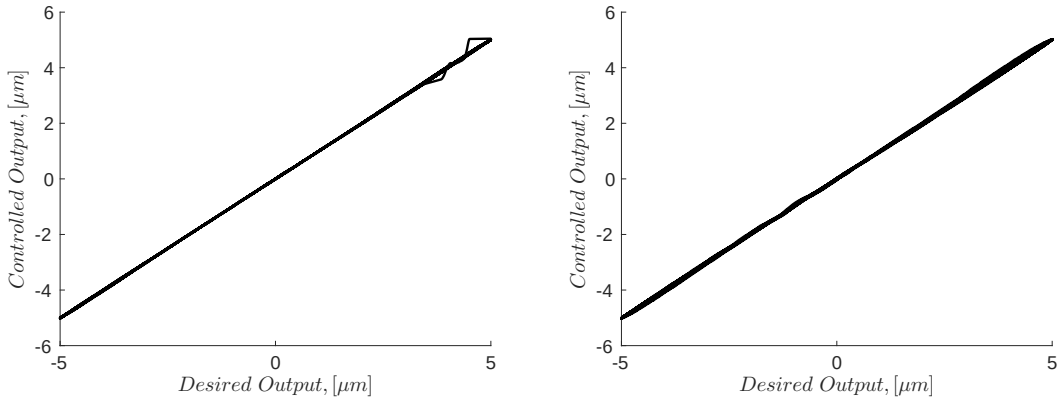

(A) Case 2 with $5Hz$ input frequency.

(B) Case 2 with $10Hz$ input frequency.

FIGURE 5.10: The plot of input-output relations with DMRAC scheme (Closed-loop condition).

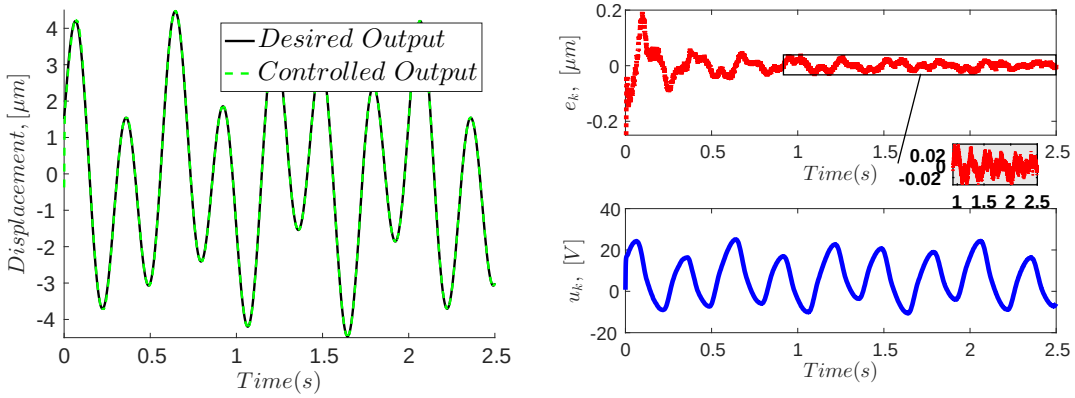

(A) Comparison of Desired output and Controlled output.

(B) The plots of tracking error e_k and control effort u_k.

FIGURE 5.11: The tracking performance for the case of mixed frequency trajectory.

To confirm the effectiveness of the rate-dependent property in hysteresis compensation, Case 3 is considered. The reference signal is composed of two sinusoidal waves and is designed as $y_d = 3.0*sin(2*\pi*3.5*k*0.0005)+1.5*cos(2*\pi*1.5*k*0.0005)$. The results pertaining to this mixed reference input are illustrated in Fig. 5.11. As can be seen in Fig. 5.11, good tracking performance is obtained and the range of steady-state error is within $\pm 0.02\mu$m.

The results of the parameter estimates of $\hat{\zeta}_{1,k}$, $\hat{\zeta}_{2,k}$, $\hat{\psi}_{1,k}$, $\hat{\psi}_{2,k}$, $\hat{\alpha}_{1,k}$ and $\hat{\alpha}_{2,k}$ corresponding to above tracking performance (Case 1 - Case 3 input references) are illustrated in Fig. 5.12-5.14. As shown in these figures, it can be witnessed that in all cases the estimates of $\hat{\zeta}_{2,k}$, $\hat{\psi}_{2,k}$, and $\hat{\alpha}_{2,k}$ vary slowly compared to their counterparts.

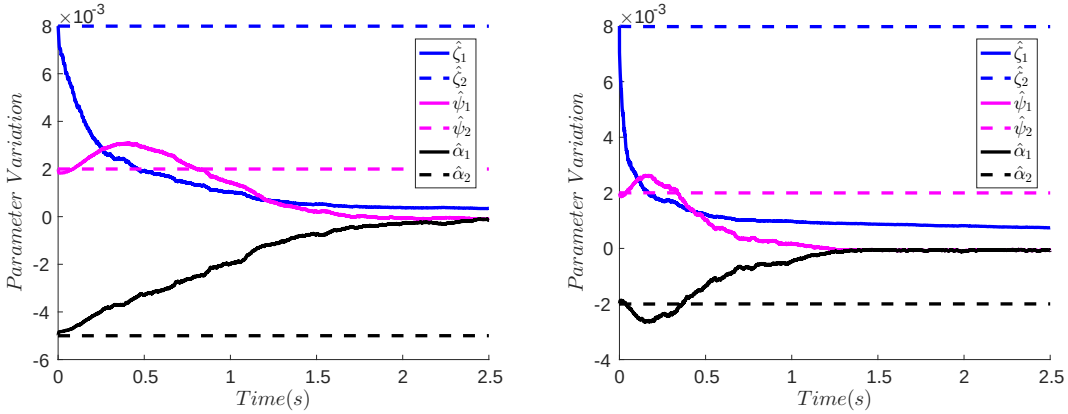

(A) Case 1 with Ramp input. (B) Case 1 with Step-Ramp input.

FIGURE 5.12: The variations of the parameter estimates for the Case 1 inputs.

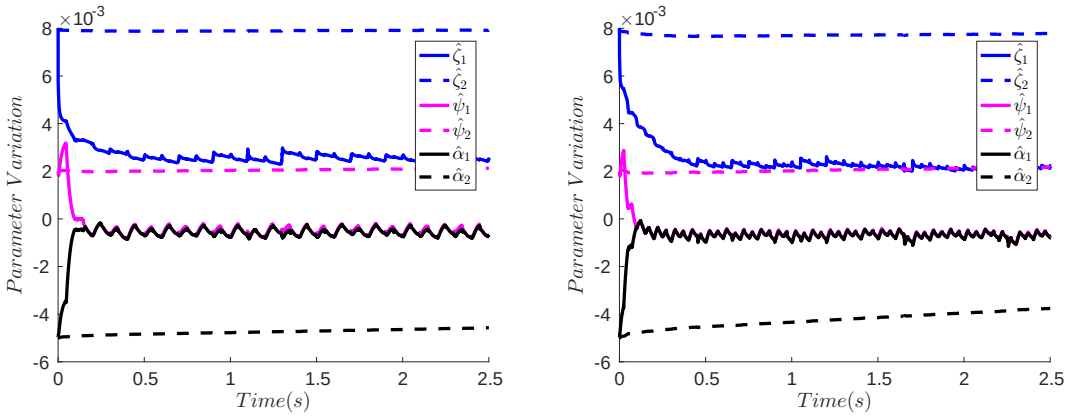

(A) Case 2 with $5Hz$ input frequency. (B) Case 2 with $10Hz$ input frequency.

FIGURE 5.13: The variations of the parameter estimates for the Case 2 inputs.

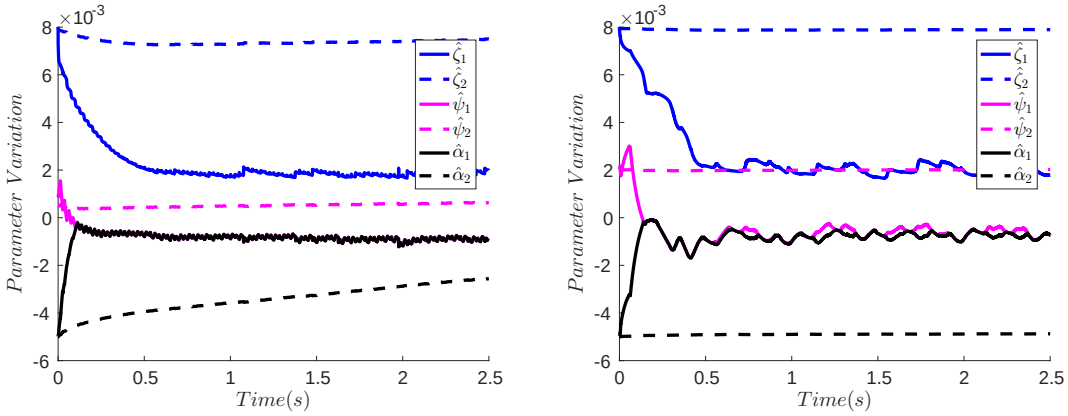

(A) Case 2 with $20Hz$ input frequency. (B) Case 3 input.

FIGURE 5.14: The variations of the parameter estimates for Case 2 and Case 3 references.

In addition, it can be observed that the control efforts for each case are stable throughout the experiments.

5.3.2.2 Sensitivity of Parameter Estimates

This Subsection provides analysis pertaining to sensitivity of parameter estimates when their initial values are set at different points and far from their boundaries of true values. Additionally, the effect of adaptive gain κ is studied. Table 5.3 tabulates initial points of each parameter estimate considered in this section. Note that identified initials (CS0) are the initial points used in experimental studies of the previous section. In this section, we are interested to observe the behaviour of parameter estimates when their initials or (one of the initials) are/is set 2.2 times (CS1), 10 times (CS2), and 100 times (CS3) farther from CS0.

TABLE 5.3: Initial points of respective parameter estimates $\hat{\zeta}_{1,0}$, $\hat{\zeta}_{2,0}$, $\hat{\psi}_{1,0}$, $\hat{\psi}_{2,0}$, and $\hat{\alpha}_{1,0}$, and $\hat{\alpha}_{2,0}$.

Parameter	Identified initial (CS0)	2.2x (CS1)	10x (CS2)	100x (CS3)
$\hat{\zeta}_{1,0}$	0.008	0.0176	0.08	0.8
$\hat{\zeta}_{2,0}$	0.008	0.0176	0.08	0.8
$\hat{\psi}_{1,0}$	-0.002	0.0044	-0.02	-0.2
$\hat{\psi}_{2,0}$	-0.002	0.0044	-0.02	-0.2
$\hat{\alpha}_{1,0}$	-0.005	0.0011	-0.05	-0.5
$\hat{\alpha}_{2,0}$	-0.005	0.0011	-0.05	-0.5

TABLE 5.4: Comparison of Tracking Performance Between CS0 and CS1 Cases.

	Performance Index	
Type of Input	CS0-RMSE (μm)	CS1-RMSE (μm)
Step	0.0044	0.0048
Step + Ramp	0.0068	0.0051
Sinusoidal (5 Hz)	0.0175	0.0174
Sinusoidal (10 Hz)	0.0379	0.0390
Sinusoidal (20 Hz)	0.0877	0.0906

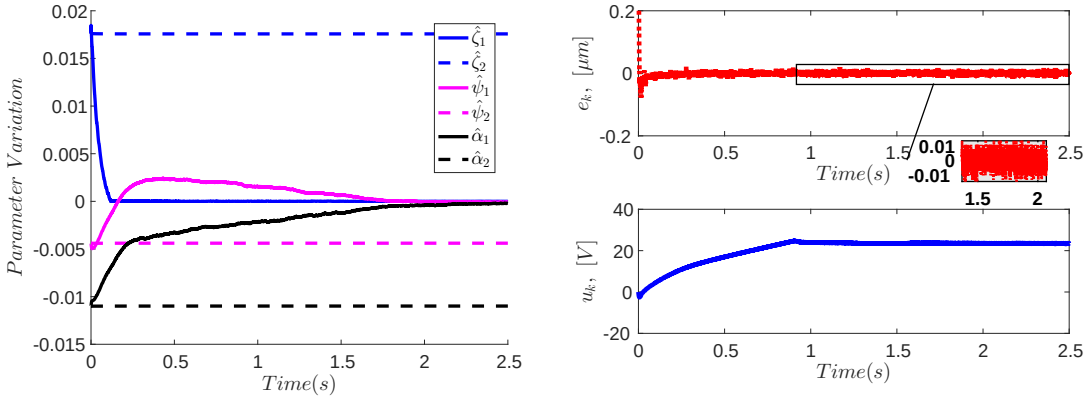

(A) The variations of each parameter estimate for Step-Ramp input.

(B) The plots of tracking error e_k and control effort u_k.

FIGURE 5.15: The variations of each parameter estimate for CS1 pertaining to Case 1 input and the corresponding tracking performance.

First, a comparison of tracking performance between CS0 and CS1 cases are made. Table 5.4 indicates the performance index in terms of RMSE for different types of input trajectories. The adaptive gain κ is set to be the same in both cases, i.e., $\kappa = 0.01$. As can be observed in Table 5.4, no significant changes are noticed by moving the initial point of the estimates by 2.2 times from CS0. The graphical results related to CS1 case can be found in Fig. 5.15 through Fig. 5.17. The variation of parameter estimates $\hat{\zeta}_{2,k}$, $\hat{\psi}_{2,k}$, and $\hat{\alpha}_{2,k}$ (denoted as G2 estimates in following statements) are plotted individually as can be seen in Fig. 5.17. The results in Fig. 5.17 indicate that sensitivity of G2 estimates are increasing with frequency changes. Almost no adaptation occurred when simple input references are employed, or in other words, G2 estimates are stagnant in the case of Step input. This phenomenon is natural and can be easily explained by referring adaptive laws (5.13), (5.15), and (5.17). The associated term to G2 estimates is a product

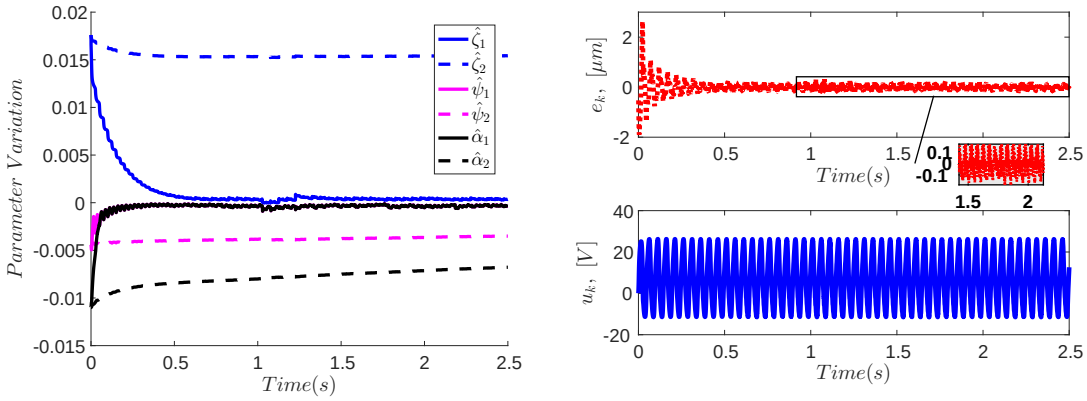

(A) The variations of each parameter estimate for Sinusoidal $20Hz$ input.

(B) The plots of tracking error e_k and control effort u_k.

FIGURE 5.16: The variations of each parameter estimate for CS1 pertaining to Case 2 input and the corresponding tracking performance.

of difference terms ν_k and $r_{u,k}$, thus give rise to slow variation and adaptation.

Meanwhile, Fig. 5.18 depicts the tracking performance related to CS2 case for Sinusoidal input (5Hz frequency) when only one parameter estimate is set slightly farther from CS0. In this case, only $\hat{\zeta}_{2,0}$ is set as 10 times farther from the others. The parameter adaptation gain κ is set as 0.01. It can be seen that the variation of $\hat{\zeta}_{2,k}$ is very small and almost insignificant in comparison to others. However, the performance tracking result as shown in Fig. 5.18b indicate that even a single change in initial point affects the tracking error where the recorded RMSE is about 0.0565 and is about 3 times higher compared to the one tabulated in Table 5.2 (refer to Sinusoidal ($5Hz$)).

Next, CS3 case is considered. In this experimental study, two conditions are tested and assessed. First, only the original parameter estimates $\hat{\zeta}_{1,k}$, $\hat{\psi}_{1,k}$, and $\hat{\alpha}_{1,k}$ (G1 estimates) are initialized at CS3. Second, only G2 estimates are initiated at CS3 while others at CS0. The parameter adaptation gain κ is set as 0.005 for every assessment. Results pertaining to both conditions are depicted in Fig. 5.19 and Fig. 5.20. As shown in Fig. 5.19, the G1 estimates are very sensitive, that fast adaptation can be seen even κ value is relatively small. In spite of good tracking error in the steady state, the attitude of control signal is less stable. On the other hand, when only G2 estimates are initialized at CS3, large tracking error is observed as can be seen in Fig. 5.20 despite stable attitude of control signal u_k.

Finally, assessments on the behaviour of parameter estimates corresponding to different values of κ are made. Fig. 5.21 – Fig.5.26 provide the plot of each parameter

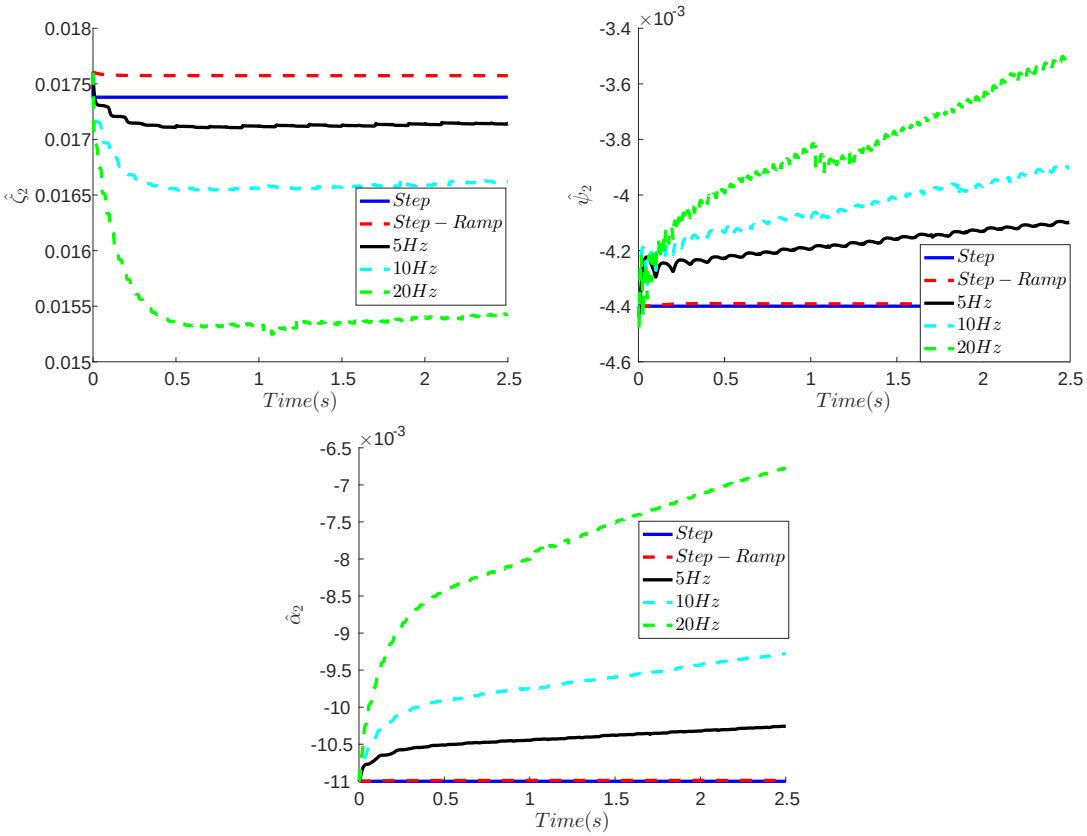

FIGURE 5.17: The variations of G2 parameter estimates for CS1 case in corresponding to different input trajectories..

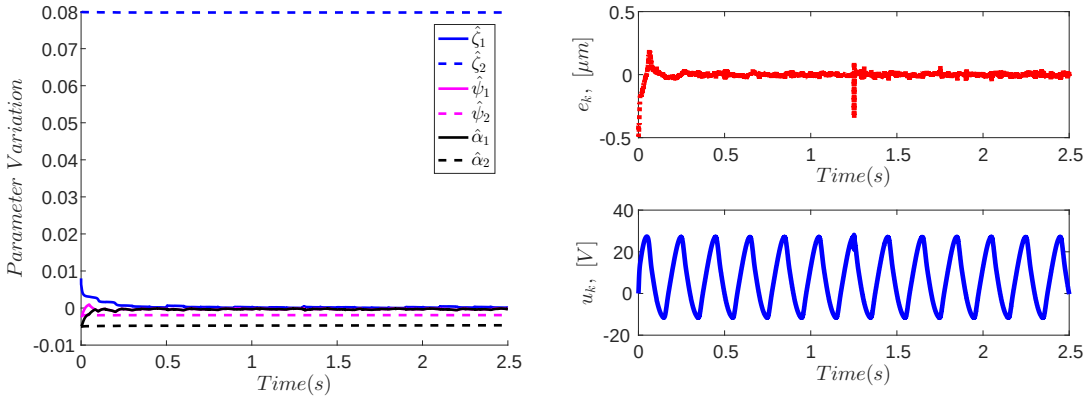

(A) The variations of each parameter estimate for Sinusoidal $5Hz$ input.

(B) The plots of tracking error e_k and control effort u_k.

FIGURE 5.18: The variations of each parameter estimate for Case 2 input and the corresponding tracking performance when only $\hat{\zeta}_{2,0}$ is initiated at CS2.

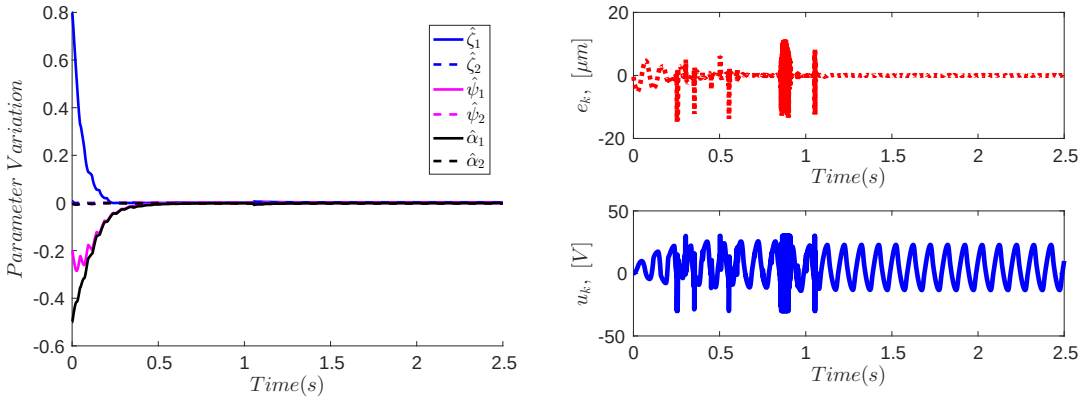

(A) The variations of each parameter estimate for Sinusoidal $10Hz$ input.

(B) The plots of tracking error e_k and control effort u_k.

FIGURE 5.19: Parameter variations for Case 2 input and the corresponding tracking performance when only G1 parameter estimates are initialized at CS3).

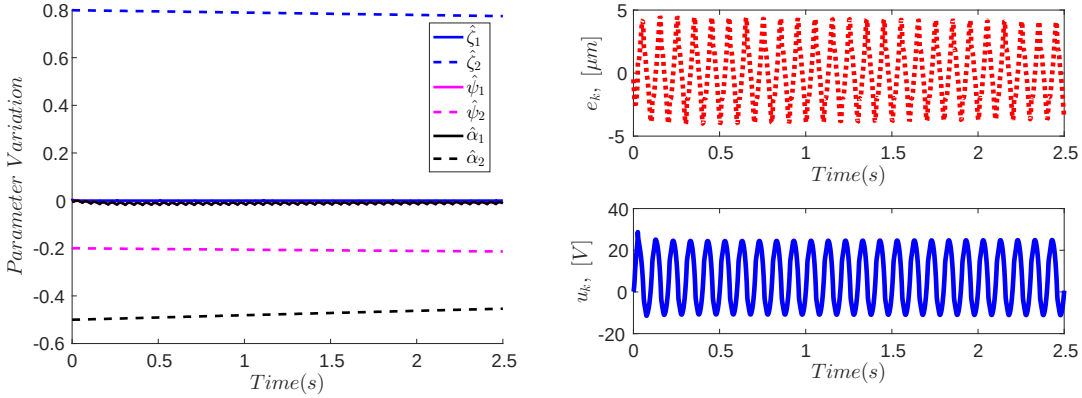

(A) The variations of each parameter estimate for Sinusoidal $10Hz$ input.

(B) The plots of tracking error e_k and control effort u_k.

FIGURE 5.20: Parameter variations for Case 2 input and the corresponding tracking performance when only G2 parameter estimates are initialized at CS3).

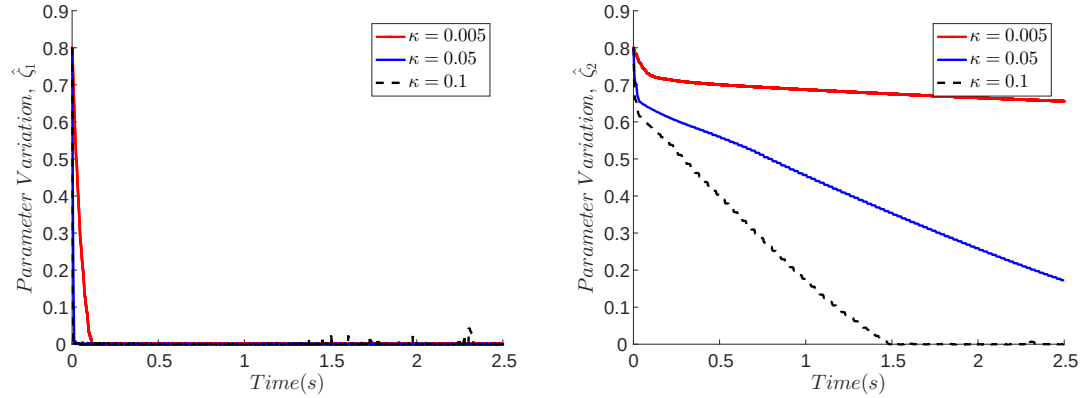

(A) The adaptation behaviour of $\hat{\zeta}_{1,k}$.

(B) The adaptation behaviour of $\hat{\zeta}_{2,k}$.

FIGURE 5.21: The variations of parameter $\hat{\zeta}_{1,k}$ and $\hat{\zeta}_{2,k}$ estimates for Case 2 input ($20Hz$ frequency) pertaining to different value of κ.

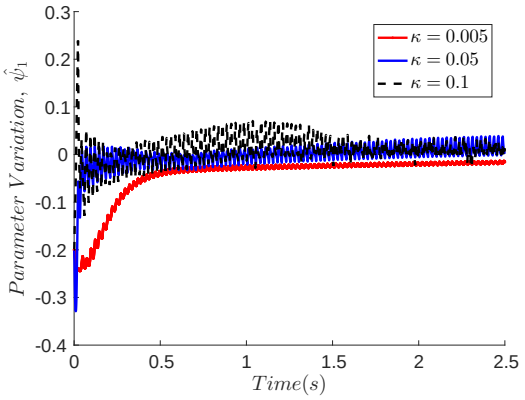

(A) The adaptation behaviour of $\hat{\psi}_{1,k}$.

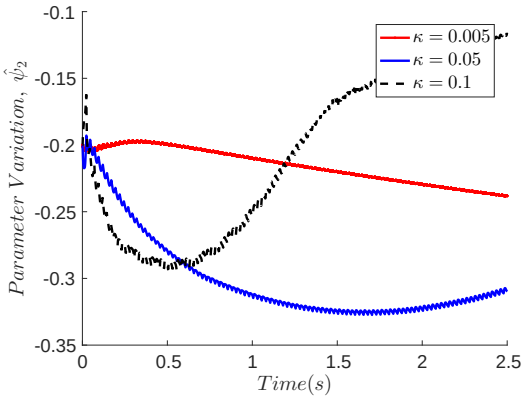

(B) The adaptation behaviour of $\hat{\psi}_{2,k}$.

FIGURE 5.22: The variations of parameter $\hat{\psi}_{1,k}$ and $\hat{\psi}_{2,k}$ estimates for Case 2 input ($20Hz$ frequency) pertaining to different value of κ.

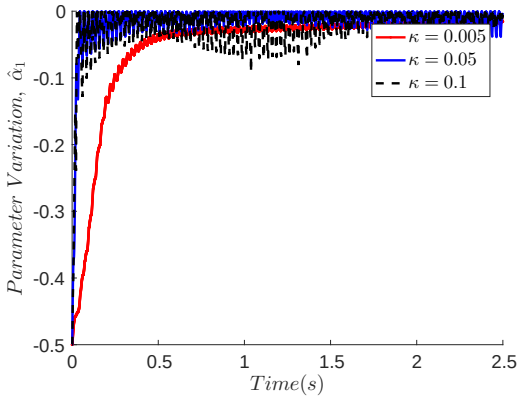

(A) The adaptation behaviour of $\hat{\alpha}_{1,k}$.

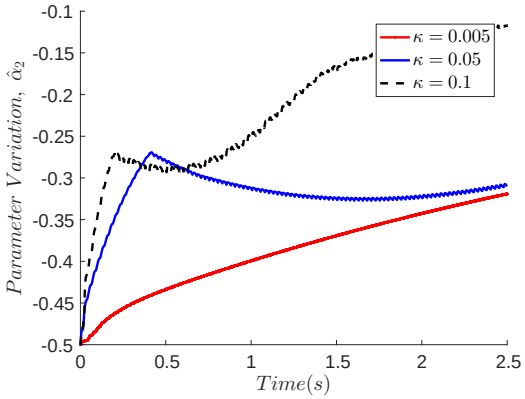

(B) The adaptation behaviour of $\hat{\alpha}_{2,k}$.

FIGURE 5.23: The variations of parameter $\hat{\alpha}_{1,k}$ and $\hat{\alpha}_{2,k}$ estimates for Case 2 input ($20Hz$ frequency) pertaining to different value of κ.

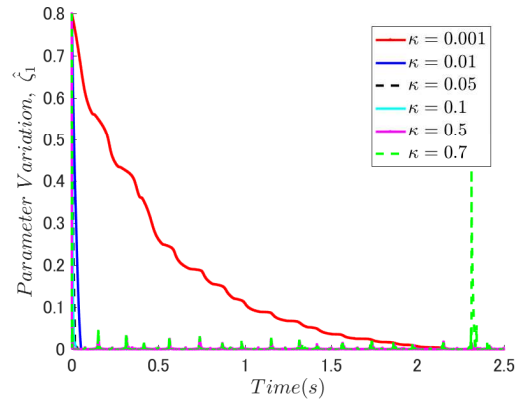

(A) The adaptation behaviour of $\hat{\zeta}_{1,k}$.

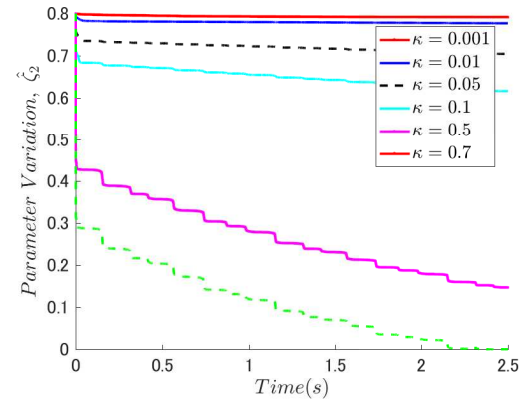

(B) The adaptation behaviour of $\hat{\zeta}_{2,k}$.

FIGURE 5.24: The variations of parameter $\hat{\zeta}_{1,k}$ and $\hat{\zeta}_{2,k}$ estimates for Case 3 input case pertaining to different value of κ.

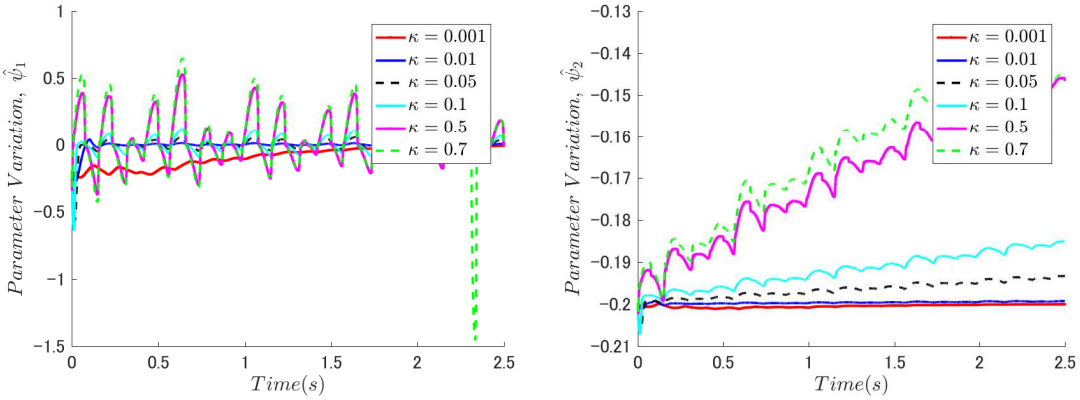

(A) The adaptation behaviour of $\hat{\psi}_{1,k}$. (B) The adaptation behaviour of $\hat{\psi}_{2,k}$.

FIGURE 5.25: The variations of parameter $\hat{\psi}_{1,k}$ and $\hat{\psi}_{2,k}$ estimates for Case 3 input case pertaining to different value of κ.

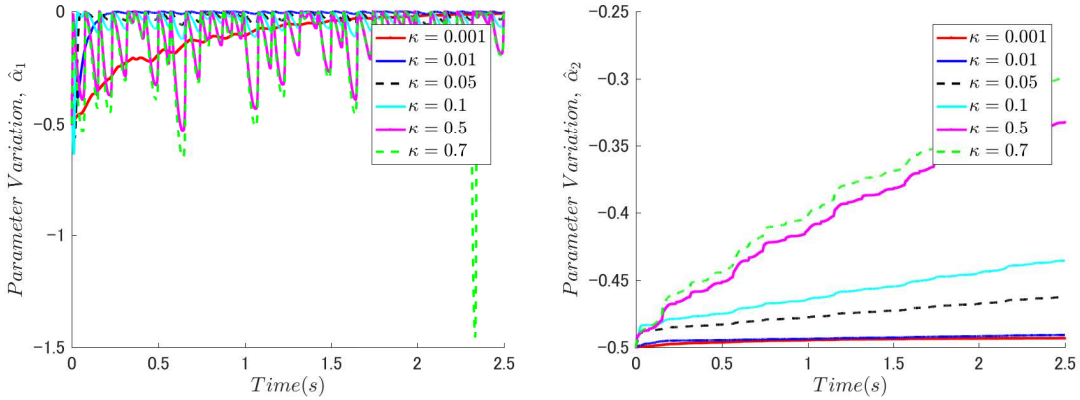

(A) The adaptation behaviour of $\hat{\alpha}_{1,k}$. (B) The adaptation behaviour of $\hat{\alpha}_{2,k}$.

FIGURE 5.26: The variations of parameter $\hat{\alpha}_{1,k}$ and $\hat{\alpha}_{2,k}$ estimates for Case 3 input case pertaining to different value of κ.

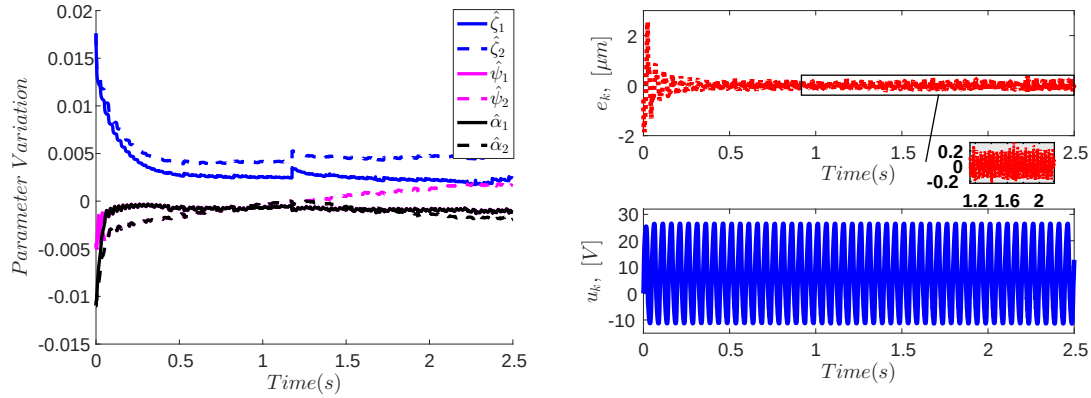

(A) The variations of each parameter estimate for Sinusoidal $20Hz$ input frequency. (B) The plots of tracking error e_k and control effort u_k.

FIGURE 5.27: Parameter variations for Case 2 input with $\kappa_1 = 0.01$, $\kappa_2 = 0.07$ and the corresponding tracking performance when all parameter estimates are initialized at CS1. (RMSE = 0.0909)

TABLE 5.5: The Summary of the Tracking Performance for Case 2 reference ($20Hz$ frequency) with different κ value (all parameter estimates are initialized at CS3).

	Performance Index	
κ value	RMSE (μm)	MAE (μm)
0.005	3.5899	6.0959
0.05	2.8551	5.5836
0.1	2.1473	6.3543

TABLE 5.6: The Summary of the Tracking Performance for Case 3 input with different κ value (all parameter estimates are initialized at CS3).

	Performance Index	
κ value	RMSE (μm)	MAE (μm)
0.001	1.2924	2.2789
0.01	0.1255	0.4662
0.05	0.1089	0.3074
0.1	0.1038	0.3299
0.5	0.0742	0.3495
0.7	0.2465	3.3889

estimate for two cases related to Case 2 input and Case 3 at different value of κ. For Case 2, we consider Sinusoidal reference with $20Hz$ input frequency. In this case, three different values of κ are studied. Meanwhile, for Case 3 input, six κ values are considered. In these experimental studies, the initial point of all estimates are set at CS3. The behaviours of parameter estimates pertaining to Case 2 input are illustrated in Fig. 5.21 to Fig. 5.23. Since the input frequency is slightly high, experiments with smaller κ values are studied. In this regard, κ is set as $\kappa \leq 0.1$ to maintain the stability of the closed-loop system. Comparing the six results in Fig. 5.21 – Fig. 5.23, it can be seen that each parameter estimate is sensitive with respect to κ value. Large tracking errors are obtained and the RMSE for each κ value is tabulated and shown in Table 5.5. A closer inspection of Table 5.5 shows that RMSE value is reduced as κ is increased.

The sensitivities of parameter estimates pertaining to Case 3 input are depicted through Fig. 5.24 to Fig. 5.26. It can be observed that as κ value increasing, the estimates become more sensitive, in particular $\hat{\zeta}_{1,k}$, $\hat{\psi}_{1,k}$, and $\hat{\alpha}_{1,k}$. Their behaviours are

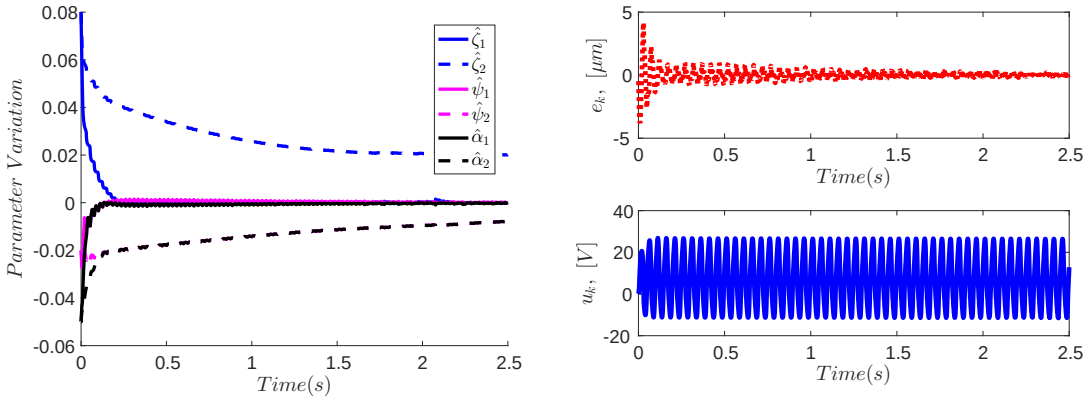

(A) The variations of each parameter estimate for Sinusoidal $20Hz$ input frequency.

(B) The plots of tracking error e_k and control effort u_k.

FIGURE 5.28: The variations of each parameter estimate for Case 2 input with $\kappa_1 = 0.015$, $\kappa_2 = 0.07$ and the corresponding tracking performance when all parameter estimates are initialized at CS2. (RMSE = 0.2338)

unstable when κ is increased over 0.5, as can be seen for example when $\kappa = 0.7$. Observation on the G2 estimates, i.e., $\hat{\zeta}_{2,k}$, $\hat{\psi}_{2,k}$, and $\hat{\alpha}_{2,k}$ suggest that they are much stable compared to G1 estimates due to small adaptation attribute. Meanwhile, Table 5.6 tabulates the performance index in corresponding to this assessment. The best κ value for this case is 0.5 as can be observed in Table 5.6. However, a closer inspection to Fig. 5.24a, Fig. 5.25a, and Fig. 5.26a suggest that the variations of G1 estimates are not so stable, and may give problem to closed-loop system.

To improve the adaptation sensitivity of G2 estimates is quite straightforward. Intuitively, one can introduce individual adaptation gain to each adaptive law instead of using a single adaptation gain κ so that the variation of each estimate can be appropriately controlled. Fig. 5.27 and Fig. 5.31 show the behaviour of parameter estimates and tracking performances of Case 2 and Case 3 respectively. In these examples, two adaptive gains κ_1 and κ_2 are used to control the adaptation attribute of the G1 estimates and their counterparts. In addition, all estimates are initialized at CS1, CS2 and CS3 respectively. Significant difference is noticed when parameter variations of Fig. 5.27 are compared with the one in Fig. 5.16. Indeed, by tuning adaptive gains κ_1 and κ_2, better tracking performance can be obtained even all the estimates are initiated slightly far from their boundary of true values. However, this is only valid for lower input frequencies. At higher frequencies, it is best to initiate the estimates within $\leq$ CS2.

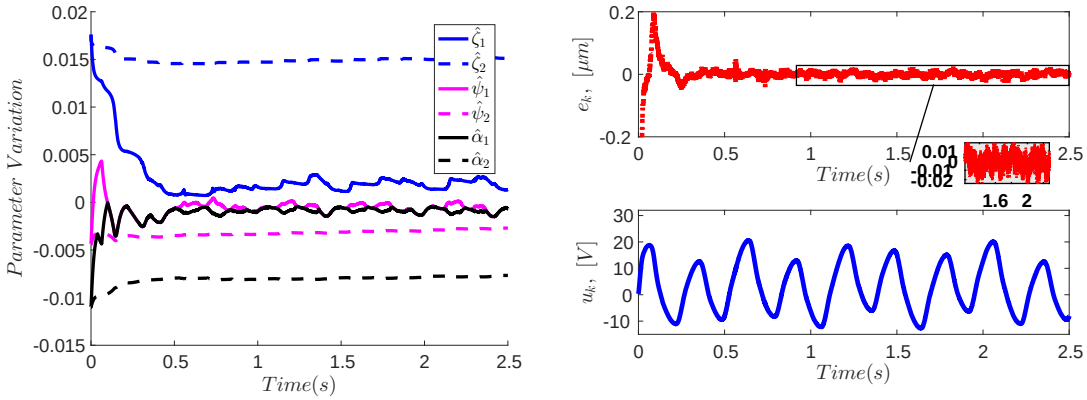

(A) The variations of each parameter estimate. (B) Plots of tracking error e_k & control effort u_k.

FIGURE 5.29: Parameter variations for Case 3 input with $\kappa_1 = 0.01$, $\kappa_2 = 0.1$ and the corresponding tracking performance when all parameter estimates are initialized at CS1 (RMSE = 0.0085).

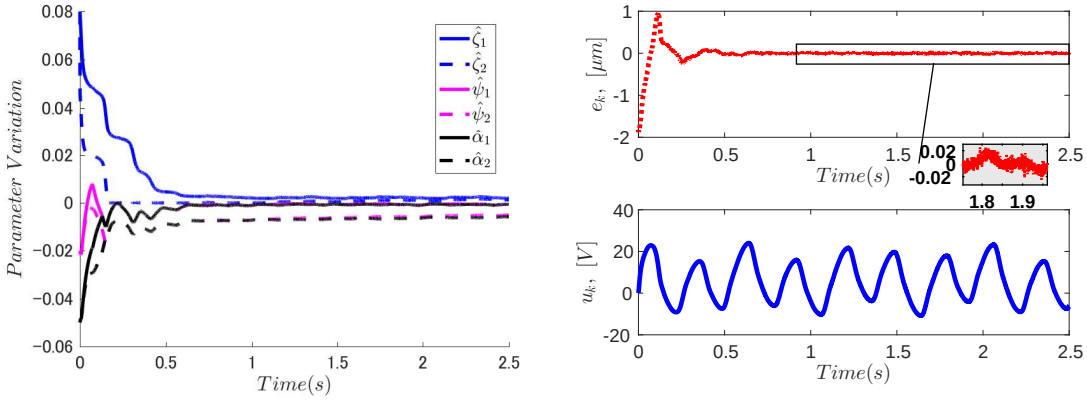

(A) The variations of each parameter estimate. (B) Plots of tracking error e_k & control effort u_k.

FIGURE 5.30: Parameter variations for Case 3 input with $\kappa_1 = 0.005$, $\kappa_2 = 0.3$ and the corresponding tracking performance when all parameter estimates are initialized at CS2 (RMSE = 0.0323).

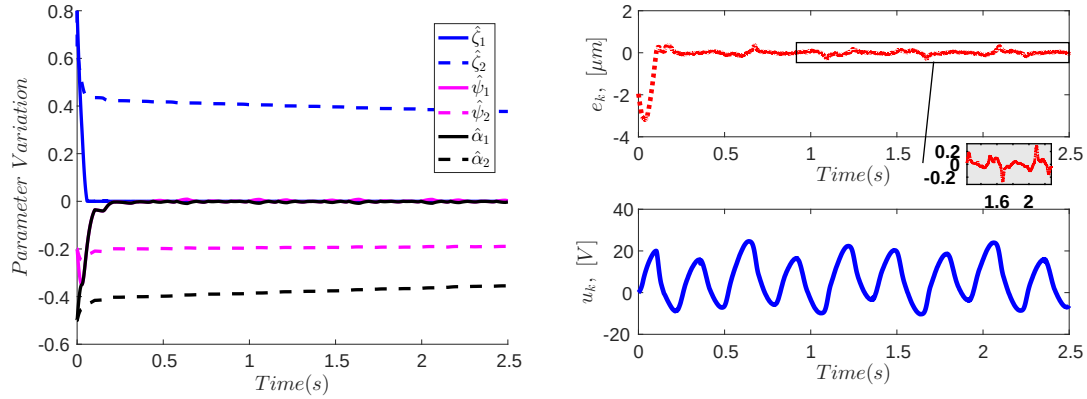

(A) The variations of each parameter estimate. (B) Plots of tracking error e_k & control effort u_k.

FIGURE 5.31: Parameter variations for Case 3 input with $\kappa_1 = 0.01$, $\kappa_2 = 0.2$ and the corresponding tracking performance when all parameter estimates are initialized at CS3 (RMSE = 0.0794).

5.4 Concluding Remarks

In this chapter, an adaptive controller design methodology is presented. Its development is based on the discrete-time modified Bouc-Wen model. Through the theoretical analysis, we can see that the formulated adaptive controller assures the stability of the closed-loop control system. Additionally, the effectiveness of the DMRAC scheme is verified through a real case study. Experimental results have clearly exhibited excellent output tracking performance via the designed control strategy.

Chapter 6

Conclusions and Recommendations

6.1 Conclusions

In the first part of the thesis, feasibility study of the DEB models towards hysteresis characterization is conducted. Through the theoretical and simulation analyses, we learnt that this category of model provides a simple modeling framework without compromising its underlying physical meanings. In addition, all the DEB models are bounded. Besides, it is obvious that Duhem model is capable of describing complex hysteresis curves that are akin to hysteresis phenomenon in the real applications. However, it is a challenge to determine proper shape functions that best describe the real hysteresis effects. Furthermore, a good model does not guarantee its viability from a control standpoint. It is shown that only BW model is the most practical one with regard to direct control fusion. The key point to this success lies in its unique structure that allows the control designer to handle $|\dot{u}|$ term appropriately.

The second part of the thesis is devoted to modeling and control of the smart actuators. A new model modification is proposed to solve rate-independent property of the original BW model. In this case, the special case of BW model is used as the basis for developing the modified one and its establishment is realized in the discrete-time domain. This consideration is taken to avoid numerical approximation which normally degrades the system performance. Moreover, most of the equipments and experimental test rigs are in digital environment. From numerical simulation results, it is observed that the proposed model is capable of describing rate-dependent input-output relations. Thus, the modified BW (MBW) model can be classified as a dynamic hysteresis model. Then, model validation process is carried out to verify the capacity of MBW model in terms of modeling and characterization of hysteretic smart actuators. The results show

that estimated outputs of MBW model are well matched with the measured outputs obtained from PEA, GMA, and IPMC. This confirms that MBW model is not unique and shall be capable of fitting and matching the input-output relations of other smart actuators.

Furthermore, the proposed MBW model is directly used in the development of control strategies. Two control architectures are developed in order to alleviate the hysteresis effects in the smart actuators; the first one is discrete nonlinear prescribed performance control (DPPC) scheme which is formulated to compensate hysteresis effects in the PEA stage; while the second one is a robust adaptive control strategy which is designed for GMA. The experimental results substantiate that the proposed control strategies have the capacity for improving the output tracking performance in the smart actuators without compromising the closed-loop systems' stability. These experimental results further confirm the capability of the MBW model. It is not only applicable for modeling and characterization, but also towards control development for the betterment of motion tracking problems in smart actuators that are affected by hysteresis effects.

6.2 Recommendations and Future Works

This thesis has addressed the modeling and controller design of the smart actuators that affected by hysteretic nonlinearity based on DEB hysteresis operator. Certainly, there are still many open problems with regards to the analysis of hysteretic systems. A few suggestions of future work could be considered as an extension to this study. It may become specially interesting to delve into:

• Modeling. The work in this thesis mainly focuses on symmetric and rate-dependent hysteresis. Since in some applications, hysteresis phenomena can be asymmetric, an extension of this work is to establish results for asymmetric BW model or asymmetric DEB hysteresis model.

• Other type of actuators. It might be of interest to extend the application of MBW model for other type of actuators such as smart memory alloy (SMA) or even in other

application fields including magnetorheological dampers, mechanical isolation systems and so forth.

• Tracking. Alternative stabilizing controllers could be designed and fused into MBW model for further improvement of the motion tracking and regulation performance especially for high frequency reference inputs.

Appendix A

Research Achievements

Journal Paper:

1. M. H. M. Ramli and X. Chen (in press), “Modeling and control of piezoelectric actuators by a class of differential equations based hysteresis models”, *Int. J. of Advanced Mechatronic Systems*.

International Conference Proceedings/Papers:

1. M. H. M. Ramli and X. Chen, "Control fusion strategy via differential equations based hysteresis operator," *2016 IEEE International Conference on Mechatronics and Automation, ICMA2016*, Harbin, 2016, pp. 1445-1450. doi: 10.1109/ICMA.2016.7558776
2. M. H. M. Ramli and X. Chen, “An extended Bouc-Wen model based adaptive Control for micro-positioning of smart actuators”, *2016 International Conference on Advanced Mechatronic Systems, ICAMechs2016*, Melbourne, VIC, 2016, pp. 189-194. doi: 10.1109/ICAMechS.2016.7813445
3. M. H. M. Ramli and X. Chen, “Nonlinear discrete prescribed performance control for Micro-Positioning of Smart Actuators”, *IEEE 4th International Symposium on Robotics and Intelligent Sensors, IRIS2016*.

Bibliography

Al-Janaideh, M. and Krejci, P. (2012). "Inverse rate-dependent Prandtl–Ishlinskii model for feedforward compensation of hysteresis in a piezomicropositioning actuator". In: *IEEE/ASME Trans. Mechatron* 18.5, pp. 1498 –1507.

Alrasheed, M. R., de Silva, C. W., and Gadala, M. S. (2007). "A new extension of particle swarm optimization and its application in electronic heat sink design". In: *ASME 2007 International Mechanical Engineering Congress and Exposition*. Vol. 8, pp. 1221–1230.

Bechlioulis, C. P. and Rovithakis, G. A. (2011). "Robust Partial-State Feedback Prescribed Performance Control of Cascade Systems With Unknown Nonlinearities". In: *IEEE Trans. on Autom. Control* 56.9, pp. 2224–2230.

Bergh, F. van den and Engelbrecht, A.P. (2006). "A study of particle swarm optimization particle trajectories". In: *Information Sciences* 176.8, pp. 937 –971. DOI: http://dx.doi.org/10.1016/j.ins.2005.02.003.

Bliman, P.-A. J. (1992). "Mathematical study of the Dahl's friction model". In: *Eur. J. Mech. A/Solids* 11.6, pp. 835–848.

Cao, Y. and Chen, X. B. (2015). "A survey of modeling and control issues for piezoelectric actuators". In: *Trans. ASME., J. Dyn. Syst. Meas. Control* 137.1, p. 014001.

Cao, Y., Cheng, L., Chen, X. B., and Peng, J. Y. (2013). "An inversion-based model predictive control with an integral-of-error state variable for piezoelectric actuators". In: *IEEE/ASME Transactions on Mechatronics* 18.3, pp. 895–904.

Chen, Y., Qiu, J., Palacios, J., and Smith, E. C. (2013). "Tracking control of piezoelectric stack actuator using modified Prandtl–Ishlinskii model". In: *J. Intell. Mater. Syst. Struct* 24.6, pp. 753 –760.

Coleman, B. D. and Hodgdon, M. L. (1987). "On a class of constitutive relations for ferromagnetic hysteresis". In: *Arch. Ration. Mech. Anal.* 99.4, pp. 375–396.

Devasia, S., Eleftheriou, E., and Moheimani, S. O. R. (2007). "A Survey of Control Issues in Nanopositioning". In: *IEEE Transactions on Control Systems Technology* 15.5, pp. 802–823.

Dimian, M. and Andrei, P. (2014). *Noise-Driven Phenomena in Hysteretic Systems*. Signals and Communication Technology. New York, NY: Springer.

Du, J., Feng, Y., Su, C. Y., and Hu, Y. M. (2009). "On the robust control of systems preceded by coleman-hodgdon hysteresis". In: *ICCA 2009: IEEE Int. Conf. Control Autom.* Pp. 685–689.

Esbrook, A., Tan, X., and Khalil, H. K. (2014). "Inversion-free stabilization and regulation of systems with hysteresis via integral action". In: *Automatica* 50.4, pp. 1017 –1025. DOI: http://dx.doi.org/10.1016/j.automatica.2013.11.013.

Evers, G. I. and Ghalia, M. B. (2009). "Regrouping particle swarm optimization: A new global optimization algorithm with improved performance consistency across benchmarks". In: *Systems, Man and Cybernetics, 2009. SMC 2009. IEEE International Conference on*, pp. 3901–3908.

Fan, H. (2002). "A modification to particle swarm optimization algorithm". In: *Engineering Computations* 19.8, pp. 970–989. DOI: 10.1108/02644400210450378.

Feng, Ying, Rabbath, C. A., Chai, T., and Su, C. Y. (2009). "Robust adaptive control of systems with hysteretic nonlinearities: A Duhem hysteresis modelling approach". In: *AFRICON 2009*, pp. 1–6.

Ge, P. and Jouaneh, M. (1996). "Tracking control of a piezoceramic actuator". In: *IEEE Transactions on Control Systems Technology* 4.3, pp. 209–216.

Goodwin, G. C. and Sin, K. S. (2009). *Adaptive Filtering Prediction and Control*. New York, NY, USA: Dover Publications.

Gorbet, R. B., Morris, K. A., and Wang, D. W. L. (2001). "Passivity-based stability and control of hysteresis in smart actuators". In: *IEEE Trans. Control Syst. Technol.* 9.1, pp. 5 –16.

Grossard, M. and Rakotondrabe, M. (2016). "High resolution actuators". In: *Actuators* 5.2, p. 18.

Gu, G. Y., Zhu, L. M., and Su, C. Y. (2014). "Modeling and compensation of asymmetric hysteresis nonlinearity for piezoceramic actuators with a modified Prandtl-Ishlinskii model". In: *IEEE Transactions on Industrial Electronics* 61.3, pp. 1583–1595.

Gu, G. Y., Zhu, L. M., Su, C. Y., Ding, H., and Fatikow, S. (2016). "Modeling and control of piezo-actuated nanopositioning stages: a survey". In: *IEEE Trans. Automation Sci. and Eng.* 13.1, pp. 313–332.

Guo, Y., Mao, J., and Zhou, K. (2011). "Modeling and control of Giant Magnetostrictive Actuator based on Bouc-Wen model". In: *Control Conference (ASCC), 2011 8th Asian*, pp. 530–534.

Habineza, D., Rakotondrabe, M., and Le Gorrec, Y. (2015). "Bouc–Wen modeling and feedforward control of multivariable hysteresis in piezoelectric systems: application to a 3-DoF piezotube scanner". In: *IEEE Trans. on Control Syst. Technol.* 23.5, pp. 1797–1806.

Hackl, C. M. (2015). "Current PI-funnel control with anti-windup for synchronous machines". In: *2015 54th IEEE Conference on Decision and Control (CDC)*, pp. 1997–2004.

Hassani, V., Tjahjowidodo, T., and Do, T. N. (2014). "A survey on hysteresis modeling, identification and control". In: *Mech. Syst. Signal Process.* 49.1, pp. 209 –333.

Hopfe, N., Ilchmann, A., and Ryan, E. P. (2010). "Funnel Control With Saturation: Nonlinear SISO Systems". In: *IEEE Transactions on Automatic Control* 55.9, pp. 2177–2182.

Hua, C. and Li, Y. (2015). "Output feedback prescribed performance control for interconnected time-delay systems with unknown Prandtl–Ishlinskii hysteresis". In: *Journal of the Franklin Institute* 352.7, pp. 2750 –2764.

Ikhouane, F. and Rodellar, J. (2006). "A linear controller for hysteretic systems". In: *IEEE Transactions on Automatic Control* 51.2, pp. 340–344.

— (2007). *Systems with hysteresis, analysis, identification and control using the bouc-wen model*. West Sussex, England: John Wiley & Sons, Ltd.

Ilchmann, A., Ryan, E. P., and Sangwin, C. J. (2002). "Tracking with prescribed transient behaviour". In: *ESAIM: COCV* 7, pp. 471–493.

Iyer, R. V. and Shirley, M. E. (2004). "Hysteresis parameter identification with limited experimental data". In: *IEEE Transactions on Magnetics* 40.5, pp. 3227–3239.

Iyer, R. V. and Tan, X. (2009). "Control of hysteretic systems through inverse compensation". In: *IEEE Control Systems* 29.1, pp. 83 –99.

Janaideh, M. Al, Rakotondrabe, M., and Aljanaideh, O. (2016). "Further results on hysteresis compensation of smart micropositioning systems with the inverse Prandtl-Ishlinskii compensator". In: *IEEE Transactions on Control Systems Technology* 24.2, pp. 428–439.

Janocha, H. and Kuhnen, K. (2000). "Real-time compensation of hysteresis and creep in piezoelectric actuators". In: *Sensors and Actuators A: Physical* 79.2, pp. 83 –89.

Jayawardhana, B., Ouyang, R., and Andrieu, V. (2012). "Stability of systems with the Duhem hysteresis operator: The dissipativity approach". In: *Automatica* 48.10, pp. 2657–2662. DOI: http://dx.doi.org/10.1016/j.automatica.2012.06.069.

Jiang, H., Ji, H., Qiu, J., and Chen, Y. (2010). "A modified prandtl-ishlinskii model for modeling asymmetric hysteresis of piezoelectric actuators". In: *IEEE Transactions on Ultrasonics, Ferroelectrics, and Frequency Control* 57.5, pp. 1200 –1210.

Kaplanoglu, E. (2012). "Design of shape memory alloy-based and tendon-driven actuated fingers towards a hybrid anthropomorphic prosthetic hand". In: *Int. J. Adv. Robot. Syst.* 9, pp. 1 –6.

Karpelson, M., Wei, G. Y., and Wood, R. J. (2012). "Driving high voltage piezoelectric actuators in microrobotic applications". In: *Sens. Actuators A: Phys.* 176, pp. 78 –89.

Ko, H. P., Jeong, H., and Koc, B. (2008). "Piezoelectric actuator for mobile auto focus camera applications". In: *Journal of Electroceramics* 23.2, p. 530. ISSN: 1573-8663. DOI: 10.1007/s10832-008-9529-8. URL: http://dx.doi.org/10.1007/s10832-008-9529-8.

Kostarigka, A. K. and Rovithakis, G. A. (2012). "Adaptive Dynamic Output Feedback Neural Network Control of Uncertain MIMO Nonlinear Systems With Prescribed Performance". In: *IEEE Transactions on Neural Networks and Learning Systems* 23.1, pp. 138–149.

Krejci, P. and Kuhnen, K. (2001). "Inverse control of systems with hysteresis and creep". In: *IEE Proceedings - Control Theory and Applications* 148.3, pp. 185 –192.

Kuhnen, K. (2003). "Modeling, Identification and Compensation of Complex Hysteretic Nonlinearities: A Modified Prandtl-Ishlinskii Approach". In: *European Journal of Control* 9.4, pp. 407 –418.

Levi, D. S., Kusnezov, N., and Carman, G. P. (2008). "Smart materials applications for pediatric cardiovascular devices". In: *Pediatr. Res.* 63.5, pp. 552 –558.

Li, Z., Su, C. Y., Chen, X., and Liu, S. (2014). "Prescribed adaptive control of unknown hysteresis in smart material actuated systems". In: *Production & Manufacturing Research* 2.1, pp. 712–724.

Lin, C. J., Yau, H. T., Lee, C. Y., and Tung, K. H. (2013). "System identification and semiactive control of a squeeze-mode magnetorheological damper". In: *IEEE/ASME Transactions on Mechatronics* 18.6, 1691–1701.

Manzoori, A. and Nezhad, H. T. (2016). "Application of an extended Bouc-Wen model in seismic response prediction of unbonded fiber-reinforced isolators". In: *Journal of Earthquake Engineering*, pp. 1–18.

Mayergoyz, I. (1986). "Mathematical models of hysteresis". In: *IEEE Transactions on Magnetics* 22.5, pp. 603–608.

Melbert, J., Raupach, C., Wang, Q., and Niestroj, F. (2006). "Piezo actuators for automotive injection systems". In: *MTZ Worldw.* 67.3, pp. 16 –18.

Na, J. (2013). "Adaptive prescribed performance control of nonlinear systems with unknown dead zone". In: *International Journal of Adaptive Control and Signal Processing* 27.5, pp. 426–446.

Oh, J. H. and Bernstein, D. S. (2005). "Semilinear Duhem model for rate-independent and rate-dependent hysteresis". In: *IEEE Trans. Autom. Control.* 50.5, pp. 631–645.

Oh, J. H., Drincic, B., and Bernstein, D. S. (2009). "Nonlinear feedback models of hysteresis". In: *IEEE Control Systems* 29.1, pp. 100 –119.

Olabi, A. and Grunwald, A. (2008). "Design and application of magnetostrictive materials". In: *Mater. Des.* 29.2, pp. 469 –483.

Padthe, A. K., Drincic, B., Oh, J. H., Rizos, D. D., Fassois, S. D., and Bernstein, D. S. (2008). "Duhem modeling of friction-induced hysteresis". In: *IEEE Control Systems* 28.5, pp. 90–107.

Pant, M., Thangaraj, R., and Abraham, A. (2007). "A new PSO algorithm with crossover operator for global optimization problems". In: *Innovations in Hybrid Intelligent Systems*. Ed. by Emilio Corchado, Juan M. Corchado, and Ajith Abraham. Berlin, Heidelberg: Springer Berlin Heidelberg, pp. 215–222.

Rakotondrabe, M. (2011). "Bouc-Wen modeling and inverse multiplicative structure to compensate hysteresis nonlinearity in piezoelectric actuators". In: *IEEE Transactions on Automation Science and Engineering* 8.2, pp. 428–431.

Reimers, A. and Della Torre, E. (1998). "Fast Preisach-based magnetization model and fast inverse hysteresis model". In: *IEEE Trans. Magn.* 34.6, 3857–3866.

Riccardi, L., Naso, D., Janocha, H., and Turchiano, B. (2012). "A precise positioning actuator based on feedback-controlled magnetic shape memory alloys". In: *Mechatronics* 22.5, pp. 568–576.

Riccardi, L., Naso, D., Turchiano, B., and Janocha, H. (2013). "LMI-based design of linear controllers for a magnetic shape memory push-push actuator". In: *52nd IEEE Conference on Decision and Control*, pp. 6634–6639.

Rosenbaum, S., Ruderman, M., Strohla, T., and Bertram, T. (2010). "Use of Jiles–Atherton and Preisach Hysteresis Models for Inverse Feed-Forward Control". In: *IEEE Transactions on Magnetics* 46.12, pp. 3984–3989.

Ruderman, M. and Bertram, T. (2010). "Discrete dynamic Preisach model for robust inverse control of hysteresis systems". In: *49th IEEE Conference on Decision and Control (CDC)*, pp. 3463–3468.

Shan, Y. and Leang, K. K. (2012). "Accounting for hysteresis in repetitive control design: Nanopositioning example". In: *Automatica* 48.4, pp. 1751 –1758.

Song, D. and Li, C.J. (1999). "Modeling of piezo actuator's nonlinear and frequency dependent dynamics". In: 9.4, pp. 391–410.

Song, J. and Der Kiureghian, A. (2006). "Generalized bouc–wen model for highly asymmetric hysteresis". In: *J. Eng. Mech.* 132.6, 610–618.

Stakvik, J. Å., Ragazzon, M. R.P., Eielsen, A. A., and Gravdahl, J. T. (2015). "On implementation of the Preisach Model: identification and inversion for hysteresis compensation". In: *Modeling, Identification and Control* 36.3, pp. 133–142. DOI: 10.4173/mic.2015.3.1.

Su, C. Y., Stepanenko, Y., Svoboda, J., and Leung, T. P. (2000). "Robust adaptive control of a class of nonlinear systems with unknown backlash-like hysteresis". In: *IEEE Transactions on Automatic Control* 45.12, pp. 2427–2432.

Tan, U. X., Latt, W. T., Shee, C. Y., Riviere, C. N., and Ang, W. T. (2009). "Feedforward controller of ill-conditioned hysteresis using singularity-free Prandtl-Ishlinskii model". In: *IEEE/ASME Transactions on Mechatronics* 14.5, pp. 598–605.

Tan, X. and Baras, J. S. (2004). "Modeling and control of hysteresis in magnetostrictive actuators". In: *Automatica* 40, 1469–1480.

Tan, X., Venkataraman, R., and Krishnaprasad, P. S. (2001). "Control of hysteresis: Theory and experimental results". In: *IN SMART STRUCTURES AND MATERIALS 2001: MODELING, SIGNAL PROCESSING, AND CONTROL IN SMART STRUCTURES*, pp. 101–112.

Vedagarbha, P., Dawson, D. M., and Feemster, M. (1999). "Tracking control of mechanical systems in the presence of nonlinear dynamic friction effects". In: *IEEE Trans. Control Syst. Technol.* 7.4, pp. 446–456.

Venkataraman, R. and Krishnaprasad, P. S. (2000). "Approximate inversion of hysteresis: theory and numerical results [magnetostrictive actuator]". In: *Decision and Control, 2000. Proceedings of the 39th IEEE Conference on*. Vol. 5, pp. 4448–4454.

Wang, G., Chen, G., and Bai, F. (2015a). "Modeling and identification of asymmetric bouc–wen hysteresis for piezoelectric actuator via a novel differential evolution algorithm". In: *Sensors Actuators, A Phys.* 235, 105–118.

Wang, S., Ren, X., Na, J., and Zeng, T. (2016). "Extended-State-Observer-Based Funnel Control for Nonlinear Servomechanisms With Prescribed Tracking Performance". In: *IEEE Transactions on Automation Science and Engineering* PP.99, pp. 1–11.

Wang, Z., Witthauer, A., Zou, Q., Kim, G. Y., and Faidley, L. (2015b). "Control of a magnetostrictive actuator-based micromachining system for optimal high-speed microforming process". In: *IEEE/ASME Trans. Mechatronics* 20.3, pp. 1046 –1055.

Wang, Z. Y. and Mao, J. Q. (2010). "On PSO Based Bouc-Wen modeling for Piezoelectric Actuator". In: *Intelligent Robotics and Applications: Third International Conference, ICIRA 2010, Shanghai, China, November 10-12, 2010. Proceedings, Part I*. Berlin, Heidelberg: Springer Berlin Heidelberg, pp. 125–134. ISBN: 978-3-642-16584-9.

Xie, Y., Tan, Y., and Dong, R. (2013). "Nonlinear modeling and decoupling control of XY micropositioning stages with piezoelectric actuators". In: *IEEE/ASME Transactions on Mechatronics* 18.3, pp. 821–832.

Xu, Q. (2015). "Piezoelectric Nanopositioning Control Using Second-Order Discrete-Time Terminal Sliding-Mode Strategy". In: *IEEE Trans. on Ind. Electron.* 62.12, pp. 7738 –7748.

Xu, Q. and Kiong, K. (2016). *Advanced control of piezoelectric micro-/nanopositioning systems*. New York, NY, USA: Springer.

Xu, Q. and Li, Y. (2010). "Dahl model-based hysteresis compensation and precise positioning control of an XY parallel micromanipulator with piezoelectric actuation". In: *Trans. ASME., J. Dyn. Syst. Meas* 132.4, p. 041011.

Yang, X., Yuan, J., Yuan, J., and Mao, H. (2007). "A modified particle swarm optimizer with dynamic adaptation". In: *Applied Mathematics and Computation* 189.2, pp. 1205–1213.

Zhang, L., Xia, Y., Lu, K., Fang, Y., Lu, Q., Ma, J., and Pan, H. andWang, D. (2015). "Motor-driven giant magnetostrictive actuator". In: *IEEE Trans. Magnetics* 51.10, pp. 1–7.

Zhang, T., Li, H. G., and Cai, G. P. (2013). "Hysteresis identification and adaptive vibration control for a smart cantilever beam by a piezoelectric actuator". In: *Sensors Actuators, A Phys.* 203, 168–175.

Zhong, J. and Yao, B. (2008). "Adaptive robust precision motion control of a piezoelectric positioning stage". In: *IEEE Trans. Control Syst. Technol.* 16.5, pp. 1039 –1046.

Zhou, J., Wen, C., and Li, T. (2012). "Adaptive output feedback control of uncertain nonlinear systems with hysteresis nonlinearity". In: *IEEE Trans. Autom. Control.* 57.10, pp. 2627–2633.

Zhou, M. and Wang, J. (2013). "Research on Hysteresis of Piezoceramic Actuator Based on the Duhem Model". In: *The Scientific World Journal* 2013.Article ID 814919, pp. 1–6.

Zhou, M., Wang, S., and Gao, W. (2013). "Hysteresis modeling of magnetic shape memory alloy actuator based on Krasnosel'skii-Pokrovskii model". In: *The Scientific World Journal*, p. 865176.